

# On the Behavior of Contaminants in Cryogenic Helium Refrigeration Systems

by

Ho-Myung Chang

B.S.E., Seoul National University, Seoul, Korea  
(1983)

M.S.E., The University of Michigan, Ann Arbor, Michigan  
(1984)

Submitted to the Department of Mechanical  
Engineering in Partial Fulfillment of the  
Requirements for the Degree of

Doctor of Philosophy

at the  
Massachusetts Institute of Technology  
May 1988

© Massachusetts Institute of Technology 1988

Signature of Author \_\_\_\_\_  
Department of Mechanical Engineering  
May 5, 1988

Certified by \_\_\_\_\_  
Joseph L. Smith, Jr.  
Thesis Supervisor

Accepted by \_\_\_\_\_  
Ain A. Sonin  
Chairman, Departmental Committee on Graduate Students

MASSACHUSETTS INSTITUTE  
OF TECHNOLOGY

MAY 25 1988  
ARCHIVES

**For My Parents,  
Sae-Kang & Choon-Jo Son Chang,**

**My Wife,  
Young-Sook,**

**and**

**My Daughter,  
Hee-Won**

# On the Behavior of Contaminants In Cryogenic Helium Refrigeration Systems

by

Ho-Myung Chang

Submitted to the Department of Mechanical  
Engineering on May 5, 1988 in partial fulfillment of  
the requirements for the degree of Doctor of Philosophy

## Abstract

The physics of contaminant condensation in cryogenic helium refrigeration systems was investigated both analytically and experimentally to understand its principal mechanism. The behavior of a contaminant in fully-developed laminar flow through a round tube was formulated into a mass transfer problem and solved analytically to find the concentration distribution of the contaminant. Thereafter, the wall accumulation rate was obtained on the assumption that no snow formed. Since the Lewis number of every common contaminant was greater than unity, super-saturation of the contaminant always existed. From the temperature and concentration profiles, a linearized expression for the degree of super-saturation was derived, which was good for the prediction of the onset condition and the most probable location of snow formation.

An experiment was designed and performed to detect the spatial distribution of wall accumulation of a contaminant in a test column. After the column was contaminated in a well-posed condition, a sharp temperature wave generated by a continuously moving heat source was propagated from the cold to the warm end (opposite to the flow direction), flushing the accumulated contaminant. A detector measured the concentration of the migrating contaminant at the exit of the column. The time history of the detector output successfully reflected the spatial distribution, because the continuous heating was locally very intensive and the dispersion of the concentration was minimized. The contamination was 100 ppm carbon dioxide in helium, and a 1.0 mm ID capillary tubing was tested for various conditions of 3 to 30 Reynolds number and 1.6 to 4 atm total pressure. The detector was a Thermal Conductivity Detector and the intensive local heating was obtained with sub-cooled boiling heat transfer through an auxiliary liquid, propane.

(Over)

When the degree of super-saturation was small, the contaminant was continuously diffused to the tube wall and sublimated without any noticeable snow formation as the analysis described. When the super-saturation increased, formation of snow and its deposition on the wall at a distance from the formed location were clearly observed. From this observed transition, a prediction for the onset of snow formation and the general behavior of formed snow was possible in terms of the derived degree of super-saturation. A dimensional analysis showed that the formation of snow would be very active in many practical cryogenic helium refrigeration systems because the degree of super-saturation was much greater than the onset condition. Control of the snow formation and migration would be a critical factor in reducing the detrimental effects of contaminants.

Thesis Supervisor : Joseph L. Smith, Jr.

Title : Professor of Mechanical Engineering

# Acknowledgements

I would like to thank Professor Joseph L. Smith, Jr., my thesis supervisor. He suggested the thesis topic and guided me with many helpful ideas. I believe that he is a great engineering educator. Also I wish to thank other committee members, Dr. Yukikazu Iwasa and Prof. James C. Keck, for their advices. This project was supported mostly by MIT Cryogenic Engineering Laboratory, and some of the experimental equipment was supported by the NSF.

The members of MIT CEL helped this project in many ways. Alan Crunkleton, my officemate, was very helpful in designing the experimental apparatus and in writing this thesis and other documents. He gave me many stimulating advices and useful informations. Bob, a lab engineer, was most helpful in constructing the apparatus. He machined several parts of my experiment and solved "many" major and minor problems encountered in the assembly process. Mike, a UROP student, prepared the test column and other tubings. Also, I thank other labmates, Jim, (another) Alan, Thong, Duan, and Eun-Soo for their help in a direct or indirect way.

David Otten in the electrical engineering department helped the design of electronic control parts of the experiment, and John Carswell in Gow-Mac Instrument Co. in New Jersey taught me how to operate the Gas Analyzer with more than 20 times of telephone conversations. Omar Knio, my friend, helped the computation of analytical results.

I would like to express my special thanks to Mr. and Mrs. Su-Yong Choi in New York City, for their parent-like support throughout my graduate study. Because of their support, I didn't feel alone in this foreign country.

Finally, I appreciate the love and support of my family. As always, I am proud of my parents' special way of love to me. They were most interested in my overall education and provided everything I need. My parents-in-law showed their love in many ways, too. Love and patience of my wife, Young-Sook, was essential to this project. She always encouraged me in her special warm atmosphere. And the birth of our "lovely" daughter, Hee-Won, kept our spirit high for the last year of the project.

# Table of Contents

<b>Abstract</b>	<b>3</b>
<b>Acknowledgements</b>	<b>5</b>
<b>List of Figures</b>	<b>9</b>
<b>List of Tables</b>	<b>12</b>
<b>List of Symbols</b>	<b>13</b>
<b>Chapter 1 Introduction</b>	<b>17</b>
1.1 Background	17
1.2 Objectives and Scope of Thesis	21
1.2.1 Analytical Description of Contamination	21
1.2.2 Experimental Detection Scheme	27
<b>Chapter 2 Mass Transfer Analysis.</b>	<b>29</b>
2.1 System Description	29
2.2 Assumptions	32
2.3 Formulation and Solution	38
2.3.1 Governing Equation and Boundary Conditions	38
2.3.2 Solution for the Concentration of Contaminant	44
2.3.3 Wall Accumulation Rate without Snow Formation	51
2.3.4 Mass Transfer Coefficient and Sherwood Number	56
2.3.5 Mass Transfer Entry Length	62

2.4 Super-Saturation . . . . .	.70
2.4.1 Lewis Numbers of Common Contaminants in Helium . . . . .	.70
2.4.2 Degree of Super-Saturation and Snow Formation . . . . .	.75
<b>Chapter 3 Experimental Apparatus and Procedure . . . . .</b>	<b>.86</b>
3.1 Overall Configuration of Experiment . . . . .	.86
3.2 Design of Apparatus . . . . .	.91
3.2.1 Test Column . . . . .	.91
3.2.2 Detector . . . . .	.92
3.2.3 Temperature Control of Test Column . . . . .	.99
3.2.4 Data Acquisition . . . . .	107
3.3 Assembly of Apparatus . . . . .	110
3.4 Procedure . . . . .	122
3.4.1 Preparation of Experiment . . . . .	122
3.4.2 The Temperature Set-Up Phase . . . . .	123
3.4.3 The Contamination Phase . . . . .	126
3.4.4 The Detection Phase . . . . .	126
<b>Chapter 4 Results and Discussion . . . . .</b>	<b>130</b>
4.1 Test Conditions and Experimental Results . . . . .	130
4.2 Interpretation of Results . . . . .	138
4.2.1 Dispersion Mechanisms . . . . .	138
4.2.2 Experimental and Analytical Distributions of Wall Accumulation . . . . .	142

4.3 Discussions . . . . .	152
4.3.1 Onset of the Snow Formation . . . . .	152
4.3.2 Contamination in Practical Helium Systems . . . . .	156
 Chapter 5 Conclusion . . . . .	 159
5.1 Summary of Study . . . . .	159
5.2 Conclusions . . . . .	162
5.3 Recommendations for Further Study . . . . .	164
 Appendix A Sublimation Data of Carbon Dioxide . . . . .	 165
Appendix B Graetz Functions . . . . .	172
Appendix C Computation of Wall Accumulation and Sherwood Number without Snow Formation . . . . .	 180
Appendix D Convection Augmented Diffusion . . . . .	191
D.1 Introduction . . . . .	191
D.2 Effective Mass Diffusivity . . . . .	195
D.3 Optimum Velocity for Minimum Dispersion . . . . .	198
Appendix E Green's Function for Convection-Diffusion Equation	199
Appendix F Details of Experimental Results . . . . .	204
 References . . . . .	 212
Biographical Note . . . . .	216



# List of Figures

1.1	Collins Cycle for the Helium Refrigeration System . . . . .	.21
1.2	Description of the Zeroth-Order Analysis . . . . .	.25
1.3	Zeroth-Order Accumulation Rate of Carbon Dioxide . . . . .	.26
1.4	Experimental Scheme to Detect the Spatial Distribution of Contaminant Accumulation . . . . .	.28
2.1	System Description . . . . .	.31
2.2	Control Volume of Differential Element . . . . .	.43
2.3	Superposition Integral of infinitesimal Steps . . . . .	.50
2.4	Mass Accumulation Rate for $Re=10$ . . . . .	.53
2.5	Mass Accumulation Rate for $Re=100$ . . . . .	.54
2.6	Mass Accumulation Rate for $Re=1000$ . . . . .	.55
2.7	Local Sherwood Number Distribution . . . . .	.61
2.8	1-Dimensional Differential Control Volume . . . . .	.67
2.9	Boundary Layers on a Flat Plate . . . . .	.68
2.10	Leveque Approximation for the Sherwood Number at the Entry Region . . . . .	.69
2.11	Lewis Number and Super-Saturation . . . . .	.73
2.12	Super-Saturation at the Entry Region . . . . .	.83
2.13	Distribution of $\Delta P$ along $x$ . . . . .	.84
2.14	Degree of Super-Saturations in the Pressure and Temperature Units .	85
3.1	Schematic Diagram for the Overall Configuration of Experiment . .	.90
3.2	Schematic Flow Diagram of Gas Analyzer Unit . . . . .	.97

3.3	Photograph of Gas Analyzer and Data Acquisition System . . . . .	98
3.4	Temperature Control System of Test Column . . . . .	104
3.5	Set-Up of Linear Temperature of Test Column . . . . .	105
3.6	Locations of Thermocouples on the Test Column . . . . .	109
3.7	Warm End Assembly . . . . .	113
3.8	Cold End Assembly . . . . .	115
3.9	Schematic Diagram of a Tube Passing through the Bottom Plate .	117
3.10	Photograph of Complete Experiment . . . . .	118
3.11	Photograph of Top Assembly . . . . .	119
3.12	Photograph of Bottom Assembly . . . . .	119
3.13	Photograph of Fluid Control Panel . . . . .	120
3.14	Obtained Linear Temperature of Test Column . . . . .	125
3.15	Time History of Temperature at Point 3 . . . . .	129
4.1	TCD Output of RUN 3 . . . . .	134
4.2	TCD Output of RUN 4 . . . . .	135
4.3	TCD Output of RUN 5 . . . . .	136
4.4	TCD Output of RUN 6 . . . . .	137
4.5	Explanation for the Test and Detection Length . . . . .	147
4.6	Experimental and Analytical Distribution of the Mass Accumulation for the RUN 4 . . . . .	148
4.7	Experimental and Analytical Distribution of the Mass Accumulation for the RUN 5 . . . . .	149
4.8	Experimental and Analytical Distribution of the Mass Accumulation for the RUN 6 . . . . .	150

4.9	Effect of Snow Formation on the Concentration Profile and the Distribution of Wall Accumulation . . . . .	151
4.10	Experimental Conditions on a Dimensionless Temperature Gradient vs. Re Sc Diagram . . . . .	152
A.1	Sublimation Pressure of Carbon Dioxide . . . . .	169
A.2	Temperature Derivative of Sublimation Pressure of Carbon Dioxide	170
A.3	Latent Heat of Sublimation of Carbon Dioxide . . . . .	171
D.1	Dispersion of a Step Concentration . . . . .	194
E.1	Contour of Integration in Complex Plane . . . . .	203
F.1	TCD Output of RUN 1 . . . . .	205
F.2	TCD Output of RUN 2 . . . . .	206
F.3	TCD Output of RUN 7 . . . . .	207
F.4	TCD Output of RUN 8 . . . . .	208
F.5	TCD Output of RUN 9 . . . . .	209
F.6	TCD Output of RUN 10 . . . . .	210
F.7	TCD Output of RUN 11 . . . . .	211

# List of Tables

2.1	Lewis Numbers of Common Contaminants in Helium . . . . .	74
3.1	Characteristics of Thermal Conductivity Detector and Flame Ionization Detector . . . . .	95
3.2	Specifications of the Selected Detector (GOW-MAC Instrument Co. Model 50-450) . . . . .	96
3.3	Elements of Column-Temperature Control System . . . . .	106
4.1	List of Test Conditions . . . . .	133
4.2	The Degree of Super-Saturation and Snow Formation for the Test Conditions . . . . .	154
A.1	Sublimation Data of Carbon Dioxide . . . . .	167
B.1	First Ten Eigen-Values and Important Constants . . . . .	179

## List of Symbols

<b>A</b>	<b>Cross Sectional Area of the Tube (m), <math>\pi d^2 / 4</math></b>
<b>a<sub>n</sub></b>	<b>n-th Coefficient of Series Solution, Dimensionless</b>
<b>C<sub>f</sub></b>	<b>Friction Coefficient, Dimensionless, <math>\tau_w / (\frac{1}{2} \rho u_m^2)</math></b>
<b>C<sub>p</sub></b>	<b>Specific Heat of Contaminant at Constant Pressure (KJ/Kg-K)</b>
<b>c</b>	<b>Concentration of Contaminant (Kg/m<sup>3</sup>)</b>
<b>c<sub>m</sub></b>	<b>Mean Concentration of Contaminant (Kg/m<sup>3</sup>)</b>
<b>c<sub>s</sub></b>	<b>Sublimation Concentration of Contaminant (Kg/m<sup>3</sup>)</b>
<b>D</b>	<b>Mass Diffusivity of Contaminant in Helium (m<sup>2</sup>/sec)</b>
<b>D<sub>eff</sub></b>	<b>Effective Mass Diffusivity of Contaminant in Helium (m<sup>2</sup>/sec)</b>
<b>d</b>	<b>Diameter of the Tube (m)</b>
<b>DSS</b>	<b>Degree of Super-Saturation, Dimensionless</b>
<b>G</b>	<b>Green's Function for Convection-Diffusion Equation, Dimensionless</b>
<b><math>\tilde{G}</math></b>	<b>Fourier Transform of the Green's Function, G, Dimensionless</b>
<b>H<sub>ig</sub></b>	<b>Heat of Sublimation of Contaminant (KJ/Kg)</b>
<b>h</b>	<b>Heat Transfer Coefficient (KW/m<sup>2</sup>-K)</b>
<b>h<sub>D</sub></b>	<b>Mass Transfer Coefficient (m/sec)</b>
<b>J<sub>v</sub></b>	<b>Bessel Function of order v, Dimensionless</b>
<b>k</b>	<b>Thermal Conductivity (KW/m-K)</b>
<b>L</b>	<b>Length of the Tube (m)</b>
<b>L<sub>a</sub></b>	<b>Mass Transfer Entrance Length (m)</b>
<b>Le</b>	<b>Lewis Number, Dimensionless, <math>\alpha/D</math></b>
<b>l</b>	<b>Length (Used as Needed) (m)</b>

$M_{acc}$	Mass Accumulation of Contaminant per unit length (Kg/m)
$\dot{M}_{acc}$	Mass Accumulation Rate of Contaminant per unit length (Kg/m-sec)
$\dot{m}$	Mass Transfer Rate of Contaminant (Kg/sec)
Nu	Nusselt Number, Dimensionless, $hd / k$
P	Partial Pressure of Contaminant (KPa)
$P_{in}$	Inlet Partial Pressure of Contaminant (KPa)
$P_s$	Sublimation Pressure of Contaminant (KPa)
$P_t$	Total Pressure (KPa)
Pe	Peclet Number, Dimensionless, $u_m d / \alpha$
$Pe_m$	Mass Transfer Peclet Number, Dimensionless, $u_m d / D$
Pr	Prandtl Number, Dimensionless, $\nu / \alpha$
$\dot{q}$	Heat Transfer Rate (KW)
R	Gas Constant of Contaminant (KJ/Kg-K)
$R_{He}$	Gas Constant of Helium (KJ/Kg-K)
$R_n$	n-th Eigen-Function of Graetz Equation, Dimensionless
r	Radial Coordinate (m)
$r_0$	Radius of the Tube (m)
Re	Reynolds Number Based on Diameter, Dimensionless, $u_m d / \nu$
$Re_x$	Reynolds Number Based on Axial Distance, Dimensionless, $u_m x / \nu$
Sc	Schmidt Number, Dimensionless, $\nu / D$
Sh	Sherwood Number, Dimensionless, $h_D d / D$
St	Stanton Number, Dimensionless, $Nu / (Re Pr)$
$St_m$	Mass Transfer Stanton Number, Dimensionless, $Sh / (Re Sc)$

<b>T</b>	<b>Temperature (K)</b>
<b>T<sub>m</sub></b>	<b>Mean Temperature (K)</b>
<b>t</b>	<b>Time Coordinate (sec)</b>
<b>u</b>	<b>Axial Velocity (m/sec)</b>
<b>u<sub>m</sub></b>	<b>Axial Mean Velocity (m/sec)</b>
<b>v<sub>h</sub></b>	<b>Heater Velocity (m/sec)</b>
<b>x</b>	<b>Axial Coordinate (m)</b>
<b>x'</b>	<b>Auxiliary Axial Coordinate (m)</b>
<b>y</b>	<b>Mole Fraction of Contaminant, Dimensionless</b>
<b>z</b>	<b>Auxiliary Radial coordinate, Dimensionless</b>

### Greek Symbols

<b><math>\alpha</math></b>	<b>Thermal Diffusivity (m<sup>2</sup>/sec)</b>
<b><math>\Delta P</math></b>	<b>Super-Saturation in Pressure (KPa)</b>
<b><math>\Delta T</math></b>	<b>Super-Saturation in Temperature (K)</b>
<b><math>\delta</math></b>	<b>Momentum Boundary Layer Thickness (m)</b>
<b><math>\delta_m</math></b>	<b>Mass Transfer Boundary Layer Thickness (m)</b>
<b><math>\epsilon</math></b>	<b>Effectiveness of Heat Exchanger, Dimensionless</b>
<b><math>\eta</math></b>	<b>Auxiliary Axial or Radial Coordinate (m) or Dimensionless</b>
<b><math>\lambda_n</math></b>	<b>n-th Eigen-Value of Graetz Equation, Dimensionless</b>
<b><math>\mu</math></b>	<b>Viscosity (Kg/m-sec)</b>
<b><math>\nu</math></b>	<b>Kinematic Viscosity (m<sup>2</sup>/sec)</b>
<b><math>\rho</math></b>	<b>Density of Helium (Kg/m<sup>3</sup>)</b>
<b><math>\sigma</math></b>	<b>Surface Tension of Boiling Bubble (N/m)</b>

$\tau$	Auxiliary Time Coordinate or Response Time of Detector (sec)
$\tau_w$	Shear Stress at Wall (N/m <sup>2</sup> )
$\xi$	Auxiliary Axial or Radial Coordinate (m) or Dimensionless
$\xi'$	Auxiliary Axial Coordinate (m)

### Subscripts

0	Properties at Sublimation Starting Point (except $r_0$ )
w	Properties at Wall of the Tube

### Centered Superscripts

-	Averaged Values
~	Non-Dimensionalized Values



# Chapter 1

## Introduction

### 1.1 Background

Contamination is one of the most critical factors affecting the reliability of cryogenic helium refrigeration or liquefaction systems. Any impurity gas in the helium is frozen before it reaches the liquid helium temperature, so the frozen contaminant remains inside of the helium systems, reducing the efficiency of the whole system and causing scheduled or unscheduled stoppage after a relatively long period of operation.

One of the clear ways to improve the cryogenic contamination problem is to use purified helium. Since the early stage of cryogenics, the development of helium-purification systems<sup>1-5, 20</sup> has been one of the major research areas, because obtaining pure helium is a prerequisite for the development of helium refrigeration and liquefaction systems. Common methods of helium purification are refrigeration purification and physical or chemical adsorption. Removal of water vapor and carbon dioxide with liquid nitrogen cooling is an example of the former. Nitrogen, oxygen, and inert gases such as argon, neon, or xenon are typically removed with the latter method. Frequently used adsorbents are silica gel, charcoal, and proper catalysts. Obviously, system life has been prolonged to a certain extent by using purified helium, but the purification method without an adequate understanding of the contamination mechanism

has not provided the best solution to improve the reliability or avoid the stoppage.

Many contemporary cryogenic equipments require a long-life and miniaturized system. In order to design such a system, it is essential to minimize the detrimental effect of contaminants. Currently, the principles of the contamination mechanism are not generally known except for a few empirical results. Lack of understanding of the mechanism often causes an unnecessary over-design of the system with unacceptable performance.

In spite of the significance of the problem, little basic work has been done about the behavior of contaminants in cryogenic helium systems. This seemingly contradictory situation has arisen for the following two reasons. First, there is a simple solution: a short-time run and warm-up of the system to remove the condensed contaminants. Second, the quantitative study for the condensation and migration of contaminants is extremely difficult. Basically, contamination is an unsteady combined heat and mass transfer problem of a multi-component and multi-phase system. An analytical approach to this complicated problem has not seemed to be an easy task. Furthermore, the critical location and amount of frozen or condensed contaminants in the cryogenic systems have not been experimentally verifiable in a simple way.

Koenig <sup>6</sup> measured the distribution of contaminant accumulation in a thermal regenerator by dividing the regenerator into many small sections each of which could be individually isolated from one another. His sectioning method was not good in measuring the proper spatial distribution, because the

sectioning wall complicated the mass transfer and accumulation characteristics of the contaminant. Ashley <sup>7</sup> suggested a light scattering method to detect the cryogenic contamination. The condensed contaminant on a transparent tube wall scattered the imposed light, which indicated its location. This method does not seem to provide quantitative information of contaminant accumulation.

As always, a clue for the solution of such a complicated problem is expected in the understanding of the mechanism. For example, in a Collins cycle for the helium refrigeration system, shown in Figure 1.1, the question is where and how much contaminant is accumulated, interrupting the steady operation of the whole system. Some available vapor-pressure data for the common contaminants, such as carbon dioxide, nitrogen, oxygen, neon, and argon, show that every gaseous contaminant should be sublimated to the solid phase (because its partial pressures is far below the triple point for a typical contamination level, less than 10 ppm, of commercial helium) at much above the temperature of the J-T valve, which has the smallest passage area. However, many cryogenic engineers think, without any solid evidence, that the stoppage of the system results from the clog-up of the J-T valve. If it can be explained and verified, the control of the contaminant migration from the sublimation location to the J-T valve may be much easier.

Therefore, the development of a proper analytical model and an experimental detection scheme to verify the spatial distribution of contaminant accumulation is very critical in obtaining specific ideas to improve the contamination problem, which is the ultimate goal of this study.

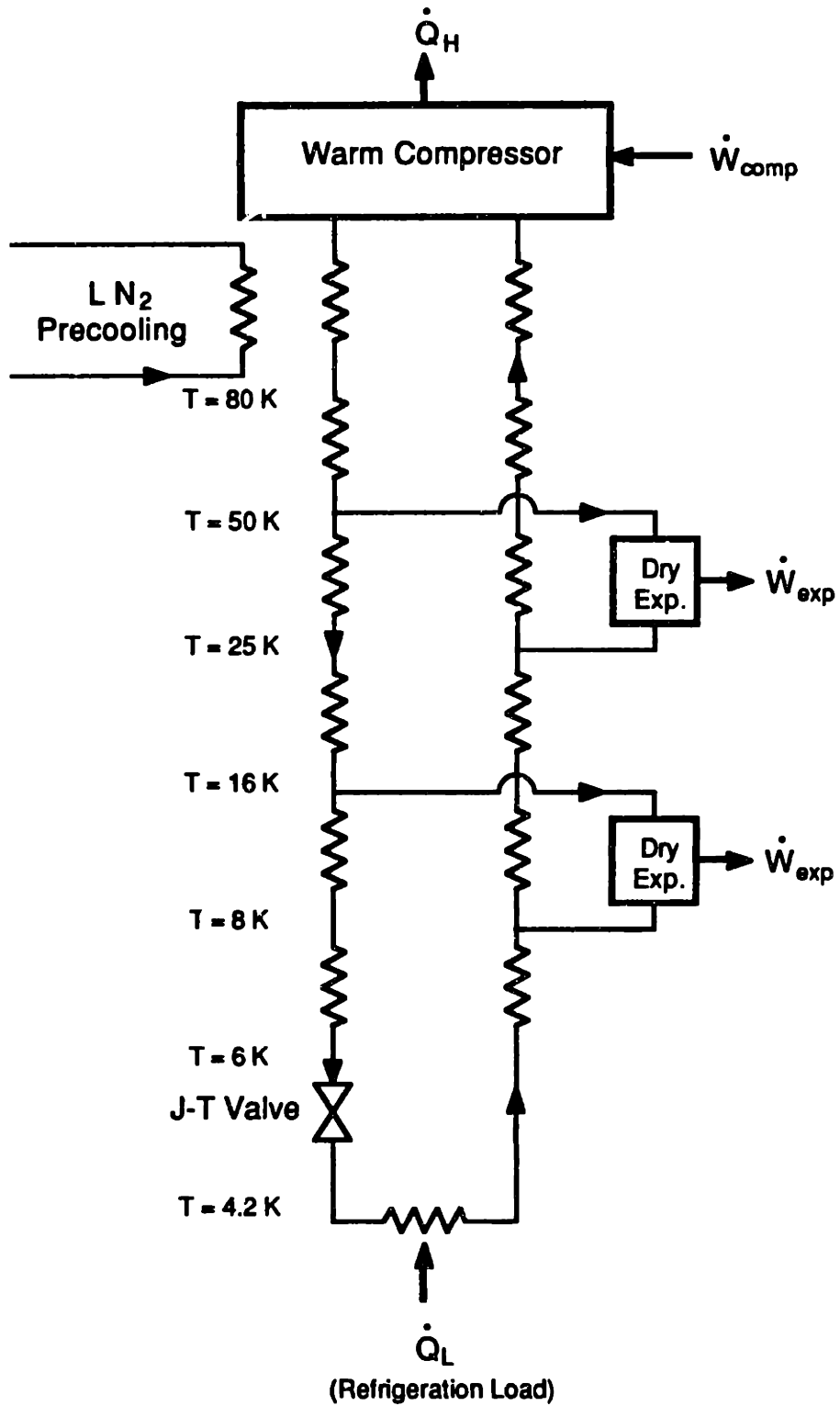


Figure 1.1 Collins Cycle for the Helium Refrigeration System

## **1.2 Objectives and Scope of Thesis**

**As a first step for the cryogenic contamination problem, this thesis has the following three objectives.**

- 1) Construction of an analytical model to predict the spatial distribution of a specific contaminant's accumulation for given conditions.**
- 2) Development and execution of an experimental technique to detect the distribution.**
- 3) Specific suggestion to improve the cryogenic contamination problem.**

**Toward these objectives, the direction of approach for this study is briefly presented in this section.**

### **1.2.1 Analytical Description of Contamination**

**The basic distribution of accumulated contaminant can be found with a "zeroth-order" analysis, which assumes an instantaneous diffusion of momentum, heat, and mass. Although the results may be unrealistic in simulating the helium systems, a description of the desired analytical model should be given on the basis of the zeroth-order analysis.**

**As the temperature decreases in the flow direction as shown in Figure 1.2 (a), the inlet partial pressure of a contaminant in helium gas reaches its sublimation pressure corresponding to the temperature distribution as shown in Figure 1.2 (b). From this point, the contaminant is sublimated and accumulation begins as shown in Figure 1.2 (c), because the partial pressure of the**

contaminant is the same as sublimation pressure according to the zeroth-order assumption.

The amount of accumulated contaminant is found by combining the continuity of the main fluid, helium, and of the contaminant. The mass balance of helium as an ideal gas for a constant pressure yields

$$\frac{d}{dx} \left( \frac{u}{T} \right) = 0, \quad (1.1)$$

where  $u$  is the local flow velocity. In Eqn. (1.1) the small contribution of the contaminant to the density of mixture is neglected. The mass balance of the contaminant in a differential length,  $dx$ , is written as

$$d \dot{m}_{acc} = A u c - A \left\{ u c + \frac{d}{dx} (u c) dx \right\}, \quad (1.2)$$

where  $\dot{m}_{acc}$  is the mass accumulation rate,  $A$  is the cross sectional area of passage, and  $c$  is the local concentration of contaminant, given by

$$c = \frac{P_s}{RT}, \quad (1.3)$$

for  $x \geq x_0$ . The sublimation pressure,  $P_s$ , in Eqn. (1.3) is a function of temperature.

If the mass accumulation rate per unit length is denoted by  $\dot{M}_{acc}$  and Eqn. (1.2) is rearranged with Eqn. (1.3), then

$$\dot{M}_{acc} = -\frac{A}{R} \frac{d}{dx} \left( \frac{u P_s}{T} \right). \quad (1.4)$$

Since  $(u/T)$  is a constant along  $x$  from Eqn. (1.1) and  $P_s$  is a function of temperature,

$$\dot{M}_{acc} = \frac{A u_0}{R T_0} \left( -\frac{dT}{dx} \right) \left( \frac{dP_s}{dT} \right) \quad (1.5)$$

where  $u_0$  and  $T_0$  denote the values of  $u$  and  $T$  at any given location, respectively. Therefore, the mass accumulation rate is proportional to the local temperature gradient at the location and the temperature derivative of sublimation pressure at the temperature.

To illustrate the zeroth-order behavior, the accumulation rate of carbon dioxide is plotted in Figure 1.3 for a linear temperature gradient. The accumulation rate is normalized with the maximum value at the sublimation starting point. The sublimation starting temperature is about 128 K for a 15 ppm of carbon dioxide in helium with 15 atm total pressure. The accumulation shape is essentially the exponential decay according to the sublimation curve, and most of contaminant is sublimated within 20 K below the starting temperature.

The desired analytical model includes two additional physical phenomena over this zeroth-order analysis. The first one is the finite diffusion of momentum, heat, and mass. The contribution of these transport phenomena to the modification of the zeroth-order analysis is very important in constructing the analytical model. The second one is the super-saturation (exactly, super-sublimation), associated with snow formation. Depending on the relative diffusion relation of heat and mass transfer, the partial pressure of contaminant may be greater than the sublimation pressure at the temperature of some

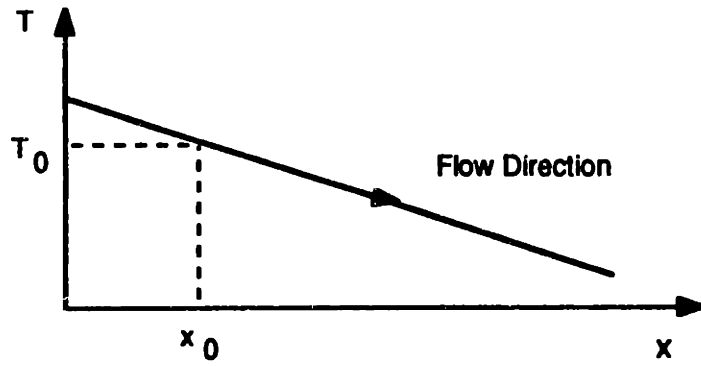
location other than the solid wall. If the super-saturation is large, the contaminant nucleates to form snow and migrates downstream instead of being accumulated on the wall through sublimation. The snow formation makes a drastic change on the behavior of contaminant described by the zeroth-order analysis.

Since the primary interest in this study is understanding the fundamentals, the system for which the analytical model is constructed is a "simple" but most important one: laminar flow in a round tube. As a beginning step of the analytical procedure, some simplifying assumptions are made after a careful examination of related physics. Then the contamination mechanism is formulated in a mass transfer problem. The solution of the partial differential equation yields the concentration distribution of contaminant, from which both the mass accumulation rate and the super-saturation relation are obtained. Nucleation and growth of contaminant for the snow formation cannot be fully described by the analysis only. However, with the partial aid of experimental results, a prediction for the onset of snow formation and the general behavior of the formed snow is included in this analytical model. Particular attention in the analytical model is paid to the effect of the following four input parameters on the behavior of contaminant:

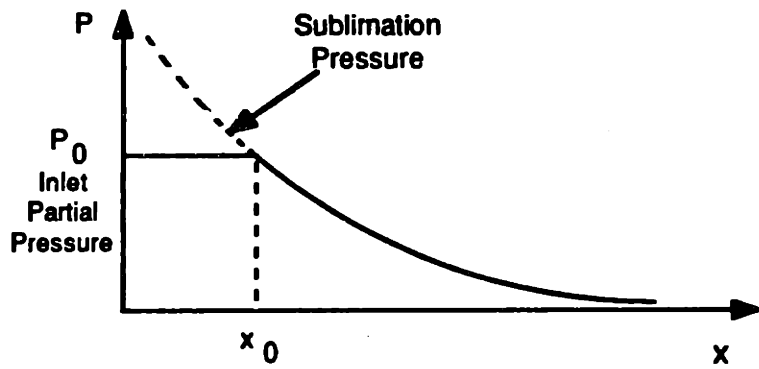
- 1) Temperature gradient of tube
- 2) Flow rate of gas mixture
- 3) Gas pressure and contamination level
- 4) Dimensions of tube.

Most of the procedure involving this analytical model is presented in Chapter 2.

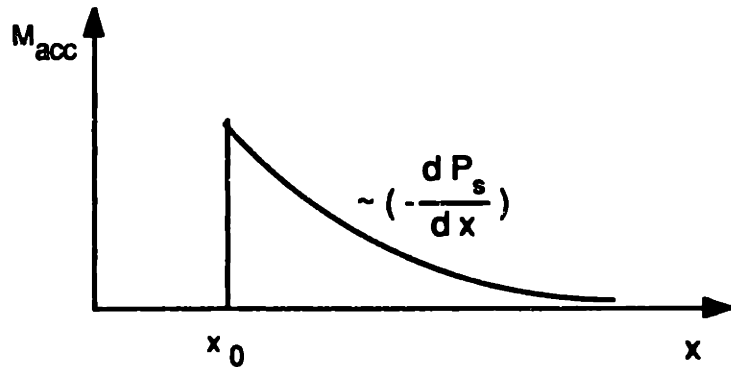




(a) Temperature Distribution



(b) Partial Pressure Distribution of Contaminant



(c) Accumulated Mass Distribution for Zeroth-Order

Figure 1.2 Description of the Zeroth-Order Analysis

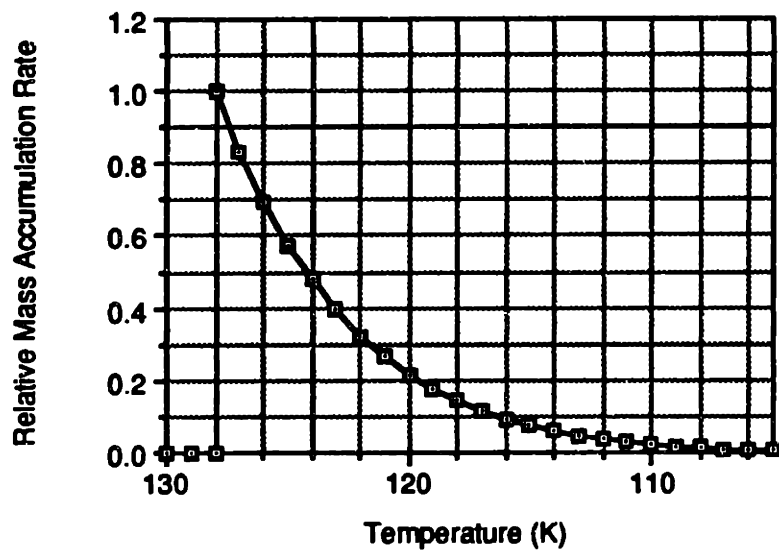


Figure 1.3 Zeroth-Order Accumulation Rate of Carbon Dioxide

## 1.2.2 Experimental Detection Scheme

A conceptual scheme to detect the spatial distribution of accumulated contaminant is shown in Figure 1.4. After a test column is contaminated in a well-posed condition (Figure 1.4 (a)), a sharp temperature wave generated by a continuously moving heat source is propagated from the low to the high temperature end (opposite to the flow direction), flushing the accumulated contaminant through the column as shown in Figure 1.4 (b). A detector located at the exit of the test column measures the concentration of contaminant as a function of time. The time history of the detector output like Figure 1.4 (c) reflects the spatial distribution of mass accumulation in the test column.

To minimize the loss of information in reproducing the spatial distribution from the time history of the detector output, the continuous heating should generate a sharp temperature front distribution as shown in Figure 1.4 (b), and the dispersion of the migration concentration wave of contaminant should be small. The sharp front temperature is obtained by a very intensive local heating and by a faster moving heating element than the actual thermal diffusion of the column.

An experiment designed and performed in this study is described in Chapter 3, and the critical results from the experiment are presented and discussed with the analytical model in Chapter 4.

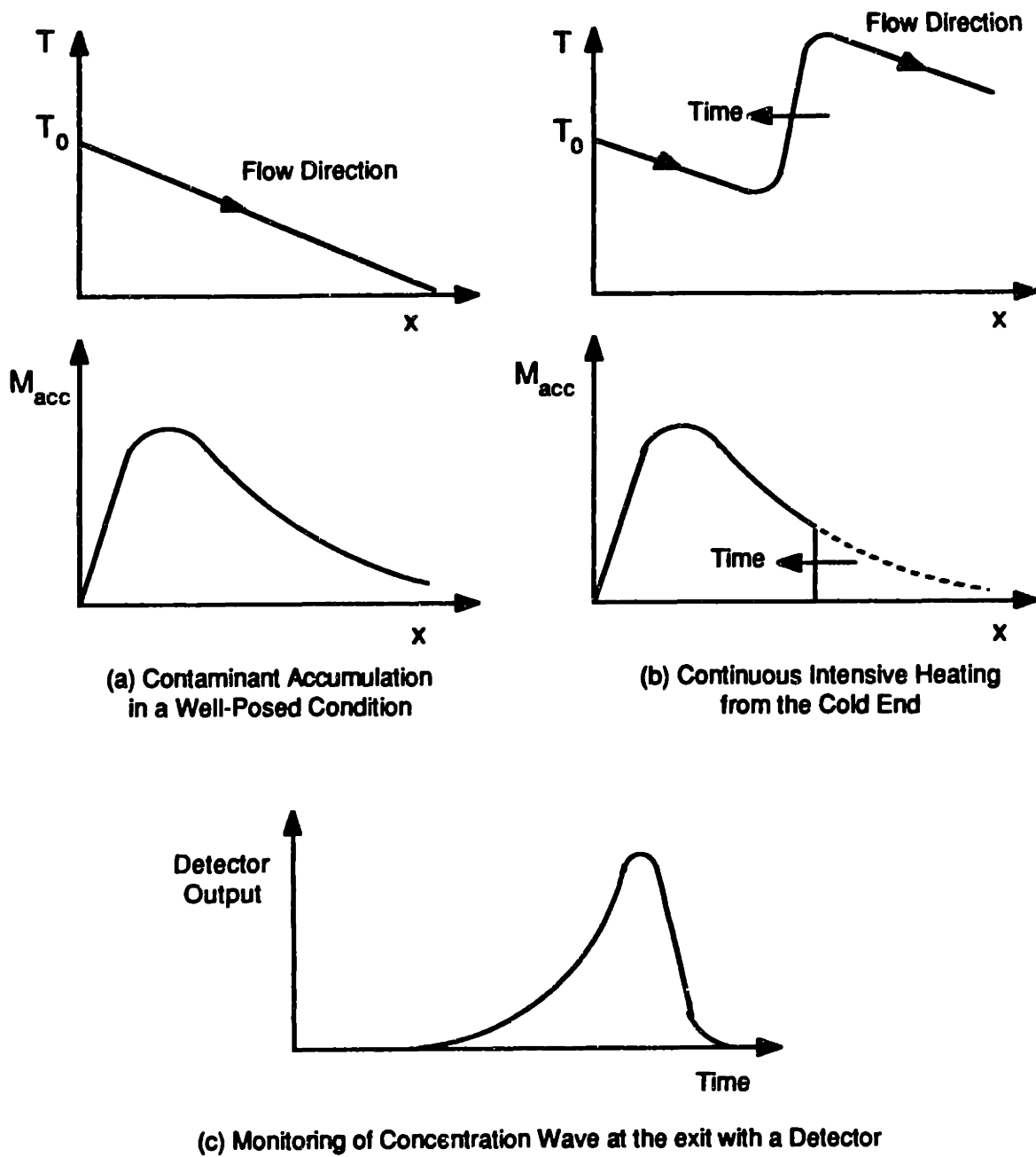


Figure 1.4 Experimental Scheme to Detect the Spatial Distribution of Contaminant Accumulation

## Chapter 2

### Mass Transfer Analysis

In this chapter, a mass transfer analysis is presented, including the calculation of wall accumulation rate without snow formation and the derivation of a simple and significant expression for the degree of super-saturation. There are two objectives of this analytical approach. The first is to acquire bottomline information for the cryogenic contamination mechanism, which is the sublimation phase change through mass transfer. This quantitative information is essential for understanding the leading behavior of contaminant and for the design of an experimental apparatus. The second objective is to interpret and discuss the experimental results. A somewhat qualitative description is provided which will play a critical role in drawing conclusions for this study.

#### 2.1 System Description

As mentioned in the previous chapter, the first step in understanding the cryogenic contamination problem is to make an analytical description for the contaminant accumulation for "simple" geometry and flow conditions. This section describes the "simple" system which is analytically solvable and, at the same time, simulates the part of cryogenic helium systems so that practically important information can be drawn from the solution. Of course, even if the primary concern is focused on this simple system, applicability of the results may be expanded to more complicated geometries and flow conditions with adequate modification as in other engineering problems.

As shown in Figure 2.1, the system is a round helium-filled tube, which has a fully developed laminar flow with a negative linear temperature gradient in its flow direction. In this system, the behavior of a specific contaminant whose mole fraction is very small (order of 10 to 100 ppm) in helium is to be sought. This situation is simulating part of a counterflow heat exchanger as in the Collins cycle for helium refrigeration systems shown in Figure 1.1.

Since the helium system has typically a very effective heat exchanger, the interest of this study is in the case of a small temperature difference,  $T_m - T_w$ . In this particular case, the ratio of length to diameter ratio of the tube is large (order of  $10^4$  to  $10^7$ ), which validates a few simplifying assumptions and makes analytical procedures easier.

A round tube is the basic geometry for internal flow and the actual geometry in many helium systems. A fully-developed flow condition is selected because the interesting temperature range is fairly low, so its location is far from the entrance of the tube. A linear temperature gradient is also good in simulating helium systems for the reason that the temperature range is relatively small compared with the temperature non-linearity which results from the temperature dependence of specific heat and thermal conductivity.

The only constraint to generalize this analytical description of helium systems is expressed with laminar-flow relations. This constraint is inevitable in a straightforward analytical procedure. Therefore it should be made clear at this point that analysis of the system here deals with the laminar region only, and the behavior of contaminant in a turbulent flow is excluded in this study.

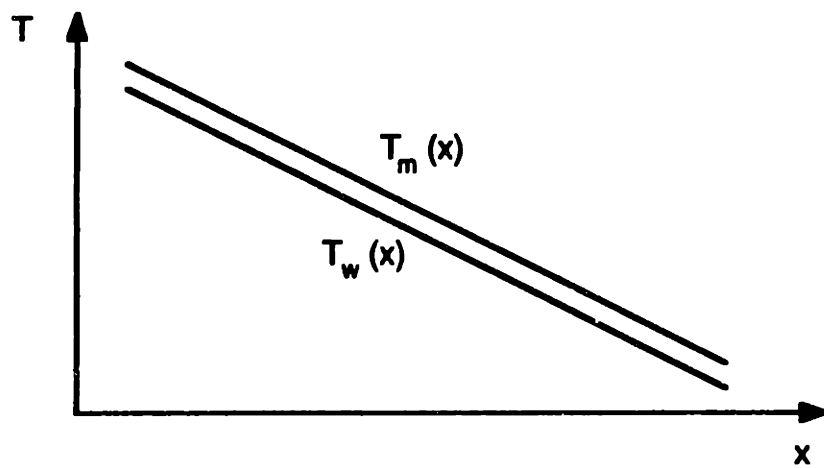
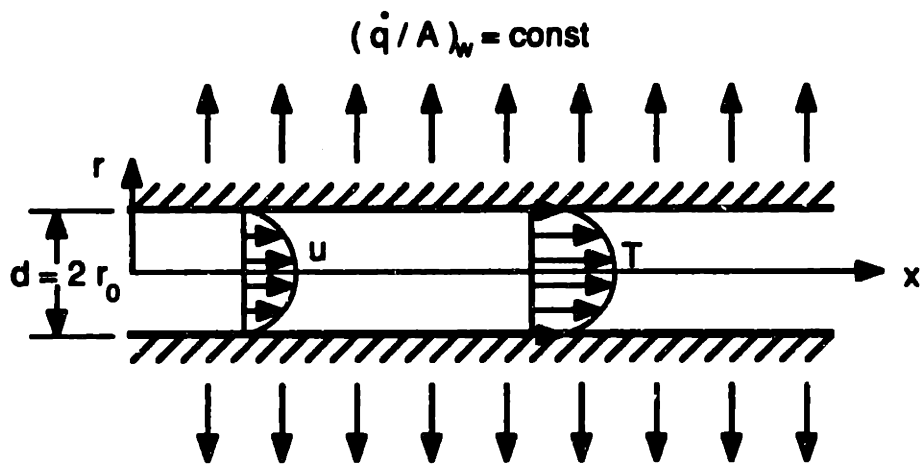


Figure 2.1 System description

## 2.2 Assumptions

In this section, several simplifying assumptions, necessary for the formulation of the cryogenic contamination problem into a mass transfer equation, are made and discussed. While most of the assumptions are applicable to practical helium systems as well as the system described in the previous section, a few assumptions may be true only for that specific system. Concerning that point, comments are made during the justifying discussion.

Basically, these assumptions begin with typical procedure of heat and mass transfer relation for a round tube or similar geometry. Momentum and heat transfer are then decoupled from mass transfer, which means in this problem that mass transfer does not affect momentum and heat transfer. In this manner, independently calculated velocity and temperature distributions can be used as prescribed conditions to obtain the concentration distribution.

**Assumption 1. Axial diffusion of heat and mass is zero.**

This assumption means that radial diffusion is much more dominant than the axial diffusion. It is based on the large ratio of length to diameter of the tube. From the equations of energy and mass (contaminant) balance and simple dimensional analysis, it can be easily shown that the ratio of radial to axial diffusion is equal to the order of the squared ratio of length to radius of the tube, which is about the order of  $10^4$  in typical heat exchangers and about  $10^7$  in our specific system. Therefore, this is a very good assumption.



**Assumption 2. The thermophysical properties of the gas mixture are represented by those of helium.**

Here, the thermophysical properties include density, specific heat, viscosity, and thermal conductivity. This is an extremely good assumption, because the typical order of contamination level in practical helium systems and in the specific system we are interested in is 10 to 100 ppm. In other words, mole fraction of helium in the mixture is about 99.999 to 99.999%, which means that the effect of mixture on the helium properties is negligible.

**Assumption 3. Total pressure drop throughout the tube is negligible.**

This assumption involves the simplifying procedure that the density of helium gas is a function of temperature and inlet pressure only. It should be noticed that gases in cryogenic systems cannot be considered incompressible due to large temperature variations. The compressibility due to temperature variation is much more dominant over that due to pressure variation. In other words, density at a specific location is determined by the inlet pressure and the local temperature. More quantitatively, density change of an ideal gas can be expressed as

$$d\rho = \frac{dP_t}{RT} - \frac{P_t}{RT^2} dT \quad (2.1)$$

where the first term on the right hand side is density change due to (total) pressure variation and the second term is due to temperature variation. To compare the order of those two contributions,  $(dP_t/P_t)/(dT/T)$  can be simply evaluated. For laminar flow through a tube, the pressure drop due to wall friction is

$$dP_i = - \frac{32 \mu u_m}{d^2} dx \quad (2.2)$$

Plugging Eqn. (2.2) into Eqn. (2.1) and rearranging,

$$\frac{dP_i}{P_i} / \frac{dT}{T} = \frac{32 \nu u_m}{R d^2} \left( -\frac{dT}{dx} \right)^{-1} \quad (2.3)$$

Even though the order of magnitude for Eqn. (2.3) is not immediately obvious, taking some representative numbers shows the value to be considerably small. For example, if  $u_m = 1$  m/sec,  $-dT/dx = 100$  K/m (moderate temperature gradient), and  $d = 0.001$  m (very small tube diameter), then the value of Eqn. (2.3) is about  $10^{-3}$ , which is approximately the same as in the experiment to be described later. In the operating conditions of practical helium systems, the value is much smaller because of the bigger tube diameter. Therefore, this assumption can be taken as valid for almost every cryogenic system.

**Assumption 4.** Gas mixture is a binary Gibbs-Dalton mixture of ideal gases.

This assumption is associated with the concept of partial pressure of a contaminant. As a description of a gas mixture, the Gibbs-Dalton model<sup>37,38</sup> (which assumes that gases exist separately at the same volume and temperature of the mixture) is known as acceptable in most engineering applications. According to the model,

$$P_{\text{total}} = P_{\text{helium}} + P_{\text{contaminant}}, \quad (2.4)$$

and

$$P_{\text{contaminant}} = y_{\text{contaminant}} P_{\text{total}}, \quad (2.5)$$

where  $P_{\text{total}}$  is the total pressure of the mixture,  $P_{\text{helium}}$  and  $P_{\text{contaminant}}$  are the partial pressures of helium and contaminant, respectively, and  $y_{\text{contaminant}}$  is the mole fraction of contaminant. As mentioned in Assumption 2 discussion, the mole fraction of contaminant is so small that the total pressure may be considered as equivalent to the partial pressure of helium, denoted by  $P_t$ , and the partial pressure of contaminant is denoted by  $P$ , simply for convenience.

**Assumption 5. The diffusion-thermo (Dufour) effect and thermal-diffusion (Soret) effect are negligible.**

This assumption is a part of decoupling heat and mass transfer, and is an extremely good assumption. Kays and Crawford <sup>43</sup> and Eckert and Drake <sup>40</sup> discussed these coupling effects. These effects are utilized only for rare cases such as isotope separation or a mixture of low density gases with very low molecular weight ( $H_2$ , He).

**Assumption 6. The mass accumulated on the wall does not affect the fluid flow environment.**

This assumption implies another decoupling of heat and mass transfer and simplifying the problem as near-steady. Validity of this assumption depends on the relative time of contamination with respect to its accumulation rate and geometrical dimensions. Since there is no solid information on the wall-condensed state, it is difficult to verify the validity strictly. On the other hand, it is the intent of this study to understand the

mechanism for contaminant accumulation, so interest here and in the experiment is for a relatively short period of contamination. It should be noted that this assumption is good enough in this specific mass transfer analysis, but not necessarily true in a relatively long-time operation or clogging-up mechanism of general helium systems.

**Assumption 7. Latent heat of sublimation of contaminant does not affect the temperature field.**

This assumption is again intended to decouple the heat and mass transfer. It is true simply because the amount of contaminant is so small that the heat transfer due to the phase transition of the contaminant is negligibly small when compared with the heat transfer according to the system component performance. More specifically, this assumption can be justified by the following argument. The total amount of heat transfer per unit length in helium systems is expressed as

$$\dot{q} = \rho c_p u_m A \left( -\frac{dT}{dx} \right) - \dot{M}_{acc} H_{ig} \quad (2.6)$$

The ratio of the second term on the right hand side to the first indicates the relative importance of the latent heat of sublimation. The ratio is on the order of  $10^{-3}$  for the condition taken in the discussion of Assumption 3 and with 100 ppm contamination of carbon dioxide. Again, this value is much smaller in the typical operating condition of practical helium systems.

**Assumption 8. Radial distribution of helium density and radial velocity are neglected.**

**This assumption intends to simplify the governing equations. The validity of this assumption can be verified by dimensional analysis. The ratio of radial variation to axial variation of helium density is on the order of the ratio of tube diameter to tube length. According to Assumption 3, density is dependent only on the temperature, while the ratio of radial to axial variation of temperature is the order of the ratio of diameter to length of the tube. The order of radial velocity can be estimated in a similar way. Another aspect of this assumption is that the boundary conditions of density and radial velocity at the tube wall are not significant for the solution of the governing equations so that their radial contribution can be neglected in observing the contamination behavior.**

**Most of the assumptions introduced above seem to be trivial in the sense that they are accepted in many engineering problems concerning transport phenomena without any detailed verification. In this specific study, however, a very important implication of the assumptions is that the mass transfer in cryogenic contamination mechanism is reasonably considered as a secondary transport phenomenon, subject to momentum and heat transfer**

## **2.3 Formulation and Solution**

**Based upon the assumptions in the previous section, the system described in Sec. 2.1 is formulated into a mass transfer problem and analytically solved in this section. For the given fully-developed velocity and temperature distributions, concentration of a contaminant is governed by a steady 2-D convection-diffusion equation. Since the boundary condition at the wall is not uniform along the axial direction, the equation is first solved for an arbitrary step wall-boundary condition. Later, a solution for the non-uniform boundary condition is found by a superposition integral of the step solution. From the concentration distribution, the wall-accumulation rate and the dimensionless mass transfer coefficient (which is the Sherwood number, denoted by  $Sh$ ) are obtained.**

**In addition to the assumptions of the previous section, it is temporarily assumed in this section that no snow forms even though super-sublimation (higher concentration than the sublimation concentration at the temperature of that location) occurs in the mass transfer process.**

### **2.3.1 Governing Equation and Boundary Conditions**

**According to Assumptions 5, 6, and 7, momentum and heat transfer are not coupled with mass transfer. Therefore, velocity and temperature distributions are found first, independently from the concentration distribution, and are then used to derive the governing equation of mass transfer with its boundary conditions.**

As described in Sec. 2.1, the temperature distribution of gas in a fully-developed laminar flow is assumed to be axially linear in the interesting range. This temperature as a function of  $x$  and  $r$  can be immediately derived from the energy balance equation with a parabolic velocity distribution. The result is

$$T(x,r) = T_w(x) + \frac{2\rho c_p u_m r_0^2}{k} \left(-\frac{dT_w}{dx}\right) \left\{ \frac{3}{16} + \frac{1}{16} \left(\frac{r}{r_0}\right)^4 - \frac{1}{4} \left(\frac{r}{r_0}\right)^2 \right\} \quad (2.7)$$

where

$$-\frac{dT_w}{dx} = \text{Const} \quad (2.8)$$

or

$$T_w(x) = T_w(0) - \left(-\frac{dT_w}{dx}\right) x \quad (2.9)$$

and  $\rho$ ,  $c_p$ ,  $k$ ,  $u_m$ , and  $r_0$  are the density, specific heat at constant pressure, thermal conductivity of helium, mean flow velocity, and the radius of the tube, respectively. It is noted that even though  $\rho$  and  $u_m$  are functions of  $x$ , their product is constant from the continuity of helium. The mean temperature of gas for a given  $x$  can be found from Eqn. (2.7) as following.

$$T_m(x) = T_w(x) + \frac{11}{48} \frac{\rho c_p u_m r_0^2}{k} \left(-\frac{dT_w}{dx}\right) \quad (2.10)$$

It may be noticed that the second term of the right-hand side of Eqn. (2.10) is a constant value. Now the Eqns. (2.9) and (2.10) are used as a part of the boundary condition for the mass transfer equation of contaminant and

temperature dependent properties such as density or mass diffusivity throughout this analysis.

With Assumptions 3 and 8, the velocity distribution can be found. For the fully developed flow in a tube, axial velocity is expressed as a parabolic shape

$$u(x,r) = 2 u_m(x) \left\{ 1 - \left( \frac{r}{r_0} \right)^2 \right\} \quad (2.11)$$

The mean axial velocity,  $u_m$ , is simply obtained from the continuity equation of helium together with Assumption 8.

$$u_m(x) \rho(x) = \text{Const} \quad (2.12)$$

where density of helium is given as a function of  $x$  only. From Assumption 3 and the ideal gas state equation,

$$\frac{u_m(x)}{T_m(x)} = \text{Const} \quad (2.13)$$

Now a differential equation for the mass balance of contaminant is ready to be derived since all the prescribed conditions are obtained. Using the coordinate systems shown in Figure 2.1, where  $x=0$  is selected as the sublimation starting point at wall, the desired differential equation is derived by considering a control volume of differential annular shape as shown in Figure 2.2. Mass flux through the axially facing surfaces is only with convection according to Assumption 1, and mass flux through the radially facing surfaces is



only with mass diffusion according to Assumption 8. Therefore, the mass balance of the contaminant is written as

$$\frac{\partial (u c)}{\partial x} = \frac{1}{r} \frac{\partial}{\partial r} \left( D r \frac{\partial c}{\partial r} \right), \quad (2.14)$$

where

$c = c(x,r)$ , concentration of contaminant, unknown

$u = u(x,r)$ , axial velocity, given by Eqn. (2.11)

$D = D(x)$ , mass diffusivity of contaminant in helium

The mass diffusivity of contaminant is generally a function of temperature and total pressure. However, Assumption 3 eliminates the total pressure dependence and similar reasoning with Assumption 4 yields to neglect the radial variation. As a result, mass diffusivity is dependent on the mean temperature or function of  $x$  only. Using this and Eqn. (2.11) in Eqn. (2.14) gives the desired governing differential equation, which is

$$2 \left\{ 1 - \left( \frac{r}{r_0} \right)^2 \right\} \frac{\partial (u_m(x) c)}{\partial x} = \frac{D(x)}{r} \frac{\partial}{\partial r} \left( r \frac{\partial c}{\partial r} \right) \quad (2.15)$$

Since this equation is first order in the  $x$  direction and second order in the  $r$  direction, one boundary condition in  $x$  direction and two boundary conditions in  $r$  direction are required to solve. Those boundary conditions are given as following:

$$c(x=0, r) = c_0 = \frac{y_0 P_t}{R T_w(0)} \quad 0 \leq r \leq r_0 \quad (2.16)$$

$$\frac{\partial c}{\partial r} (x, r=0) = 0 \quad x \geq 0 \quad (2.17)$$

$$c(x, r=r_0) = c_s(x) = \frac{P_s(T_w)}{RT_w(x)} \quad x \geq 0, \quad (2.18)$$

where  $c_s$  is the sublimation concentration at  $T_w$ .

Eqn. (2.16) is an inlet condition for the contaminant concentration.  $P_1$  is the inlet total pressure and  $y_0$  is the inlet mole fraction of contaminant. Before the contaminant reaches its sublimation temperature, there is no virtual mass transfer, so the concentration is uniform across the cross section of the tube at the sublimation starting point at wall. Again it is noted that  $x$  coordinate was selected zero at the sublimation starting point.

The two boundary conditions required in the radial direction are Eqn. (2.17) and Eqn. (2.18). The former imposes the symmetry around the axial axis due to no peripheral variation in this problem. An alternative boundary condition for Eqn. (2.17) is " $c(x, r=0) = \text{finite}$ ", which results in the same solution because both of these are used to take one of two solutions in the  $r$ -directional equation introduced later. The latter is the driving condition of this mass transfer phenomenon. It is not difficult to notice that, in a negative temperature gradient field in the flow direction, wall side of the fluid is colder than the middle of the tube and gaseous contaminant starts to sublime into a solid phase at the wall. This results in a deformed concentration profile so that the mass transfer occurs from that sublimation starting point ( $x=0$ ). Therefore, for  $x \geq 0$ , there is a phase equilibrium at the wall or concentration at  $r=r_0$  is taken as its sublimation concentration, which is shown as Eqn. (2.18).

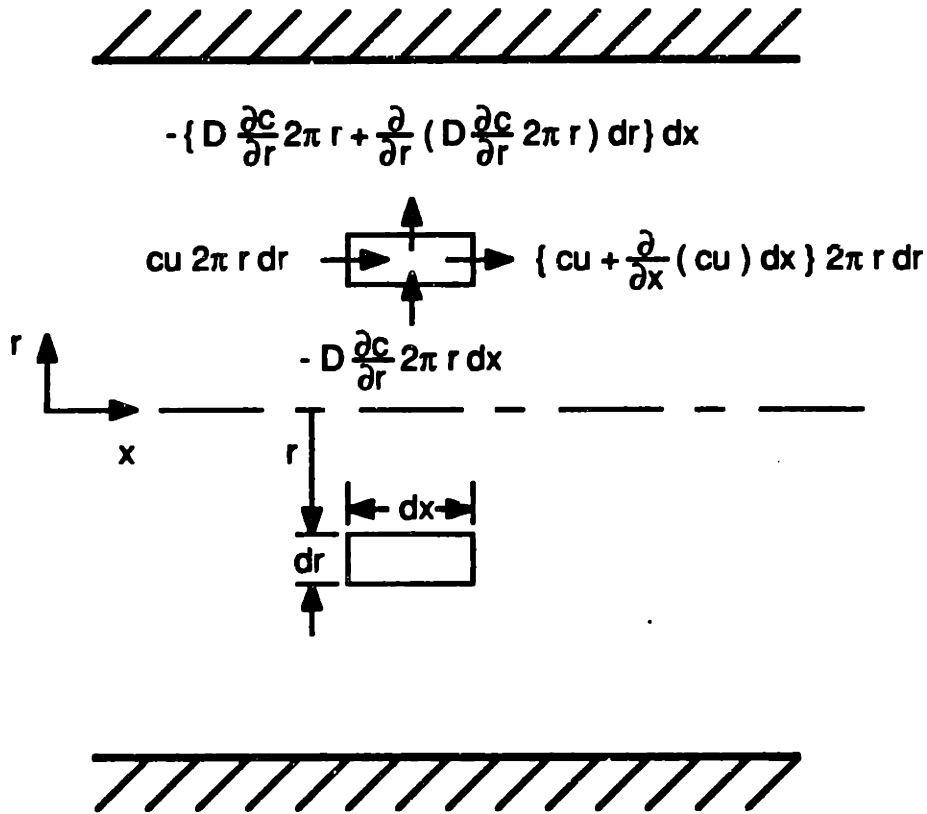


Figure 2.2 Control Volume of Differential Element

### 2.3.2 Solution for the Concentration of Contaminant

In this sub-section, the partial differential equation, Eqn. (2.15), with boundary conditions, Eqns. (2.16) to (2.18), is analytically solved. Eqn. (2.15) is a linear and homogeneous second order equation, and can be solved by the method of separation of variables. Difficulties arise, however, because of the non-uniform boundary condition Eqn. (2.18). It may be observed that since there is an  $x$ -dependence in that boundary condition, the differential equation cannot render a Sturm-Liouville type of series solution in a direct way. One of the ways to overcome the difficulties is to get a solution for a step wall boundary condition (which is  $x$  independent) and take the  $x$  dependence with a superposition integral of infinitesimal steps. 8, 9, 12

To achieve the step solution, boundary condition Eqn. (2.18) is replaced by

$$c(x, r=r_0) = c_1 \quad x \geq 0, \quad (2.19)$$

where  $c_1$  is an arbitrary constant. At this point, Eqn. (2.15) to (2.17) and Eqn. (2.19) are non-dimensionalized to get two homogeneous boundary conditions. Definitions of the dimensionless variables are

$$\tilde{r} = \frac{r}{r_0} \quad \tilde{x} = \frac{x}{r_0} \quad \tilde{c}(\tilde{x}, \tilde{r}) = \frac{c(x,r) - c_1}{c_0 - c_1} \quad \tilde{u}(\tilde{x}) = \frac{u_m(x)}{u_m(0)} \quad \tilde{D}(\tilde{x}) = \frac{D(x)}{2 r_0 u_m(0)} \quad (2.20)$$

Then, the governing equation becomes

$$(1 - \tilde{r}^2) \frac{\partial(\tilde{u}(\tilde{x}) \tilde{c})}{\partial \tilde{x}} = \frac{\tilde{D}(\tilde{x})}{\tilde{r}} \frac{\partial}{\partial \tilde{r}} \left( \tilde{r} \frac{\partial \tilde{c}}{\partial \tilde{r}} \right) \quad (2.21)$$

with boundary conditions

$$\tilde{c}(\tilde{x}=0, \tilde{r}) = 1 \quad (2.22)$$

$$\frac{\partial \tilde{c}}{\partial \tilde{r}}(\tilde{x}, \tilde{r}=0) = 0 \quad (2.23)$$

$$\tilde{c}(\tilde{x}, \tilde{r}=1) = 0, \quad (2.24)$$

where two homogeneous boundary conditions in the  $r$  direction are obtained. Now this set of equation can be directly solved by separation of variables. By letting

$$\tilde{c}(\tilde{x}, \tilde{r}) = X(\tilde{x}) R(\tilde{r}), \quad (2.25)$$

two sets of ordinary differential equations are obtain.

$$(\tilde{u} X)' + \lambda^2 \tilde{D} X = 0 \quad (2.26)$$

$$\tilde{r} R'' + R' + \lambda^2 \tilde{r} (1 - \tilde{r}^2) R = 0$$

$$\text{with } R'(0)=0, R(1)=0 \quad (2.27)$$

Eqn. (2.27) is the characteristic equation of partial differential equation, determining the eigen-values and eigen-functions for Sturm-Liouville type of series solution. It is so called Graetz equation and its eigen-functions are called Graetz functions. When this equation is compared with the zeroth order Bessel equation (which characterizes the diffusion in a round tube), it has  $r(1-r^2)$  as a

weight function instead of  $r$ . In this sense, the Graetz equation can be called a parabolic velocity weighted equation over the Bessel equation. As can be expected, asymptotic behavior of the Graetz function near  $r=0$  is the Bessel function, because they have asymptotically same weight function near the center of the tube. Details of Graetz equation, its solution, and properties are presented in Appendix B.

Solving Eqn. (2.26) and Eqn. (2.27) with denoting the  $n$ -th eigen-function and eigen-value as  $R_n$  and  $\lambda_n$ , respectively, gives the solution of Eqn. (2.21) as follows:

$$\tilde{c}(\tilde{x}, \tilde{r}) = \sum_{n=0}^{\infty} a_n R_n(\tilde{r}) \frac{1}{\tilde{u}(\tilde{x})} \exp \left\{ - \int_0^{\tilde{x}} \frac{\lambda_n^2 \tilde{D}(\eta)}{\tilde{u}(\eta)} d\eta \right\} \quad (2.28)$$

where  $a_n$  is the  $n$ -th coefficient of series expansion of the function 1 (unity) in terms of Graetz function  $R_n$ , and is expressed as

$$a_n = \frac{\int_0^1 r(1-r^2) R_n(r) dr}{\int_0^1 r(1-r^2) R_n^2(r) dr} \quad (2.29)$$

Going back to the variables of real dimension by Eqns. (2.20), Eqn. (2.28) becomes

$$c(x,r) - c_1 = (c_0 - c_1) \sum_{n=0}^{\infty} a_n R_n\left(\frac{r}{r_0}\right) \frac{u_m(0)}{u_m(x)} \exp\left\{-\int_0^x \frac{\lambda_n^2 D(\eta)}{2 r_0^2 u_m(\eta)} d\eta\right\} \quad (2.30)$$

where  $a_n$ ,  $R_n$ , and  $\lambda_n$  are still remaining dimensionless, but dummy variable for integral,  $\eta$ , has been back to the length dimension. This is the solution of the partial differential equation Eqn. (2.15) with boundary conditions of Eqns. (2.16) and (2.17), and the step wall condition Eqn. (2.19).

To get the final solution for the non-uniform wall condition Eqn. (2.18), the remaining procedure is the superposition integral by taking the continuously varying wall condition as sum of many infinitesimal steps. For an infinitesimal step,  $\Delta c$  at  $x=\xi$ , shown in Figure 2.3 (a), solution of Eqn. (2.15) is simply found by substituting  $c_0+\Delta c$  for  $c_1$ , and 0 for  $\xi$ . The result is

$$c(x,r) - c_0 = \Delta c \left\{ 1 - \sum_{n=0}^{\infty} a_n R_n\left(\frac{r}{r_0}\right) \frac{u_m(\xi)}{u_m(x)} \exp\left(-\int_{\eta=\xi}^x \frac{\lambda_n^2 D(\eta)}{2 r_0^2 u_m(\eta)} d\eta\right) \right\} \quad (2.31)$$

As shown in Figure 2.3 (b), for an arbitrary continuous wall condition  $c_w(x)$ , concentration distribution is found as a summation of infinitesimal steps or, in the limit, as an integral of its derivative. Therefore solution for the boundary condition Eqn. (2.18) is obtained as following.

$$c(x,r) = c_0 + \int_{\xi=0}^x \left\{ 1 - \sum_{n=0}^{\infty} a_n R_n\left(\frac{r}{r_0}\right) \frac{u_m(\xi)}{u_m(x)} \exp\left[-\int_{\eta=\xi}^x \frac{\lambda_n^2 D(\eta)}{2 r_0^2 u_m(\eta)} d\eta\right] \right\} \left(\frac{dc_w}{d\xi}\right) d\xi \quad (2.32)$$

or interchanging the order of integral and summation yields

$$c(x,r) = c_s(x) - \sum_{n=0}^{\infty} a_n R_n \left( \frac{r}{r_0} \right) \int_{\xi=0}^x \frac{u_m(\xi)}{u_m(x)} \exp \left\{ - \int_{\eta=\xi}^x \frac{\lambda_n^2 D(\eta)}{2 r_0^2 u_m(\eta)} d\eta \right\} \frac{dc_s}{d\xi} d\xi \quad (2.33)$$

This is the final solution for the governing equation derived in the previous subsection. In this equation,  $c_s(x)$  is the sublimation concentration at the wall and equal to  $c_w(x)$ .

A few observations can be made about the solution, Eqn. (2.33). The right hand side of the equation has two terms, the first of which is the contaminant concentration at the wall and the most dominant term in magnitude. The second term is the radial variation from the wall concentration and is relatively small in magnitude. It should be noted that the radial variation is a function of  $x$  as well as  $r$ . This means that the problem is concerned with the mass transfer entry region for the already fully developed velocity and temperature field. The second observation is the limiting case of infinite mass transfer rate. As  $D(x)$  goes to infinity, the second term of Eqn. (2.33) converges to zero so that concentration is the sublimation concentration at the wall temperature everywhere, which is the obvious result and is exactly same as the zeroth-order analysis of the previous chapter. The final observation concerns the simplified expression for the negligible temperature dependence of velocity and mass diffusivity, which is true for small  $x$  near the sublimation starting point. In this case, Eqn. (2.33) is simplified as

$$c(x,r) = c_s(x) - \sum_{n=0}^{\infty} a_n R_n \left( \frac{r}{r_0} \right) \int_{\xi=0}^x \exp \left\{ - \frac{\lambda_n^2 D}{2 r_0^2 u_m} (x - \xi) \right\} \frac{dc_s}{d\xi} d\xi \quad (2.34)$$



In this equation, the exponent inside of integral can be expressed in terms of

dimensionless variables as  $-\frac{\lambda_n^2}{\text{Re Sc}} \frac{x-\xi}{r_0}$ , where Re is the Reynolds number based on the tube diameter,  $u_m d/v$ , and Sc is the Schmidt number,  $v/D$ . Product of those two numbers is sometimes called mass transfer Peclet number (denoted by  $\text{Pe}_m$ ) in parallel with heat transfer, where Peclet number is the product of Reynolds and Prandtl numbers. What should be noted in this expression is that x-dependence of radial variance in concentration involves this  $(\text{Re Sc})$ . This variable is frequently used in the entry region analysis, as will be shown later.

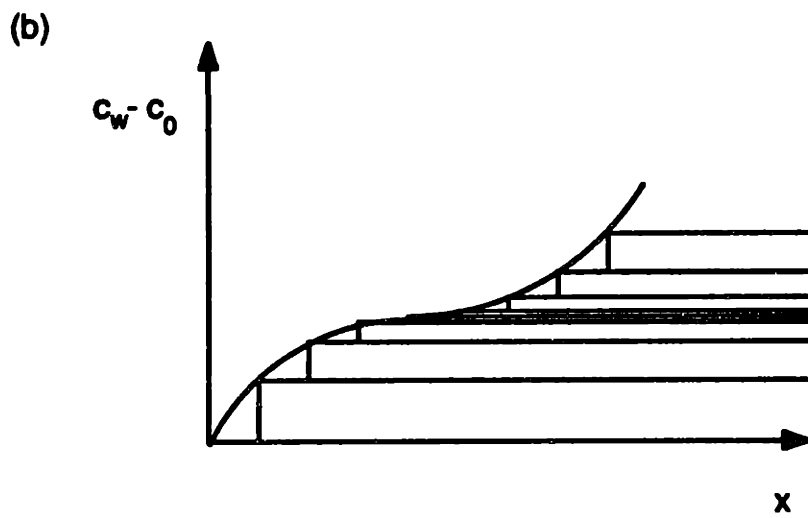
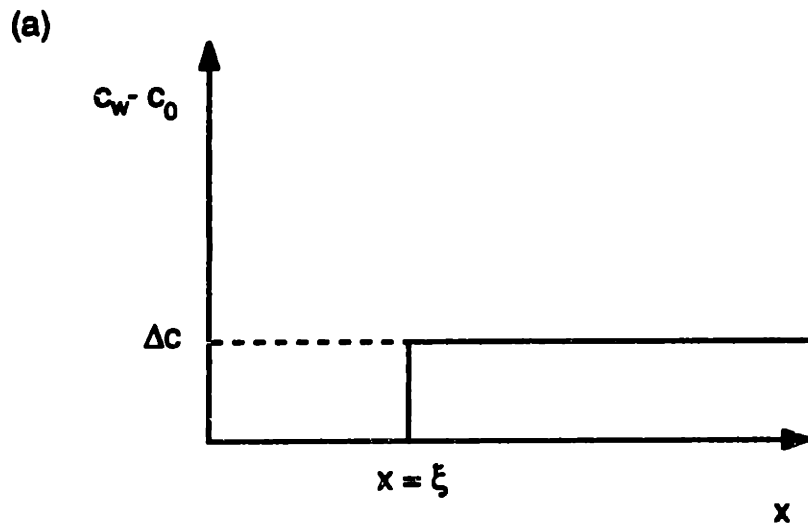


Figure 2.3 Superposition Integral of Infinitesimal Steps

### 2.3.3 Wall Accumulation Rate without Snow Formation

The solution for the concentration of contamination found in the previous sub-section is used to calculate the wall accumulation rate. This calculation is significant because the wall accumulation is not only the detrimental effect of contamination but also an experimentally verifiable quantity. It is emphasized again that this wall accumulation calculation is under the assumption of no snow formation in spite of super-saturation.

Mass accumulation rate per unit length is equal to mass flux times its peripheral length.

$$\dot{M}_{acc} = -2\pi r_0 D(x) \left( \frac{\partial c}{\partial r} \right)_{r=r_0}, \quad (2.35)$$

where  $\dot{M}_{acc}$  has the dimension of mass per time per length. Substitution of Eqn. (2.33) for Eqn. (2.35) yields

$$\dot{M}_{acc}(x) = 2\pi D(x) \sum_{n=0}^{\infty} a_n R_n'(1) \int_{\xi=0}^x \frac{u_m(\xi)}{u_m(x)} \exp \left\{ - \int_{\eta=\xi}^x \frac{\lambda_n^2 D(\eta)}{2 r_0^2 u_m(\eta)} d\eta \right\} \frac{dc_s}{d\xi} d\xi \quad (2.36)$$

From Appendix B,

$$a_n R_n'(1) = -2.02552 \lambda_n^{-1/3} \quad (2.37)$$

Mass accumulation is positive because both  $a_n R_n'(1)$  and  $dc_s/d\xi$  are negative. Although numerical evaluation of  $c(x,r)$  is not easy because the eigen-functions,

$R_n$ , are not expressed in a closed form, mass accumulation rate is relatively handy with Eqn. (2.37).

Using some computational techniques, the mass accumulation rate of carbon dioxide has been calculated for several flow rates and temperature gradients. The details of the procedure including the computer program are given in Appendix C. Three of the results are presented in Figures 2.4 to 2.6, together with the zeroth-order solution introduced in Chapter 1. They have the same temperature gradient ( $dT/dx = -100$  K/m), the same total pressure ( $P_t = 202.65$  KPa = 2 atm), and the same contamination level ( $y_{in} = 100$  ppm), but different flow rates. The flow rate is shown in each graph in terms of  $Re$ ; at small  $Re$ , mass accumulation almost coincides with the zeroth order solution and at higher  $Re$ , an overshoot occurs. The peak accumulation reaches about 87% of the zeroth order peak for  $Re=10$ , about 65% for  $Re=100$ , and about 27% for  $Re=1000$ .

The dimensionless number which concerns the mass accumulation rate is the Sherwood number. Complete non-dimensionalization is presented in the next sub-section.

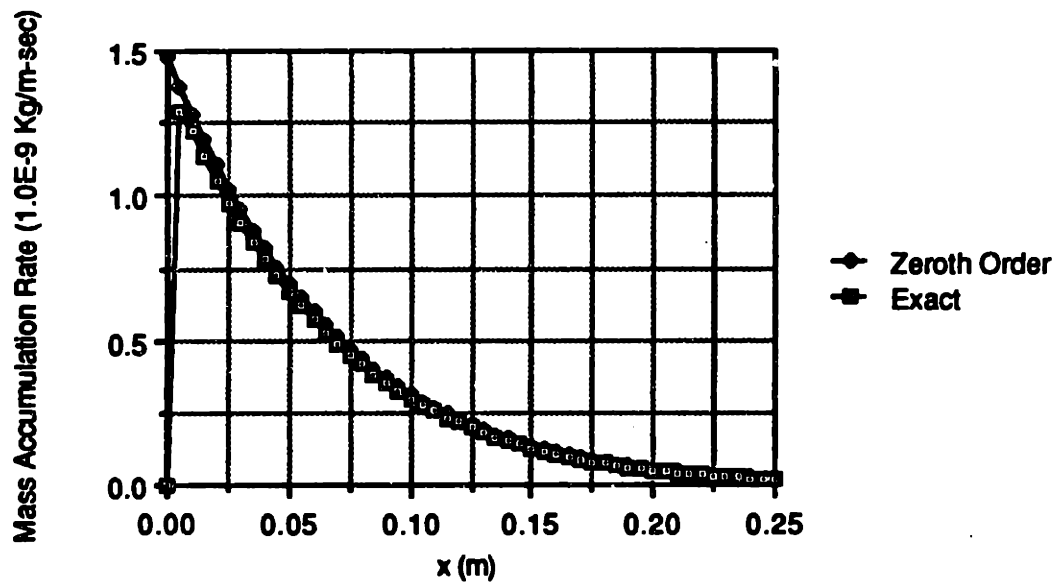


Figure 2.4 Mass Accumulation Rate for  $Re = 10$

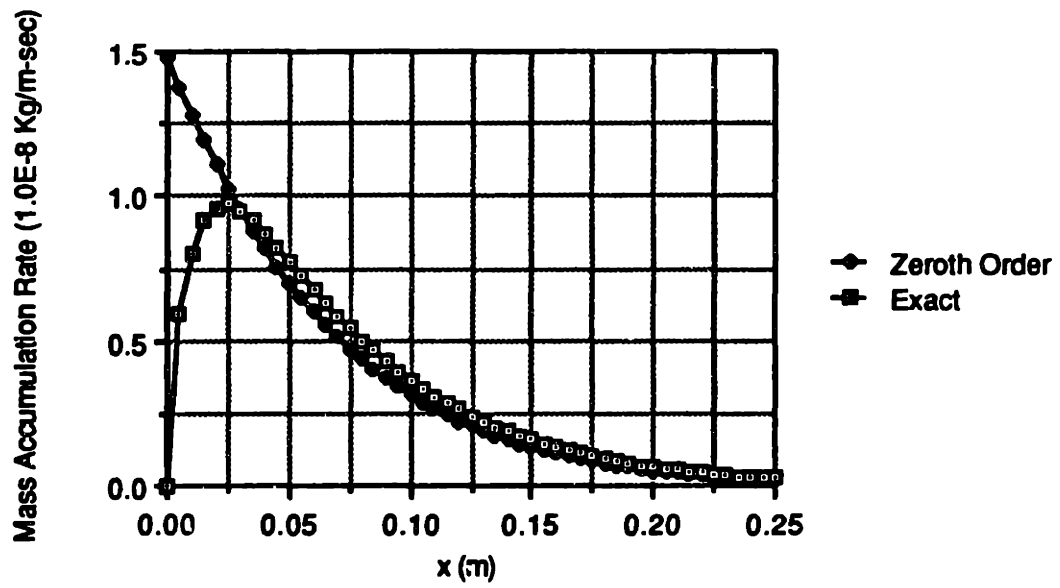


Figure 2.5 Mass Accumulation Rate for  $Re = 100$

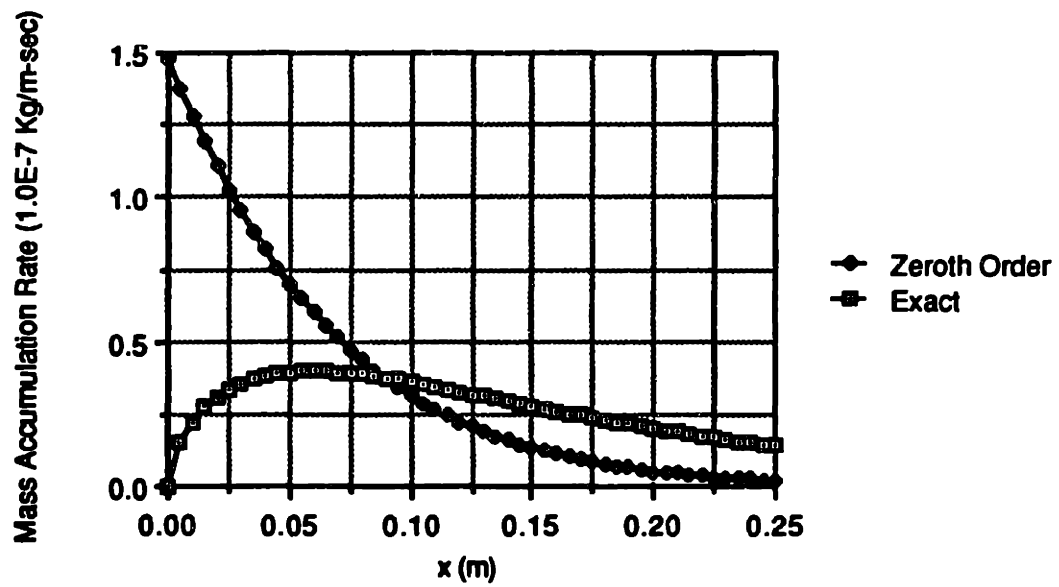


Figure 2.6 Mass Accumulation Rate for  $Re = 1000$

### 2.3.4 Mass Transfer Coefficient and Sherwood Number

A convenient variable to characterize the mass transfer in the entry region and the wall accumulation is the mass transfer coefficient,  $h_D$ , which is defined using a mean concentration, similarly to the mean temperature used to define the heat transfer coefficient in heat transfer.

$$\frac{\dot{m}_{acc}}{A} = h_D (c_m - c_w) \quad (2.38)$$

The mean concentration,  $c_m$ , is defined as

$$c_m = \frac{\int_A c u dA}{\int_A u dA} \quad (2.39)$$

where  $A$  is the cross-sectional area of the tube. Therefore, the expression for the mass transfer coefficient is given by

$$h_D(x) = \frac{D(x) \left( -\frac{\partial c}{\partial r} \right)_{r=r_0}}{c_m(x) - c_w(x)} \quad (2.40)$$

Note that  $h_D$  has the dimension of velocity, m/sec. The dimensionless number of the mass transfer coefficient is the Sherwood number,  $Sh$ , which is comparable to the Nusselt number in heat transfer. The local Sherwood number is defined as



$$\text{Sh}(x) = \frac{h_D(x) d}{D(x)} \quad (2.41)$$

Since the analytical solution for concentration is already found, the local Sherwood number is readily derived. The numerator of Eqn. (2.40) is given by Eqn. (2.36) and the denominator can be obtained from Eqns. (2.34) and (2.39). In calculation and simplification for the mean concentration, one of the properties, derived from the characteristic equation, Eqn. (2.27),

$$\int_0^1 r (1 - r^2) R(r) dr = -\frac{1}{\lambda^2} R'(1) \quad (2.41)$$

is useful. Final expression for the local Sherwood number is

$$\text{Sh}(x) = \frac{\sum_{n=0}^{\infty} \lambda_n^{-1/3} \int_{\xi=0}^x \frac{u_m(\xi)}{u_m(x)} \exp \left\{ - \int_{\eta=\xi}^x \frac{\lambda_n^2}{\text{Re}(\eta) \text{Sc}(\eta)} \frac{d\eta}{r_0} \right\} \frac{dc_s}{d\xi} d\xi}{2 \sum_{n=0}^{\infty} \lambda_n^{-7/3} \int_{\xi=0}^x \frac{u_m(\xi)}{u_m(x)} \exp \left\{ - \int_{\eta=\xi}^x \frac{\lambda_n^2}{\text{Re}(\eta) \text{Sc}(\eta)} \frac{d\eta}{r_0} \right\} \frac{dc_s}{d\xi} d\xi}, \quad (2.42)$$

where Eqn. (2.37) has been used. This is the complete and the most general Sherwood number expression for cryogenic contamination. It is observed that Eqn. (2.42) is good for any kind of temperature gradient

One set of calculated Sherwood numbers is drawn for  $x/d$  in Figure 2.7, where  $(\text{Re Sc}) = 33.0$  at  $x=0$ ,  $dT_w/dx = -75.0$  K/m,  $d = 0.001$  m, and contaminant is 100 ppm of carbon dioxide in 1.88 atm total pressure. This is one of the experimental conditions, discussed in later chapters. In Figure 2.7, Sherwood number starts from infinity at the sublimation starting point and appears to

converge gradually to about 4.3. The infinity Sh at  $x=0$  is due to a sudden (mathematically non-differentiable) change of wall boundary condition at  $x=0$ . The value of Sh at large  $x$  is not really converging to a certain constant, because the wall boundary condition is changing continuously even if its change is getting smaller as  $x$  increases. Therefore the mass transfer can not be fully developed in the exact sense.

Concerning the Sherwood number and Eqn. (2.42), several discussions are presented at this point. When the temperature dependences of axial mean velocity and the mass diffusivity are neglected, Eqn. (2.42) can be tremendously simplified. This simplification is good along the points not far from the sublimation starting point,  $x=0$ . In this case, the integral at the inside of exponential function is simply performed.

$$\text{Sh}(x) = \frac{\sum_{n=0}^{\infty} \lambda_n^{-1/3} \int_{\xi=0}^x \exp\left(-\frac{\lambda_n^2}{\text{Re Sc}} \frac{x-\xi}{r_0}\right) \frac{dc_s}{d\xi} d\xi}{2 \sum_{n=0}^{\infty} \lambda_n^{-7/3} \int_{\xi=0}^x \exp\left(-\frac{\lambda_n^2}{\text{Re Sc}} \frac{x-\xi}{r_0}\right) \frac{dc_s}{d\xi} d\xi} \quad (2.43)$$

There are four dimensionless groups affecting the local Sherwood number: the Reynolds number, Schmidt number, dimensionless axial distance, and dimensionless wall concentration corresponding to the temperature gradient. The Reynolds number and the Schmidt number always show up as a product. Physically,  $(\text{Re Sc})$  means the ratio of flow rate to radial mass diffusion rate. The reason for dimensionless axial distance is, of course, because the problem is dealing with the entry region and wall condition is generally non-uniform. Wall

sublimation concentration can be non-dimensionalized by any concentration value, such as inlet concentration, because it appears both in the numerator and denominator. This dimensional discussion is equally true for the exact expression of  $Sh(x)$ , Eqn. (2.42), but it is mentioned here because it is more visible after the simplification into Eqn. (2.43).

If it is further assumed that wall temperature is given such that the wall concentration is varying linearly (of course, this is not a realistic assumption), then Eqn. (2.43) is more simplified to

$$Sh(x) = \frac{\sum_{n=0}^{\infty} \lambda_n^{-7/3} \left\{ 1 - \exp\left(-\frac{\lambda_n^2 x}{Re Sc r_0}\right) \right\}}{2 \sum_{n=0}^{\infty} \lambda_n^{-13/3} \left\{ 1 - \exp\left(-\frac{\lambda_n^2 x}{Re Sc r_0}\right) \right\}} \quad (2.44)$$

A special interest for this unrealistic case is in its behavior at large  $x$ ,

$$Sh = \frac{\sum_{n=0}^{\infty} \lambda_n^{-7/3}}{2 \sum_{n=0}^{\infty} \lambda_n^{-13/3}} \quad (2.45)$$

It can be shown that Sherwood number in Eqn. (2.45) approaches 4.36. This is a well-known Nusselt number for the fully developed flow with constant wall heat flux boundary condition. Obviously, from an analogy between such a heat transfer problem and this particular mass transfer problem, the Sherwood number should be and, indeed, turns out to be 4.36. It may be reminded that Eqn. (2.45) is a result from series expansion of wall accumulation in terms of

eigen-values and eigen-functions of a Sturm-Liouville type of equation, Eqn. (2.27). Therefore, Eqn. (2.45) is one of the exact (and complicated) expressions of 4.36 (which is actually 48/11) expanded with those eigen-values and eigen-functions. It is again stressed that this paragraph is not directly related with current contamination analysis.

The next discussion is about the heat and mass transfer analogy. As already mentioned, the above mass transfer is analogous to a certain heat transfer which has temperature boundary conditions corresponding to the concentration boundary conditions Eqns. (2.16) to (2.18). It should be noted carefully that there is no analogy between the mass transfer and the heat transfer occurring in this current system. Therefore the Colburn j-factor analogy type of analysis is not applicable here. Especially for small  $x$ , the behaviors of heat and mass transfer are apparently different from each other. For large  $x$ , however, the Sherwood number varies very slowly as shown in Figure 2.7, even though it does not approach a final value, and as a result, there is a near-similarity between two transport phenomena.

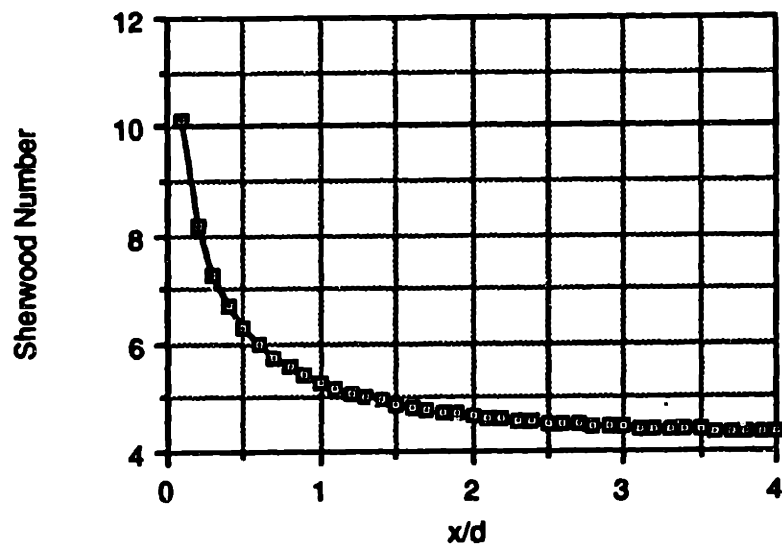


Figure 2.7 Local Sherwood Number Distribution

### 2.3.5 Mass Transfer Entry Length

Particular attention in this sub-section is paid to the behavior of the Sherwood number in the mass transfer entry region (near  $x=0$ ) and the evaluation of the so-called entry length which is defined as the distance for the mass transfer boundary layer to grow and meet each other. It starts from a 1-D wall accumulation expression using the mass transfer coefficient,  $h_D(x)$ . By considering a control volume shown in Figure 2.8, mass balance and mass transfer rate equation can be written as

$$\dot{M}_{acc} = A \frac{d}{dx} \{ u_m(x) c_m(x) \} \quad (2.46)$$

and

$$\dot{M}_{acc} = \pi d h_D(x) \{ c_m(x) - c_w(x) \} \quad (2.47)$$

respectively. In Eqn. (2.46),  $A$  is the cross-sectional area of tube,  $\pi d^2/4$ . Combining Eqns. (2.46) and (2.47) together with the wall concentration,

$$c_w(x) = \frac{P_s(x)}{R T_w(x)} \quad (2.48)$$

and Eqn. (2.13), yields

$$\frac{d}{4} \frac{d}{dx} \left\{ \frac{u_m(x) \dot{M}_{acc}(x)}{h_D(x)} \right\} + \dot{M}_{acc}(x) = \frac{A u_m(0)}{R T_w(0)} \left( - \frac{dP_s(x)}{dx} \right) \quad (2.49)$$

This is the desired 1-D equation for wall accumulation using mass transfer coefficient. An alternative method to get Eqn. (2.49) is the integration of Eqn.

(2.15) over the cross-section of the tube with boundary conditions. The first fact to notice in Eqn. (2.49) is that when  $h_D$  goes to infinity, the first term of left hand side vanishes so that the remaining part of equation becomes exactly the zeroth order equation, Eqn. (1.5).

The usefulness of Eqn. (2.49) is its capability to give an analytical expression for the mass transfer entry length,  $L_e$ , which is of main interest. Since Eqn. (2.49) is a linear first order differential equation, its characteristic length is comparable to the desired entry length.

$$L_e = \text{order of } \left( \frac{d u_m}{4h_D} \right) \quad (2.50)$$

or

$$L_e = \text{order of } \left( \frac{Re Sc}{Sh} d \right) \quad (2.51)$$

where  $Re$  can be taken as an averaged value over the entry length or simply any value (for example,  $Re(0)$ ) around that region, because the mean velocity does not vary very much in this short range. However, the difficulty is in the selection of  $Sh$ , which changes from infinity to a finite value in this entry region, as shown in Figure 2.7. Furthermore, the expression for the  $Sh(x)$ , Eqn. (2.42) or (2.43), is not analytically integrable to obtain the averaged Sherwood number, even though it is numerically integrable. The group of dimensionless numbers,  $Sh/(Re Sc)$ , is sometimes called the mass transfer Stanton number (denoted by  $St_m$ ), in parallel with Stanton number (denoted by  $St$ ), defined as  $Nu/(Re Pr)$  in heat transfer (especially when the Colburn-Reynolds analogy is mentioned).

To proceed to the analytical entry length expression, an asymptotic behavior of the Sherwood number near  $x=0$  is needed. A well-known method is so-called Lebeque approximation <sup>9</sup>, which assumes that the behavior near  $x=0$  is similar to that of flat plate. This approximation is good for small  $x$  when compared with radius of the tube. When there is a uniform flow over a flat plate and mass transfer starts at the point far from the leading edge, as shown in Figure 2.9, wall accumulation is expressed as

$$\left(\frac{\dot{m}}{A}\right)_w = \frac{0.339 D Sc^{1/3} Re_{x'}^{1/2}}{x'} \int_{x_0}^{x'} \left\{ 1 - \left(\frac{\xi'}{x'}\right)^{3/4} \right\}^{-1/3} \left(-\frac{dc_w}{d\xi'}\right) d\xi' \quad (2.52)$$

where  $Re_{x'}$  is Reynolds number based on  $x'$ , the distance from the leading edge and  $U_\infty$ , the free stream velocity, and  $x'$  is assumed much greater than  $x$ , the distance from the mass transfer starting point. Approximating by

$$\left(\frac{\xi'}{x'}\right)^{3/4} = \left(\frac{x_0 + \xi}{x_0 + x}\right)^{3/4} \approx \left(1 - \frac{x - \xi}{x_0}\right)^{3/4} \approx 1 - \frac{3}{4} \frac{x - \xi}{x_0} \quad (2.53)$$

and using the wall friction relation

$$C_f = \frac{\tau_w}{\rho U_\infty^2 / 2} = \frac{0.664}{Re_{x'}^{1/2}} \quad (2.54)$$

to eliminate  $x_0$ , yields

$$\left(\frac{\dot{m}}{A}\right)_w = 0.808 D Sc^{1/3} \left\{ \frac{1}{\nu} \left(\frac{\partial u}{\partial y}\right)_0 \right\}^{1/3} \left(-\frac{dc_w}{dx}\right)_0 x^{2/3} \quad (2.55)$$



where the wall concentration,  $c_w$ , has been linearized with its slope at  $x=0$  or  $x'=x_0$ . Taking

$$\left(\frac{\partial u}{\partial y}\right)_0 = \frac{8 u_m}{d} \quad (2.56)$$

Eqn. (2.55) is reduced to

$$\left(\frac{\dot{m}}{A}\right)_w = 1.617 D Sc^{1/3} Re^{1/3} \left(\frac{x}{d}\right)^{2/3} \left(-\frac{dc_w}{dx}\right)_0 \quad (2.57)$$

Substituting Eqn. (2.57) to the definition of Sherwood number with  $c_m = c_0$ , the asymptotic behavior near  $x=0$  is finally obtained as

$$Sh(x) = 1.617 (Re Sc)^{1/3} \left(\frac{d}{x}\right)^{1/3}, \text{ for } x = 0. \quad (2.58)$$

As expected, the Sh goes to infinity but is integrable at  $x=0$ . In Eqn. (2.58), there is no contribution of wall concentration, since it has been linearized with its gradient at  $x=0$ . To validate this asymptotic behavior, one of the numerical values for Sherwood number is plotted in Figure 2.10, for the exact solution, Eqn.(2.42), and the Leveque approximation, Eqn. (2.59). The conditions of this calculation are same as those of Figure 2.7. A good agreement is observed for the range up to about  $x/d=2$  on the integration basis. A major reason for the faster decay of Leveque approximation is that it describes the behavior over a flat plate where boundary layer grows continuously, while the boundary layer stops growing after the entry region in the tube.

Returning to the evaluation of the entry length, an averaged Sherwood number can be used in Eqn. (2.51). Denoting the averaged Sh from  $x=0$  to  $l$  (any length) as  $\overline{Sh}(l)$ ,

$$\overline{Sh}(l) = \frac{1}{l} \int_0^l Sh(x) dx = \frac{3}{2} Sh(l) \quad (2.59)$$

From Eqns. (2.51), (2.58), and (2.59)

$$L_e = \frac{Re Sc}{4 \overline{Sh}(L_e)} d \quad (2.60)$$

or

$$L_e = 0.0332 (Re Sc) d \quad (2.61)$$

where  $\overline{Sh}(L_e)$  is a function of  $L_e$ , so Eqn. (2.60) has been solved for  $L_e$ . This final equation is the desired entry length. For the conditions in Figure 2.7, the entry length is about 1.1 times the diameter. As shown in Figure 2.10, the Lebeque approximation is good throughout this region and therefore Eqn. (2.61) is valid even though it is derived from an approximate relation. A physical meaning of the entry length is, from Eqn. (2.49), the distance, necessary for the wall accumulation to reach 63% of the final value at large  $x$  if the wall concentration is constant or near constant. The entry length gives a critical information about the degree of super-saturation and about the experimental results, later.

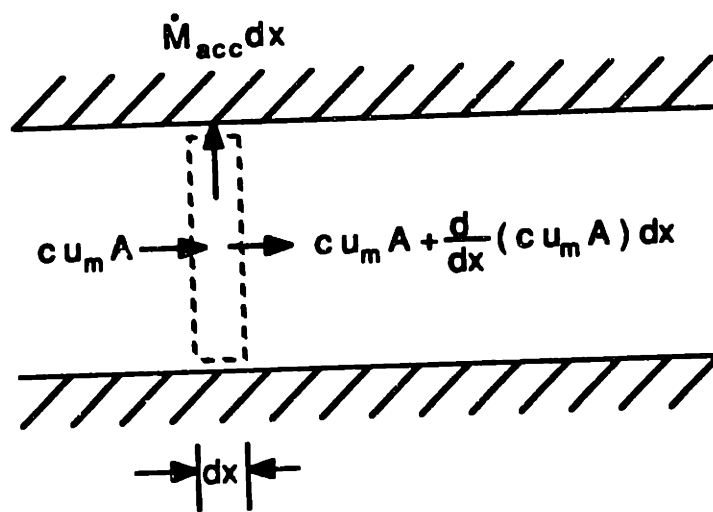


Figure 2.8 1-Dimensional Differential Control Volume

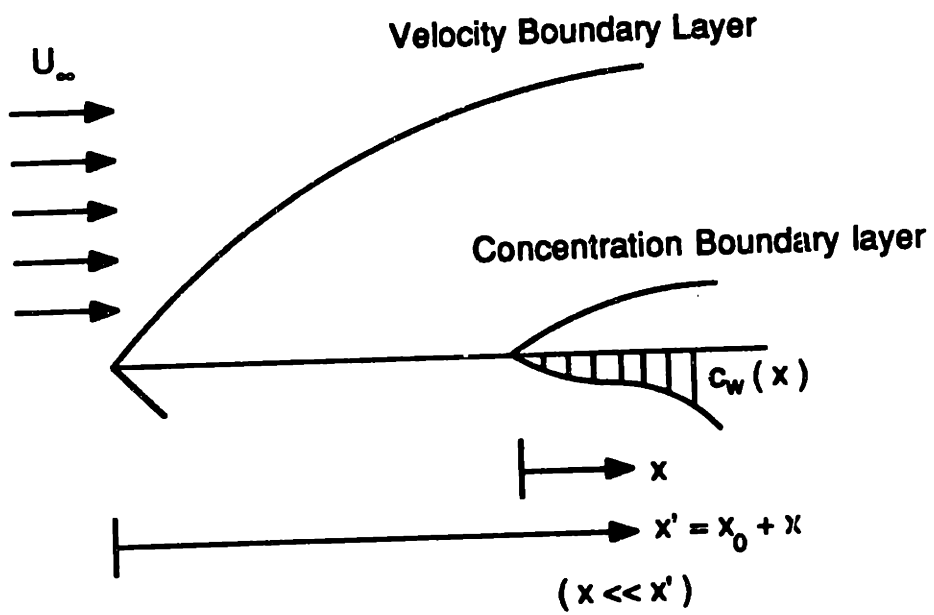


Figure 2.9 Boundary Layers on a Flat Plate

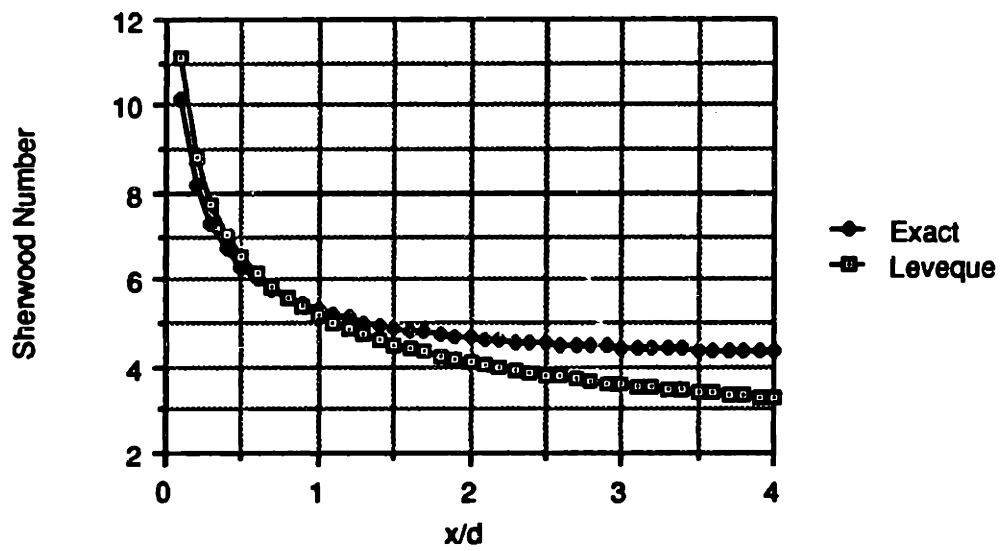


Figure 2.10 Leveque Approximation for the Sherwood Number at the Entry Region

## 2.4 Super-Saturation

Every analysis throughout the last section is presented under the assumption that there is no snow formation. As mentioned earlier, super-saturation (exactly speaking, super-sublimation - here super-saturation is used for convenience) always exists in the sublimation process for every positive wall-accumulation rate of contaminant, because heat transfer of helium is faster than the mass transfer of contaminant in helium as will be shown in the following sub-section. The characteristics of the super-saturation are reviewed and the degree of super-saturation is estimated. The purpose of this section is to provide a simple and reasonable method to predict the onset of snow formation and its location, so that it may be used to discuss the experimental results and draw critical conclusions on the behavior of contaminant in helium systems.

### 2.4.1 Lewis Numbers of Common Contaminants in Helium

Lewis number,  $Le$ , which is the ratio of thermal diffusivity to mass diffusivity

$$Le = \frac{\alpha}{D}, \quad (2.62)$$

is the most important property of contaminant in helium, in determining whether the super-saturation occurs or not. For the semi-fully developed temperature and concentration profiles (semi-fully developed flow means that their axial

variation is negligibly small to radial variation), the concentration of contaminant and its sublimation concentration at that temperature can be given by

$$c = c(x, r) \quad (2.63)$$

and

$$c_s = \frac{P_s(T(x,r))}{RT(x,r)}, \quad (2.64)$$

respectively. Their relative profiles have the shapes as shown in Figure 2.11, because both the concentration and temperature curves have the near-parabolic shapes, Eqn. (2.10), but sublimation pressure is essentially exponential function of temperature. Therefore, for Lewis number below unity, there is no super-saturation ( as Figure 2.11 (a) ) because the mass transfer is fast enough, and for Lewis number above unity, there is super-saturation near the wall ( as Figure 2.11 (b) ).

Quantitatively, the radial gradients at the wall are related as

$$\frac{\left(\frac{\partial c}{\partial r}\right)_w}{\left(\frac{\partial c_s}{\partial r}\right)_w} = Le \quad (2.65)$$

Eqn. (2.65) is proven as following. Assuming semi-fully developed for concentration distribution, which is similar with fully developed temperature profile,

$$\left(\frac{\partial c}{\partial r}\right)_w \approx -\frac{1}{4} \frac{u_m d}{D} \left(-\frac{dc_w}{dx}\right) \quad (2.66)$$

The sublimation concentration is given as

$$\left(\frac{\partial c_s}{\partial r}\right)_w = \left(\frac{\partial T}{\partial r}\right)_w \left(\frac{1}{RT} \frac{dP_s}{dT} - \frac{P_s}{RT^2}\right) \quad (2.67)$$

where

$$\left(\frac{\partial T}{\partial r}\right)_w = -\frac{u_m d}{\alpha} \left(-\frac{dT_w}{dx}\right) \quad (2.68)$$

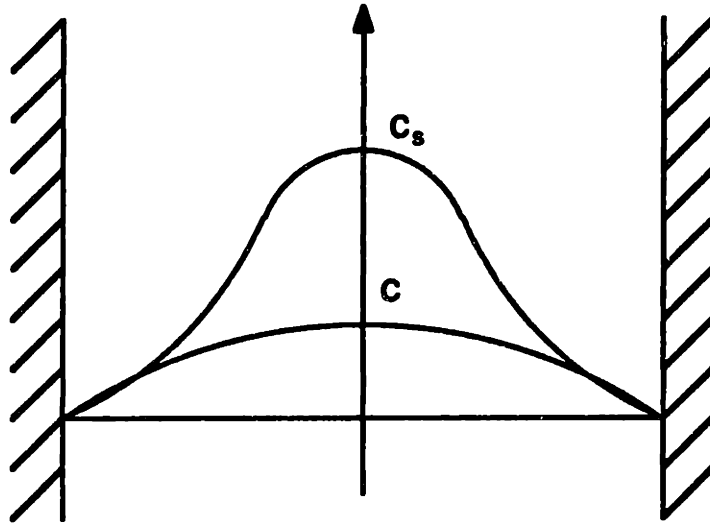
Combining Eqns. (2.67) and (2.68) yields

$$\left(\frac{\partial c_s}{\partial r}\right)_w = -\frac{1}{4} \frac{u_m d}{\alpha} \left(-\frac{dc_w}{dx}\right) \quad (2.69)$$

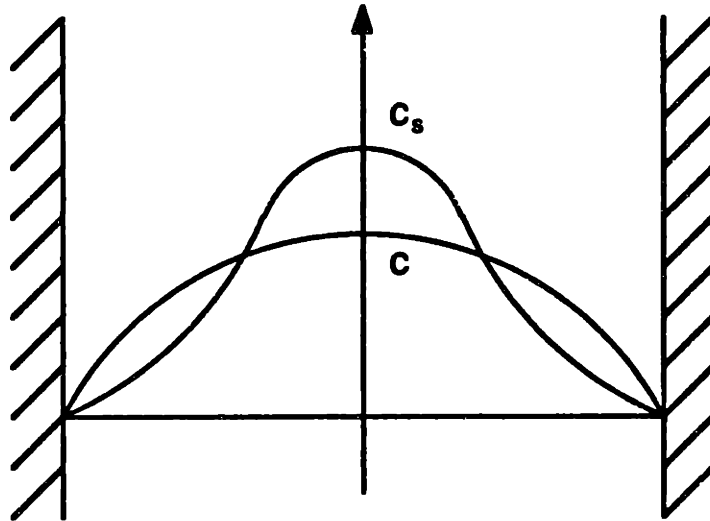
and from Eqns. (2.66) and (2.69), Eqn. (2.65) is derived.

As listed in Table 2.1, where the thermal diffusivity of the mixture is that of helium according to Assumption 2, the Lewis numbers of common contaminants in helium are about 2.5 to 3.0 at standard conditions. This means from Eqn. (2.65) that the slope of concentration is about 2.5 to 3 times greater than that of sublimation concentration. Since Lewis number is nearly independent of temperature and total pressure, it may be concluded that there is always supersaturation in cryogenic contamination for every contaminant.





(a) Small  $Le$  : No Super-Saturation



(b) Large  $Le$  : Super-Saturation

Figure 2.11 Lewis Number and Super-Saturation

**Table 2.1 Lewis Numbers of Common Contaminants in Helium**

Contaminant	$\alpha$ (m <sup>2</sup> /sec)	D (m <sup>2</sup> /sec)	Le = $\alpha / D$
N <sub>2</sub>	1.83 x 10 <sup>-4</sup>	6.87 x 10 <sup>-5</sup>	2.66
O <sub>2</sub>		7.29 x 10 <sup>-5</sup>	2.51
Ar		7.34 x 10 <sup>-5</sup>	2.49
CO <sub>2</sub>		6.12 x 10 <sup>-5</sup>	2.99

## 2.4.2 Degree of Super-Saturation and Snow Formation

This section intends to estimate the maximum degree of super-saturation and its location in order to predict and explain the onset of snow formation and its effect on wall accumulation. To reach this goal, it is essential to examine the super-saturation at the entry region, because the maximum degree is located there. In this sub-section, the degree of super-saturation is estimated in terms of  $(P-P_s)$  instead of  $(c-c_s)$ .

As a first step, the maximum super-saturation for a given  $x$  is defined as

$$\Delta P(x) = \text{Max}_r \{ P(x,r) - P_s(x,r) \} \quad (2.70)$$

A qualitative description for the variation of  $\Delta P$  along  $x$  is presented as follows. At the Point 0 in Figure 2.12, which is the sublimation starting point,  $\Delta P$  is zero because the partial pressure is uniform and smaller than or equal to the sublimation pressure over the cross-section. Immediately after the sublimation starts on the wall, super-saturation occurs because the mass transfer boundary layer grows from the wall at a slow rate (Point 1). In that situation, the partial pressure of contaminant remains constant except inside of the boundary layer, while the sublimation pressure is fully developed because the temperature is fully developed. As the boundary layer grows further,  $\Delta P$  increases throughout the entry length (about Points 2 or 3). After the flow is semi-fully developed, the relative shape of partial pressure compared with the sublimation pressure remains same, but their absolute magnitude gets smaller because the sublimation pressure gets flatter as temperature decreases in the vapor-

pressure curve. Therefore  $\Delta P$  decreases as  $x$  increases after the entrance region. The final distribution of  $\Delta P(x)$  is roughly shown in Figure 2.13.

The maximum degree of super-saturation,

$$\Delta P_{\max} = \text{Max}_x \{ \Delta P(x) \} \quad (2.71)$$

can be exactly obtained because all necessary information for temperature and concentration has been found. But the information is expressed in a non-closed and complicated form, for which an analytical solution for  $\Delta P_{\max}$  is not easily obtainable even if calculation of a single problem is numerically possible. Furthermore, in order to be useful, the expression for the maximum degree of super-saturation should be in a simple form with dimensionless number groups which include the effect of the prescribed flow conditions and geometry, since the onset of snow formation may be a sort of stability problem similar to the onset of turbulence in fluid mechanics.

For these reasons, the maximum degree of super-saturation is "estimated" through a linearization technique, instead of getting the complicated exact expression. From Figure 2.13, the maximum value of  $\Delta P$  is approximately expressed as

$$\Delta P_{\max} \approx L_0 \left\{ \frac{d}{dx} \Delta P(x) \right\}_0 \quad (2.72)$$

where  $L_0$  is the mass transfer entry length. As mentioned in the previous qualitative description, the degree of super-saturation reaches its maximum at

around the point where the concentration boundary layer grows to meet each other, which is estimated to occur about  $x = L_0$ .

To obtain the desired expression from Eqn. (2.72), the derivative of  $\Delta P(x)$  at  $x=0$  should be evaluated. For convenience, Eqns. (2.10) and (2.34) are simply noted as

$$T(x,r) = T_w(x) + T_r(r) \quad (2.73)$$

and

$$c(x,r) = c_w(x) + c_r(x,r) \quad (2.74)$$

respectively. Of course, in these equations  $T_r \ll T_w$  and  $c_r \ll c_w$ . The partial pressure of contaminant is obtained as

$$P(x,r) = c(x,r) R T(x,r) = c_w(x) R T_w(x) + c_r(x,r) R T_w(x) + c_w(x) R T_r(r) \quad (2.75)$$

where the higher order terms are neglected. And the sublimation pressure corresponding to the temperature is obtained as

$$P_s(x,r) = P_s\{T(x,r)\} = P_s\{T_w(x)\} + \left(\frac{dP_s}{dT}\right)_{T_w} T_r(r) \quad (2.76)$$

where the higher order terms are neglected, too. From Eqns. (2.75) and (2.76),

$$P(x,r) - P_s(x,r) = c_r(x,r) R T_w(x) - \left(\frac{dc_s}{dT}\right)_{T_w} R T_w(x) T_r(r) \quad (2.77)$$

where the first term of the right hand side in Eqn. (2.75) has been cancelled with that in Eqn. (2.76), and the third term of right hand side in Eqn. (2.75) and the

second term of right hand side of Eqn. (2.76) were combined into the second term of right hand side in Eqn. (2.77).

Now taking a partial derivative of Eqn. (2.77) with respect to  $x$  at  $x=0$  yields

$$\frac{\partial (P - P_s)_{x=0}}{\partial x} = \left(\frac{\partial c_r}{\partial x}\right)_0 RT_w(0) - \frac{d}{dx} \left\{ \left(\frac{dc_s}{dT}\right)_{T_w} \right\}_0 RT_w(0) T_r(r) - \left(\frac{dc_s}{dT}\right)_{T_w(0)} R \left(\frac{dT_w}{dx}\right)_0 T_r(r) \quad (2.78)$$

The first term of Eqn. (2.78) can be found from Eqn. (2.34).

$$\left(\frac{\partial c_r}{\partial x}\right)_0 RT_w(0) = \left(-\frac{dc_s}{dx}\right)_0 RT_w(0), \text{ for } 0 \leq r < r_0 \quad (2.79)$$

From the above qualitative description, it is obvious that near  $x=0$  maximum super-saturation occurs at  $r \approx r_0$  or close to the wall, since the partial pressure is uniform over the radius but the sublimation pressure increases as  $r$  decreases.

Therefore,

$$\left(\frac{d}{dx} \Delta P\right)_0 = \left\{ \frac{\partial (P - P_s)_{x=0}}{\partial x} \right\}_{r=r_0} \quad (2.80)$$

or

$$\left(\frac{d}{dx} \Delta P\right)_0 = RT_w(0) \left(-\frac{dc_s}{dx}\right)_0, \quad (2.81)$$

where  $T_r(r=r_0) \approx 0$  has been used. Even if Eqn. (2.81) has been obtained after a lengthy analytical procedure, it has a very simple and clear physical meaning that the increasing rate of super-saturation with  $x$  at  $x=0$  is proportional to the

decreasing rate of sublimation concentration at the wall, because the concentration of contaminant remains essentially uniform at the boundary layer starting region.

Going back to Eqn. (2.72) with Eqns. (2.61) and (2.81), the expression for the maximum degree of super-saturation is obtained in terms of pressure units as

$$\Delta P_{\max} = 0.0332 R T_w(0) \left( \frac{dc_s}{dT} \right)_0 \left( -\frac{dT_w}{dx} \right)_0 (Re Sc) d \quad (2.82)$$

where the x-derivative of sublimation concentration has been divided into its temperature dependence and the temperature gradient. Since

$$\frac{dc_s}{dT} = \frac{1}{RT} \left( \frac{dP_s}{dT} - \frac{P_s}{T} \right) \quad (2.83)$$

and for most of contaminants,  $(dP_s/dT) \gg (P_s/T)$  (see Appendix A, for Carbon Dioxide), Eqn. (2.82) is simplified to the final expression for the maximum degree of super-saturation in terms of pressure units as

$$\Delta P_{\max} = 0.0332 \left( \frac{dP_s}{dT} \right)_0 \left( -\frac{dT_w}{dx} \right)_0 (Re Sc) d \quad (2.84)$$

In words, the degree of super-saturation is proportional to the slope of vapor-pressure curve and temperature gradient at the sublimation point, Reynolds number, Schmidt number and the tube diameter. It is noticed that the inlet partial pressure of contaminant affects the slope of vapor-pressure curve at  $x=0$ . It should be mentioned that Eqn. (2.84) is valid only for the problem with a

gradual temperature change, because it has been derived through a linearization of sublimation relations.

One more useful step to develop an analytical model concerning the possibility of snow formation is a derivation of dimensionless expression for the degree of super-saturation. Because this step might help to generalize the results verified with somewhat restrictive experiment (for example, only low Reynolds number flow with carbon dioxide as a contaminant, as described in next chapters) to different situation. To derive that expression, the obtained degree of super-saturation needs to be observed from different angle. As shown in Figure 2.14, what has been found in Eqn. (2.84) is the difference of partial pressure of contaminant and the sublimation pressure at that temperature. Another important amount for the degree of super-saturation is in temperature unit,  $\Delta T$ , which is the difference of temperature and the sublimation temperature at the partial pressure of contaminant. One of the reasons why the  $\Delta T$  is introduced here is that it can be used in an intuitive definition of the dimensionless degree of super-saturation (denoted by DSS) as

$$DSS = \frac{C_p \Delta T_{max}}{H_{ig}}, \quad (2.85)$$

where  $H_{ig}$  is the latent heat of sublimation and  $C_p$  is the specific heat of contaminant in gas phase at constant pressure.

The DSS indicates how much the contaminant has gone over the sublimation point without a phase change, compared with the latent heat. This dimensionless number can be associated with the possibility of snow formation,



as the latent heat implicates the amount of driving potential in order for the contaminant molecules to get together and begin nucleation. Of course, the nucleation for the snow is not an easy process to generally identify, even if it is broadly classified as homogeneous and heterogeneous nucleation depending on the existence or quantity (or sometimes the size) of the actively condensable particles. In any case, it is true that the possibility of nucleation of contaminant and its growth is closely related with the degree of super-saturation and the latent heat. Details of the mechanism for snow formation and its moving behavior <sup>14, 15</sup> are outside of the scope of this thesis. Instead, through a typical dimensional analysis using this moderately reasonable dimensionless number and the experimental results concerning snow formation, it is intended to estimate how significant the snow formation is in practical helium systems.

To finish the derivation of DSS, Eqn. (2.84) is converted to the temperature unit of degree of super-saturation and substituted into Eqn. (2.85), giving the desired expression as

$$DSS = 0.0332 \left( \frac{C_p d}{H_v} \right)_0 \left( -\frac{dT_w}{dx} \right)_0 (Re Sc) \quad (2.86)$$

At low temperatures, the specific heat is not dependent on temperature, and its constant value is the gas constant, multiplied by a constant determined by the configuration of atoms in molecules. For carbon dioxide,  $C_p = (7/2) R$ , or

$$DSS = 0.116 \left\{ \frac{R d}{(H_v)_0} \left( -\frac{dT_w}{dx} \right)_0 \right\} (Re Sc) \quad (2.87)$$

There are two dimensionless groups in addition to a constant in Eqn. (2.87). The first group in brace can be said a dimensionless temperature gradient at the contaminant accumulation point and the second is, as mentioned earlier, the flow rate to mass transfer ratio. The constant is of little significance except for the order of magnitude, because there have been several approximations.

It is finally observed how the four input parameters, given in the previous chapter, affect the dimensionless degree of super-saturation. The tube diameter has an effect of power two, one of which is in the dimensionless temperature, the other is in Reynolds number. The flow mean velocity shows up only in Reynolds number. Combining these two parameters, DSS is proportional to the flow rate. The axial temperature gradient in the sublimation starting range affects it linearly when the gradient changes gradually. The fourth parameter is the inlet partial pressure, which is of special interest. Even if it does not appear explicitly, it determines the sublimation starting temperature and therefore the latent heat of sublimation. As shown in Figure A.3, there is an interesting behavior of the latent heat for various temperatures for carbon dioxide. Because with a typical contamination level, CO<sub>2</sub> has its sublimation starting temperature from 125 to 130 K, where the latent heat is near constant. This means that the partial pressure of carbon dioxide would not affect the onset of its snow formation. However, it should be emphasized that it does not mean that the partial pressure is unimportant for the amount of wall accumulation, since the expression for DSS is concerned only with the onset condition of snow formation.

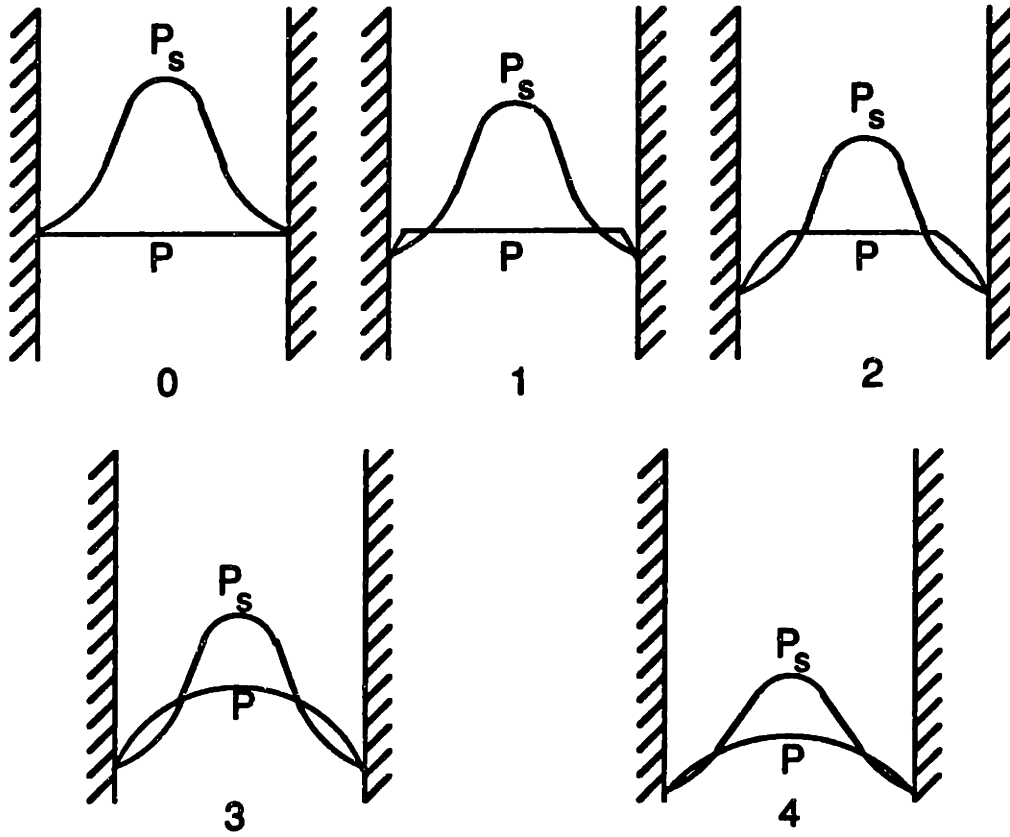


Figure 2.12 Super-Saturation at the Entry Region

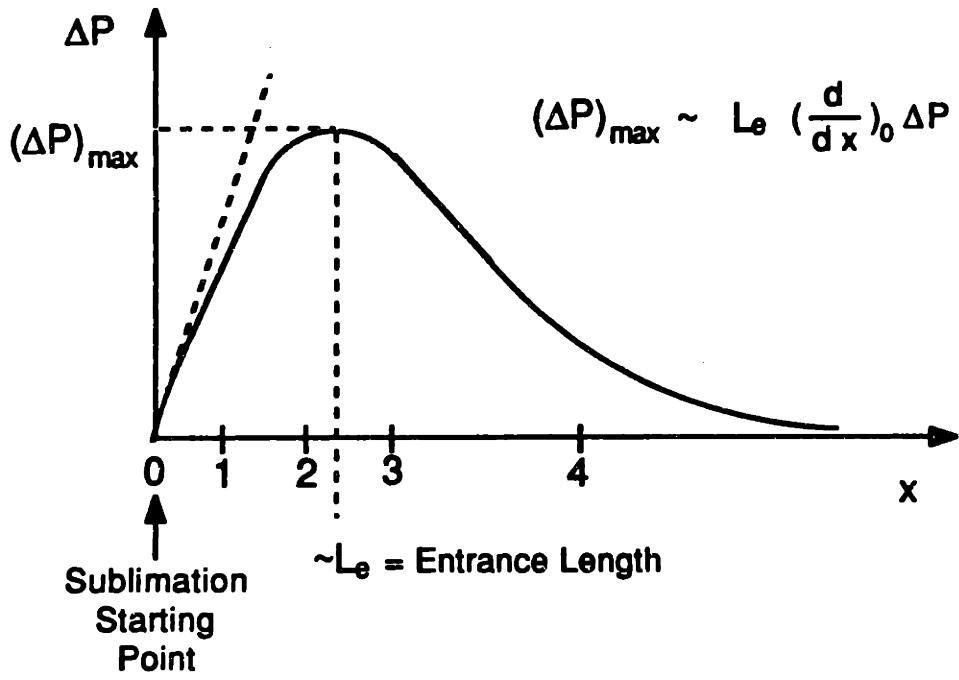


Figure 2.13 Distribution of  $\Delta P$  along  $x$

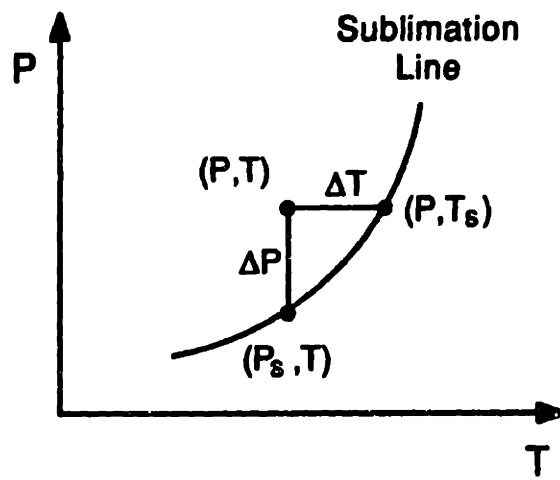


Figure 2.14 Degree of Super-Saturations in the Pressure and Temperature Units

## Chapter 3

### Experimental Apparatus and Procedure

The analytical prediction of contaminant behavior presented in the previous chapter is verified and evaluated by a specially designed experiment to be described in this chapter. Basically, the experiment detects the spatial distribution of wall accumulation of a contaminant for some known conditions. A particular interest of this experiment is in the onset conditions of snow formation, the relative amount of formed snow and its behavior. Any snow formation is expected to result in an abrupt change or an additional peak in the spatial distribution of wall accumulation without snow formation.

The overall configuration, important design aspects of the apparatus and the procedure of the experiment are presented in this chapter. Also, some of the desired test conditions obtained after the construction of the apparatus are given during the presentation as appropriate. Most of the critical results and discussions of this experiment are presented in the next chapter.

As introduced in Chapter 1 with Figure 1.4, the basic idea to detect the spatial distribution of wall accumulation is that, a sharp temperature wave propagating continuously from the cold to the warm end (opposite to the flow direction) flushes accumulated contaminant through the column and a detector (measuring the concentration of contaminant) monitors the migrating contaminant at the exit of the column as a function of time. Time history of the detector output reflects the spatial distribution of wall accumulation if the heating

is locally intensive and the dispersion of the concentration wave is not too much.

The detection method of this experiment is, more or less, comparable with that of gas chromatography (GC), a major instrumental technique in analytical chemistry and in many other areas. Both methods measure the migrating concentration wave of minor gases as a function of time and require minimum dispersion of the wave for the best performance, even if the main concern of this experiment is the detailed shape and magnitude of a specific peak in the detector output, while that of GC is the magnitude and sequence of several peaks. Documented instrumentation skills of gas chromatography<sup>16-20</sup> were most helpful in designing this experiment.

### **3.1 Overall Configuration of Experiment**

This section describes the overall configuration of the experiment for the purpose of quick and general understanding, before the detailed design of the apparatus and its assembly are presented in next sections.

Figure 3.1 is a schematic diagram of the apparatus including the flow circuit of the fluids. The test gas was selected to be a very low concentration (100 ppm as specified by the supplier) of carbon dioxide in helium for the following three reasons. First of all, the contamination behavior of carbon dioxide can be observed at above the liquid nitrogen temperature. Secondly, the precise thermodynamic properties for sublimation are available. Finally CO<sub>2</sub>

has a thermal conductivity much smaller than that of helium, so CO<sub>2</sub> has a high sensitivity with the selected detector, as described later.

The test gas, controlled by a two-stage pressure regulator, flows into a straight and vertical test column located at the center of the vacuum chamber. The top of the column is the warm end side. The outflowing gas from the test column is connected to the sensing side of the thermal conductivity detector after a heat exchange with a reference gas which has much lower and steady concentration of carbon dioxide. The test gas, whose concentration has been detected, flows back to the outer tube of the test column from the bottom-cold-end side to make the balanced counterflow of a heat exchanger.

The temperature of the test column is controlled by two electrical heaters placed in and outside of the outer annulus of the heat exchanger. The annular space is filled with liquid propane, cooled by liquid nitrogen. Propane is used because it remains liquid phase from liquid nitrogen temperature to room temperature at a moderate pressure. The outside heater (not explicitly shown in Figure 2.1) is used to generate a uniform heat flux over the entire test column when a linear temperature gradient is set up. The small inside heater (shown as a black piece near the bottom of test column) is a moving heater whose position is precisely controlled by a motor at the top and a wire. This heater is used to provide intensive local heating when the test column is heated and the wall-accumulated contaminant starts to migrate.

The 3-way valve I and the shut-off valves 1,2 and 3 are necessary to warm up and calibrate the gas analyzer. The 3-way valves II and IV are to



change the path of the test gas and propane as necessary, respectively. The 3-way valve III is installed for the purpose of purging air to eliminate any pre-contamination of the apparatus in the preparing phase of experiment. The shut-off valve 4 is used only when a fast drain of liquid propane is needed and the shut-off valve 5 is used to increase the pressure of nitrogen in the rare case that the propane is frozen.

The flow rates of the test gas and the reference pure helium gas are controlled by the metering valves in the flowmeters of the gas analyzer unit. The pressure of propane is controlled by both the regulator at the cylinder and the back pressure regulator at the exit.

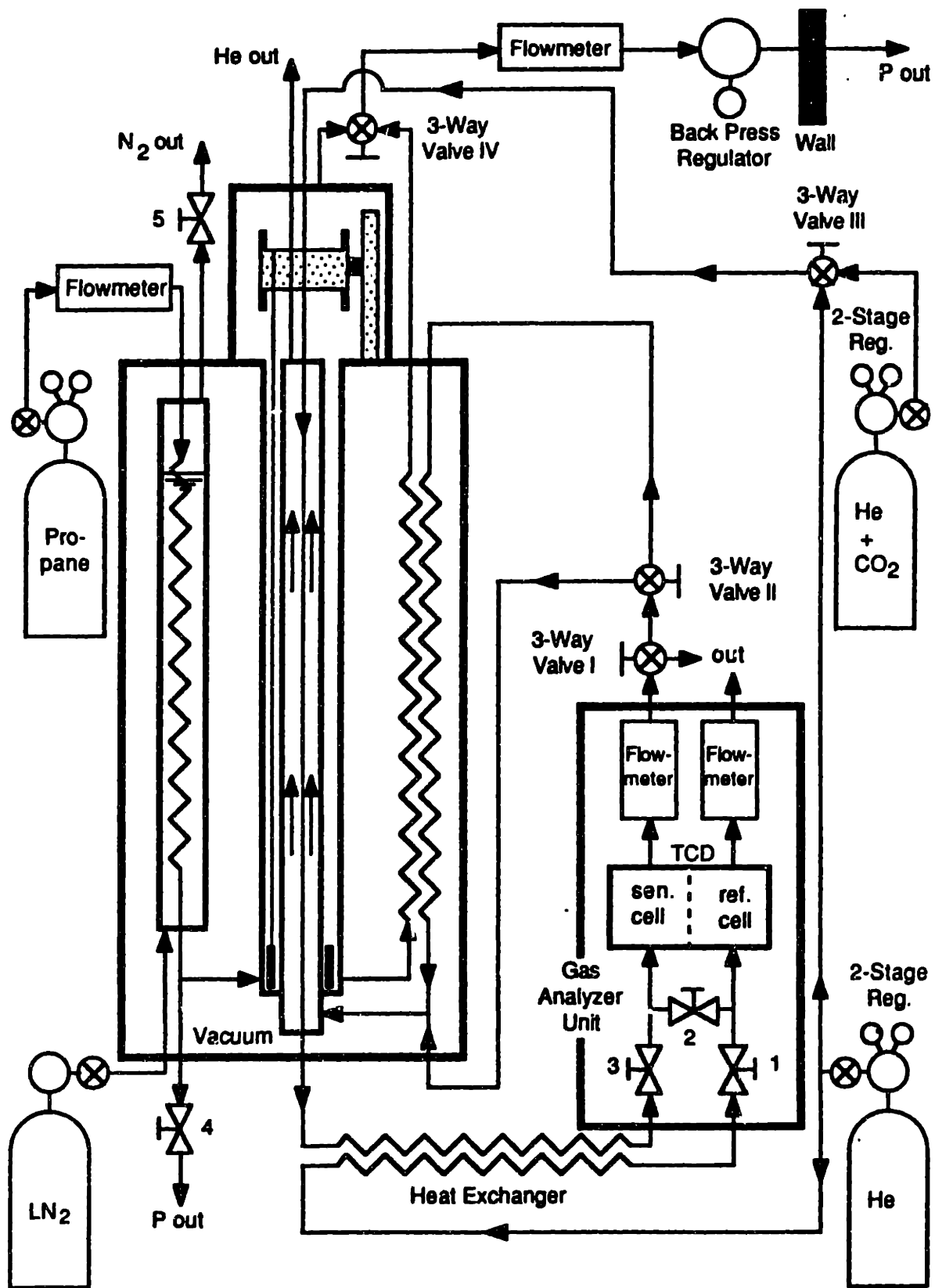


Figure 3.1 Schematic Diagram for the Overall Configuration of Experiment

## **3.2 Design of Apparatus**

**This section discusses the design aspects of a few important parts of the experimental apparatus. The two critical factors in designing the apparatus are to provide a stable and controllable condition for the accumulation of contaminant and to detect the spatial distribution with minimum loss of information.**

### **3.2.1 Test column**

**The test column is a round tube where the contamination occurs. In selecting the dimensions of the column, consideration of three phenomena should be included. The first one is a heat transfer characteristic. A fast radial heat transfer rate is required when the column is heated. A large ratio of length to diameter is necessary. Second, the test column diameter should be selected such that the degree of super-saturation is small enough to observe the onset of snow formation with a variation of axial temperature gradient and flow rate in reasonable ranges. Finally, dispersion of the migrating concentration wave in the column and through to the detector should be minimum. The test flow rate is the same as the flow rate with which the contaminant is carried to the detector. As shown in Appendix D, the minimum dispersion can be obtained by selecting a proper diameter of the tube and flow rate.**

**The test column was selected as a long and precleaned stainless-steel capillary tubing (provided for open tubular GC column) with dimensions of**

**inside diameter = 1.0 mm**

**wall thickness = 0.3 mm**

**length = 2 m.**

The test column tubing was made straight by stretching by about 1% of the total length. The test column was placed inside of a slightly bigger stainless steel tube (outside diameter = 3.9 mm, wall thickness = 0.5 mm) so that they formed a balanced counterflow heat exchanger with very high effectiveness of about 99.80 to 99.95 % for the flow rates mentioned later. The high and low temperatures of the heat exchanger were about 270 K and 110 K, respectively; therefore, the average axial temperature gradient was about 80 K/m.

### **3.2.2 Detector**

Four important characteristics of common detectors are examined for their applicability to this specific experiment: minimum detectable amount, linearity, response time, and detectable species. Out of many, the two most frequently used detectors are the thermal conductivity detector (TCD) and the flame ionization detector (FID). As shown in Table 3.1, both satisfy minimum detectable amount and linearity criteria for this application, because the interesting concentration will be about 100 to a few thousand ppm of carbon dioxide in helium. In general, the FID has a shorter response time but cannot detect any carbon dioxide, unless the CO<sub>2</sub> is converted to a detectable species such as methane by some proper chemical reaction processors. When a methanizer is used, the effective response time gets longer. The TCD has a very good response to carbon dioxide because the thermal conductivity of helium is about 10 times of that of CO<sub>2</sub>.

**The detector was selected as a thermal conductivity detector installed in a GC (Gas Chromatography) gas analyzer unit. The cells of the TCD were designed to be very small so that the response time was less than 1 second, which was short enough to avoid too much dispersion in the detector output. The specifications of the selected TCD are listed in Table 3.2.**

**Before a steady operation of the detector, it was critical to purge air from the detector cells and other connected spaces. For an initial start-up, a complete elimination of any pre-contamination was observed after two days of purging. The gas analyzer was calibrated with test gas which has 100 ppm carbon dioxide in helium, as specified by the supplier.**

**In the operation of the detector, the control of flow rate, pressure, and temperature was the most important . To get a stable base line of the detector output, two incoming streams to the reference and sensing cells should be always in exactly the same conditions. The pressures were precisely controlled with two identical two-stage regulators. The temperatures at the inlets were maintained the same with a parallel-flow heat exchanger as shown in Figure 3.1. The metering valves and the flowmeters placed at the exit of the TCD cells controlled the flow rates.**

**A schematic flow diagram of the gas analyzer unit is shown in Figure 3.2. The zero valve is used to purge the air at the preparation step, and the unit is calibrated by switching the zero and span valves. The twin flowmeters are located at the exit in order to reduce the dead volume before the detection. It**

should be mentioned that this gas analyzer unit was originally designed for a typical GC application and much dead volume exists especially around the switching valves. A photograph of the gas analyzer unit is shown in Figure 3.3 together with the data acquisition board and computer system.

**Table 3.1 Characteristics of Thermal Conductivity Detector  
and Flame Ionization Detector**

	<b>TCD</b>	<b>FID</b>
<b>Minimum Detectable Quantity</b>	<b>50 ppm</b>	<b>Less than 1 ppm</b>
<b>Linearity</b>	<b>10<sup>4</sup></b>	<b>10<sup>6</sup></b>
<b>Response Time</b>	<b>Normal</b>	<b>Short</b>
<b>Detectable Species</b>	<b>All except Carrier</b>	<b>Organic Compounds Only</b>
<b>Carrier Gas</b>	<b>He or H<sub>2</sub></b>	<b>He or N<sub>2</sub></b>
<b>Maximum Temperature</b>	<b>400 °C</b>	<b>400 °C</b>

**Table 3.2 Specifications of the Selected Detector  
(GOW-MAC Instrument Co. Model 50-450)**

---

<b>Power Requirements</b>	<b>Nominal 110 Volts AC, 60 Hz 700 Watts</b>
<b>Detector</b>	
<b>Type</b>	<b>Thermal Conductivity</b>
<b>Filament Type</b>	<b>Tungsten (Resistance : 40 <math>\Omega</math>)</b>
<b>Bridge Current</b>	<b>Maximum 200 mA</b>
<b>Carrier Gas</b>	<b>Helium</b>
<b>Flow Rate</b>	<b>10 to 70 cc/min</b>
<b>Operating Temperature</b>	<b>100 °C</b>
<b>Calibrated Range</b>	<b>0 to 1000 ppm (0.1%) CO<sub>2</sub> in He</b>
<b>Recorder</b>	<b>Maximum 1 mV</b>

---



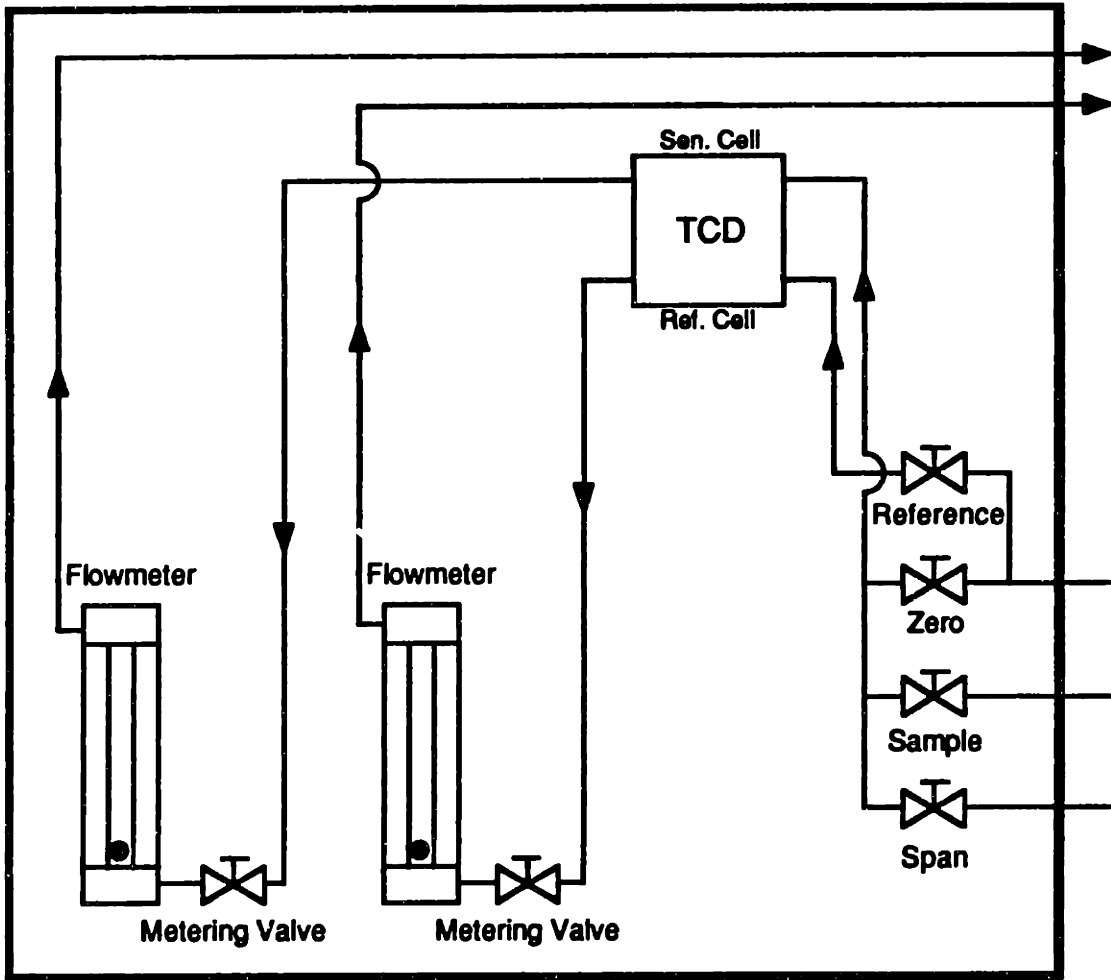
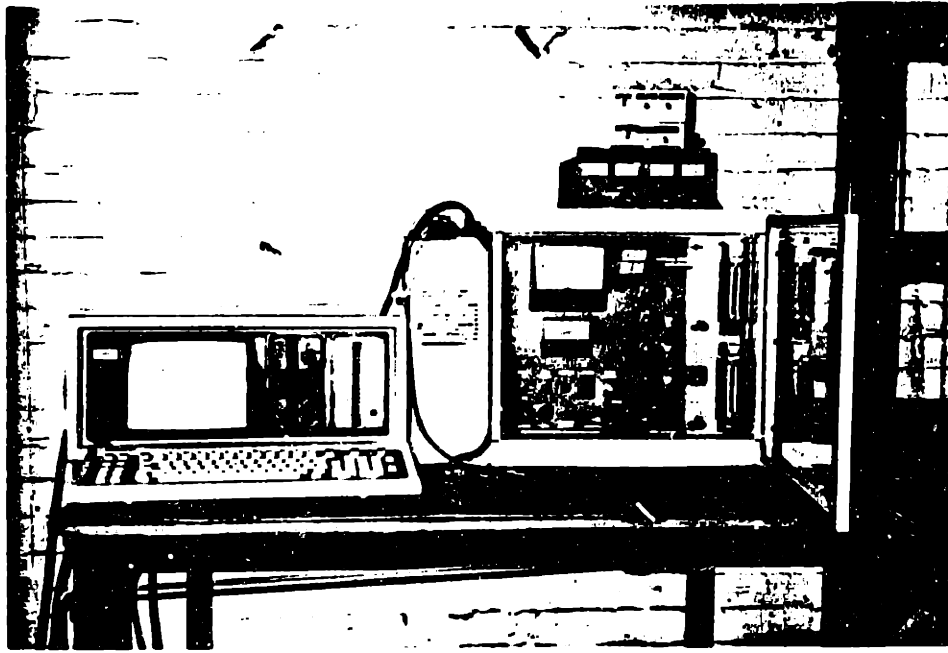


Figure 3.2 Schematic Flow Diagram of Gas Analyzer Unit



**Figure 3.3** Photograph of Gas Analyzer and Data Acquisition System

### 3.2.3 Temperature Control of Test Column

A main effort in designing the apparatus is focused on the temperature control systems of the test column. Three control actions are required to perfect this experiment. According to the time sequence, the first requirement is the linear temperature set-up of the test column without any pre-contamination. Even if a final steady-state temperature distribution of the balanced counterflow heat exchanger is near-linear, it takes an enormously long time because of the high effectiveness (for example, about 20 days for  $\epsilon=99.95$ ) and this long time of temperature set-up cannot avoid a considerable amount of pre-contamination. The second requirement is maintaining a stable temperature distribution during the accumulation period. The third one is the very intensive local (and continuously moving) heating required to establish the sharp temperature wave as shown in Figure 1.4 (b). A simple preliminary calculation shows that the required heat flux to heat the column 50 K (which is about the minimum to guarantee every accumulated contaminant to migrate) with a moving speed fast enough to keep the axial temperature gradient steep at the heating area is far above the burn-out point of a typical low-temperature-application heater with heat transfer through gaseous helium.

Concerning the third requirement, non-touching heating methods such as magnetic induction heating with a high frequency current or a thermal radiation heating were considered. But in both cases, the cooling of the heating source turned out to be extremely difficult because of the requirement that the heating source had to be placed inside of vacuum in order to provide a short heating length.

The above three requirements were satisfied by placing one more outer tube on the heat exchanger and using an auxiliary "liquid" as shown in Figure 3.4. The inner tube is the test column and the middle tube is the counterflow part of the heat exchanger. On the outer surface of the outer tube, a heating (constantan) wire was uniformly wrapped in a spiral shape to supply a uniform heat flux on the tube assembly, which was necessary for the first and second requirements. For the purpose of satisfying the third requirement, a thermfoil heater was attached by epoxy to a short length of tube which was placed, with proper tolerances, between the middle and outer tubes. The auxiliary liquid, selected as a propane, filled the annular space between the middle and outer tubes over the total tube length. Propane was the only fluid whose critical temperature was much above the room temperature and the triple point temperature (which was nearly the freezing temperature at moderate pressure) was as low as the liquid nitrogen temperature. This thermodynamic property was important because a liquid-phase fluid was essential over the temperature range, as described below.

For the first and second requirements, the cold liquid propane flows up from the bottom (cold) end. In addition, the tubes are uniformly heated with a heating wire. A constant mass flow rate with a uniform heat flux sets up the axially linear temperature gradient such that

$$(\dot{m} C_p)_{\text{propane}} \frac{dT}{dx} = \left( \frac{\dot{q}}{l} \right), \quad (3.1)$$

where the right-hand side is the uniform heat flux per unit tube length.

The temporal temperature distribution of the column is shown in Figure 3.5. Liquid propane cooled by liquid nitrogen flows into the column, whose initial temperature is constant and at room temperature. At the same time, the column is uniformly heated by the amount of Eqn. (3.1). In this way, the desired linear temperature distribution is established starting from the cold end. The temperature of the region where the cold temperature wave has not reached remains nearly constant because the pressure of propane is maintained such that the boiling temperature is approximately the room temperature; thus, the phase of propane changes from liquid to vapor.

The time necessary to complete the linear temperature set-up is equal to the column length divided by the temperature wave migration velocity. The velocity is smaller than the flow velocity of propane because the temperature migration is retarded by the heat capacity of three tubes. After writing energy balance equations for the propane and the tubes, the temperatures of them are assumed equal at each axial position because of a small thermal resistance between the tubes. Then, the migration velocity of the temperature wave can be easily obtained as

$$u_{\text{mig}} = \frac{u_{\text{prop}}}{1 + \frac{(\rho C A)_{\text{tube}}}{(\rho C_p A)_{\text{prop}}}}, \quad (3.2)$$

where  $u_{\text{prop}}$  is the mean velocity of liquid propane and  $A$  is the cross-sectional area of the propane flow or the tubes. As can be noticed in Eqn. (3.2), for a fast temperature set-up, a large density of fluid or a liquid is necessary, which is one

of the reasons to use propane as an auxiliary fluid. This temperature set-up process satisfies the first and second requirements simultaneously, because the steady-state temperature distribution of the procedure is linear.

A more difficult part of the column temperature control is to satisfy the third requirement: continuous and intensive local heating. The first quantity to be determined is the moving velocity of the heater. As far as the detection of spatial distribution of wall accumulation is concerned, a slow velocity gives more detailed information. But too slow velocity cannot generate the required steep temperature front because more diffusion time is allowed. A numerical simulation was performed to determine the front temperature gradient for various heater velocities, and one of the acceptable velocities was 1 cm/sec.

The heating rate to increase the temperature of the tubes by 50 K with a velocity of 1cm/sec is about 75 Watts. Since the heating length should be a few centimeters for the heat to be locally intensive, the average heat flux is on the order of  $10^4$  or even  $10^5$  Watts/m<sup>2</sup>. This high heat flux can be transmitted only by a boiling heat transfer, which is the other major reason for the necessity of liquid propane. The nucleate pool boiling relation according to Rohsenow and Choi <sup>39</sup> is given as

$$\frac{C \Delta T}{h_{fg}} = C_{sf} \left\{ \frac{(q/A)}{\mu h_{fg}} \sqrt{\frac{\sigma}{g (\rho_l - \rho_v)}} \right\}^{1/3} Pr^{1.7}, \quad (3.3)$$

where  $\Delta T$  is the difference of the wall and the boiling temperatures,  $C_{sf}$  is a constant which depends on the surface condition and the kind of fluid,  $\sigma$  is the

surface tension of bubble, and  $C$ ,  $\mu$ , and  $Pr$  are the specific heat, viscosity, and Prandtl number of liquid, respectively. For the heat flux of  $10^5$  Watts/m<sup>2</sup>,  $\Delta T$  is about 7 K from Eqn. (3.3). When reviewing the information of so-called burn-out theory and other experimental data <sup>22-24</sup>, this situation is about a burn-out point of typical thermofoil heaters used in many low-temperature applications.

But in this specific boiling heat transfer, the cold tube wall is located very close to the heating surface as shown in Figure 3.4, which results in an immediate condensation of the bubbles because the temperature remains far below the boiling temperature of propane even after the heater is passed over. In other words, the possibility to have the heating surface wet is increased or the heat transfer capability is augmented. Conclusively, the sub-boiling in a propane-filled space makes the desired intensive local heating feasible in this experiment.

The heater position is precisely controlled by a DC stepper motor, a spool and a lead wire. The stepper motor is placed at the top plate as shown in Figure 3.1 and is operated in the vapor propane filled space. The relatively thick and short tube on which the thermofoil heater has been attached, as shown in Figure 3.4, keeps the heater nearly concentric and provides weight when returning to the original bottom position after lifting and heating.

The column-temperature control system is summarized in Table 3.3.

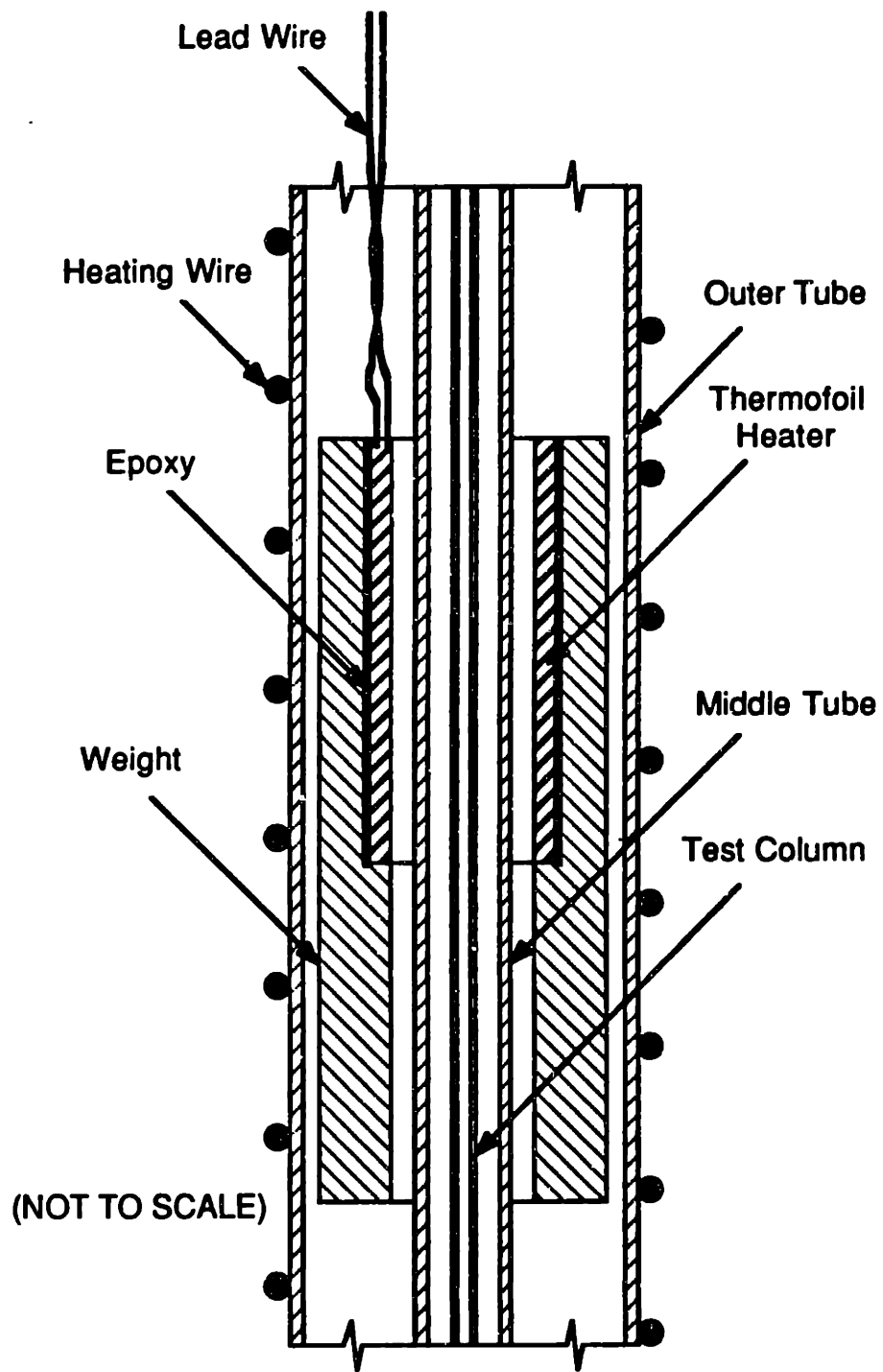


Figure 3.4 Temperature Control System of Test Column



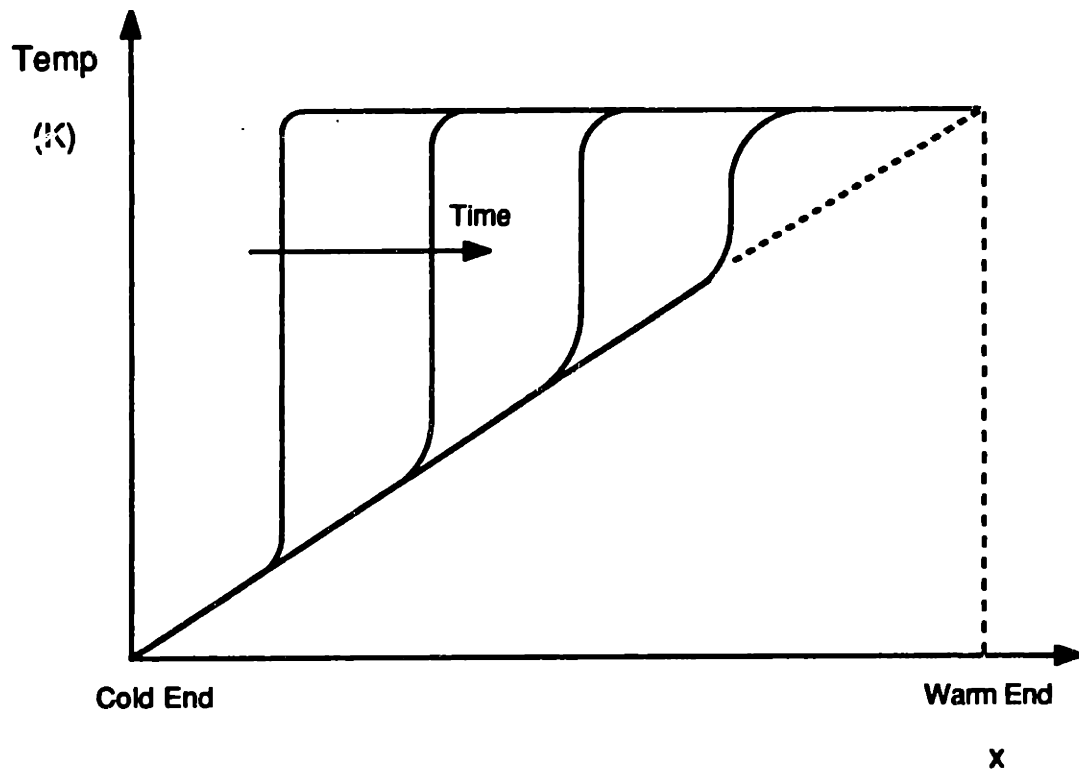


Figure 3.5 Set-up of Linear Temperature of Test Column

**Table 3.3 Elements of Column-Temperature Control System**

---

<b>Heater</b>	<b>Type</b>	<b>Minco Thermofoil Heater with Kapton Insulation</b>
	<b>Dimension</b>	<b>39 mm (length) x 18 mm (width)</b>
	<b>Resistance</b>	<b>26.1 <math>\Omega</math></b>
	<b>Power Output</b>	<b>73 Watts (i = 1.67 Amp, V = 44 Volt AC)</b>
<b>Outer Tube</b>	<b>Dimension</b>	<b>9.5 mm (OD) x 0.7 mm (thickness)</b>
	<b>Material</b>	<b>Stainless Steel</b>
<b>Weight</b>	<b>Dimension</b>	<b>80 mm (length) x 7.3 mm (OD) x 5.0 mm (ID)</b>
	<b>Radial Gaps</b>	<b>0.4 mm to Outer Tube, 0.5 mm to Middle Tube</b>
	<b>Material</b>	<b>Stainless Steel</b>
	<b>Weight</b>	<b>14 g</b>
<b>Motor</b>	<b>Type</b>	<b>Airpax DC Stepper Motor</b>
	<b>Power Supply</b>	<b>12 Volts DC</b>
	<b>Max. Torque</b>	<b>11.3 mNm</b>
	<b>Step Angle</b>	<b>7.5°</b>
	<b>Gear Ratio</b>	<b>20 : 1</b>
	<b>Steps per Rev.</b>	<b>48</b>

---

### **3.2.4 Data Acquisition**

Temperature of the test column is measured and recorded at six locations as shown in Figure 3.6. Point 1 is located 5 cm above the cold end, points 2 to 4 are located every 10 cm from point 1, and points 5 and 6 are located every 60 cm from point 4. These temperature data are used to check the linear temperature distribution at the beginning stage and to evaluate the intensive local heating and the steep front during the detection stage.

One additional location of temperature measurement is the propane tubing at the exit from the nitrogen bath. A temperature of this location below 90 K indicates that the liquid level of nitrogen is too low and that liquid nitrogen should be filled again.

In those temperature measurements, type-J thermocouple (copper-constantan) was used. The thermocouples were soft-soldered on the outside of the outer tube at the necessary locations.

The difference between measured temperature and test column temperature is negligibly small when the linear temperature is set up, because the thermal resistance between the outer tube and liquid propane is small and there is no net heat transfer between the inner tube and liquid propane. But when the intensive local heating is applied, the difference is not negligible. In this heating process, the actual temperature of the test column is lower than the measured temperature, which means that the heating of the test column is slower than that of the outer tube. Since the sub-boiling heat transfer is very

rapid and the balanced heat exchanger has a high effectiveness, the delayed axial temperature gradient of test column is as steep as the measured temperature gradient at the outer tube. Therefore, the migration of accumulated contaminant starts later than the rapid increase of measured temperature and the time lag should be taken into account in the relation of detector output and wall accumulation.

The output of the detector is recorded in units of ppm CO<sub>2</sub>. All the data are collected at every second through an ACRO Data Acquisition and Control System shown in Figure 3.3. The sampling time, 1 second, can be interpreted as a sampling length of 1 cm on the wall accumulation of test column, because the heater moves at the velocity of 1 cm/sec to generate concentration wave to be detected.

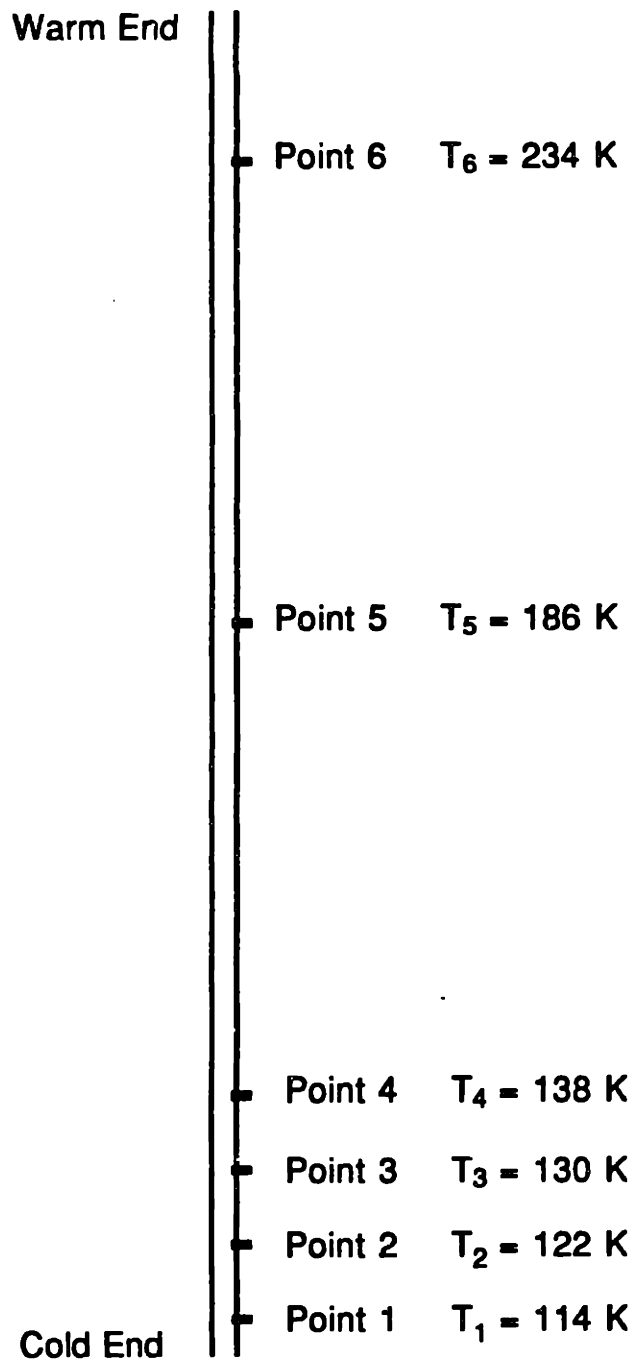


Figure 3.6 Locations of Thermocouples on the Test Column

### **3.3 Assembly of Apparatus**

**In assembling the experimental components, keeping both the vacuum seal and the accessibility to every element was the major concern and the most difficult problem. In particular, to minimize the dead volume between the test column and the detector, the exit of the test column had to be made through the bottom of the vacuum chamber, which increased the difficulty.**

**Another careful assembly process was to maintain the three tubes, including test column, vertically straight and concentric so that the small moving heater could travel smoothly through the outer annular space. To avoid any moving part from the high-pressure propane-filled space to outside, the driving motor had to be placed in the propane-filled space, which complicated the assembly of warm or top end.**

**Detailed assembly diagram for the warm end is shown in Figure 3.7. A heavy top plate (5) was mounted at the top of a structure frame, and supported a vacuum shell (6). At the center of the vacuum space, three concentric tubes (1,2, and 7) were vertically located and the outer tube (7) was welded to the top plate. A small enclosure (3) on the plate was designed to enclose the stepper motor (4) and spool which controlled the position of the small moving heater. Two header pieces of the enclosure (9 and 10) were to align the middle and inner tubes concentric and to assemble and disassemble the elements in the enclosure. Power for the moving heater and the driving stepper was supplied through wires mounted inside of the top plate. A nitrogen vent tube (8) was supported by a bigger auxiliary tube at a distance (called stand-off) because the**

cold part had to be placed at a distance from the rubber O-ring seal for vacuum. Material of every part was 304 stainless steel.

The assembly of cold (and bottom) end is shown in Figure 3.8. Three concentric tubes were brought together with two pieces of copper block (2 and 3). The inner test column, middle tube, and the other helium tube to supply a counterflow were silver-brazed to the lower piece. The outer tube of test column and two propane tubes (not shown in the diagram, perpendicular to the paper) were also silver-brazed to the upper piece in a similar way. The two pieces were soft-soldered to form a cold end block. Two thermofoil heaters (5 and 6) were attached with epoxy on the top and bottom of the block in order to heat the block when the moving heater started to work so that the migrating contaminant was not allowed to condense again at the cold block. Material of every part except the cold block was 304 stainless steel.

The tubes passing through the bottom of vacuum chamber were designed to have the capability for both easy open-up and good vacuum seal. Details of these parts are schematically shown in Figure 3.9. An O-ring seal Cajon fitting was welded to the bottom plate and was allowed to slide over an auxiliary tube when an access to the inside was needed. A bored-through Swagelok union fitting connected the auxiliary tube and the tube passing through the bottom of vacuum chamber.

Every tube except the test capillary column was kept at a distance from the vacuum shell with proper spacers, and was wrapped with a super-insulation to reduce the radiation heat leak when it was cold.

A photograph of the assembled apparatus is shown in Figure 3.10. A long and thin vacuum chamber was held by a 2.6 m-high frame structure. Vacuum was pulled down from the bottom with a mechanical pump and a diffusion pump. A fluid control panel was placed at the eye-height of the frame, and electrical control systems for heaters and a stepper motor were on the gas analyzer unit. A close view to the top of the apparatus is shown in Figure 3.11, and the bottom end of the vacuum chamber is shown in Figure 3.12. The fluid control panel is shown in Figure 3.13.



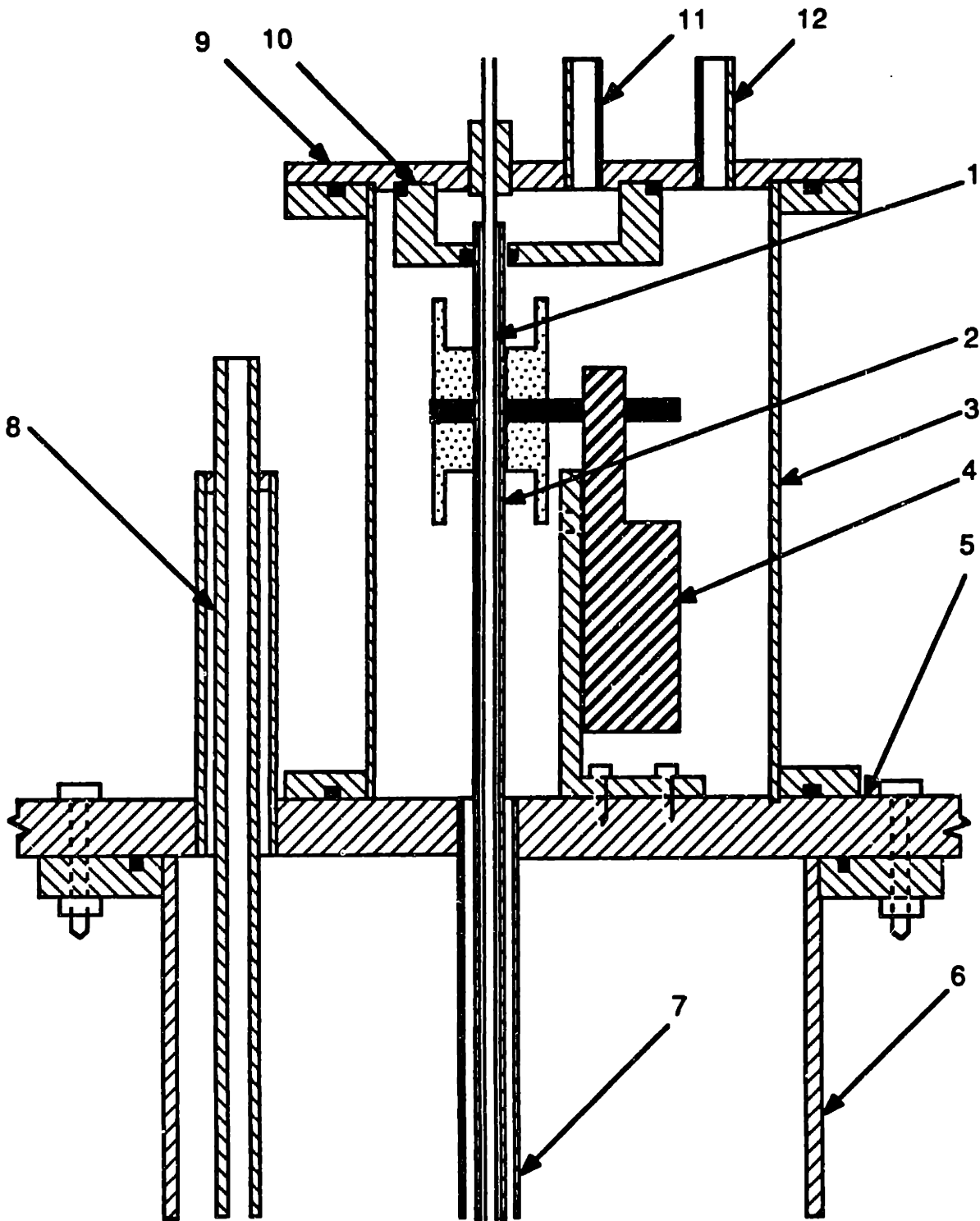


Figure 3.7 Warm End Assembly (SCALE 1:1)

### Legend for Figure 3.7

---

<b>1</b>	<b>Test Column</b>
<b>2</b>	<b>Middle Tube for Counterflow</b>
<b>3</b>	<b>Motor Enclosure</b>
<b>4</b>	<b>Stepper Motor</b>
<b>5</b>	<b>Top Plate</b>
<b>6</b>	<b>Vacuum Shell</b>
<b>7</b>	<b>Outer Tube for Propane Flow</b>
<b>8</b>	<b>Nitrogen Vent Tube</b>
<b>9</b>	<b>Motor Enclosure Heater Plate</b>
<b>10</b>	<b>Middle Tube Aligning Piece</b>
<b>11</b>	<b>Helium Exhaust Tube</b>
<b>12</b>	<b>Propane Exhaust Tube</b>

---

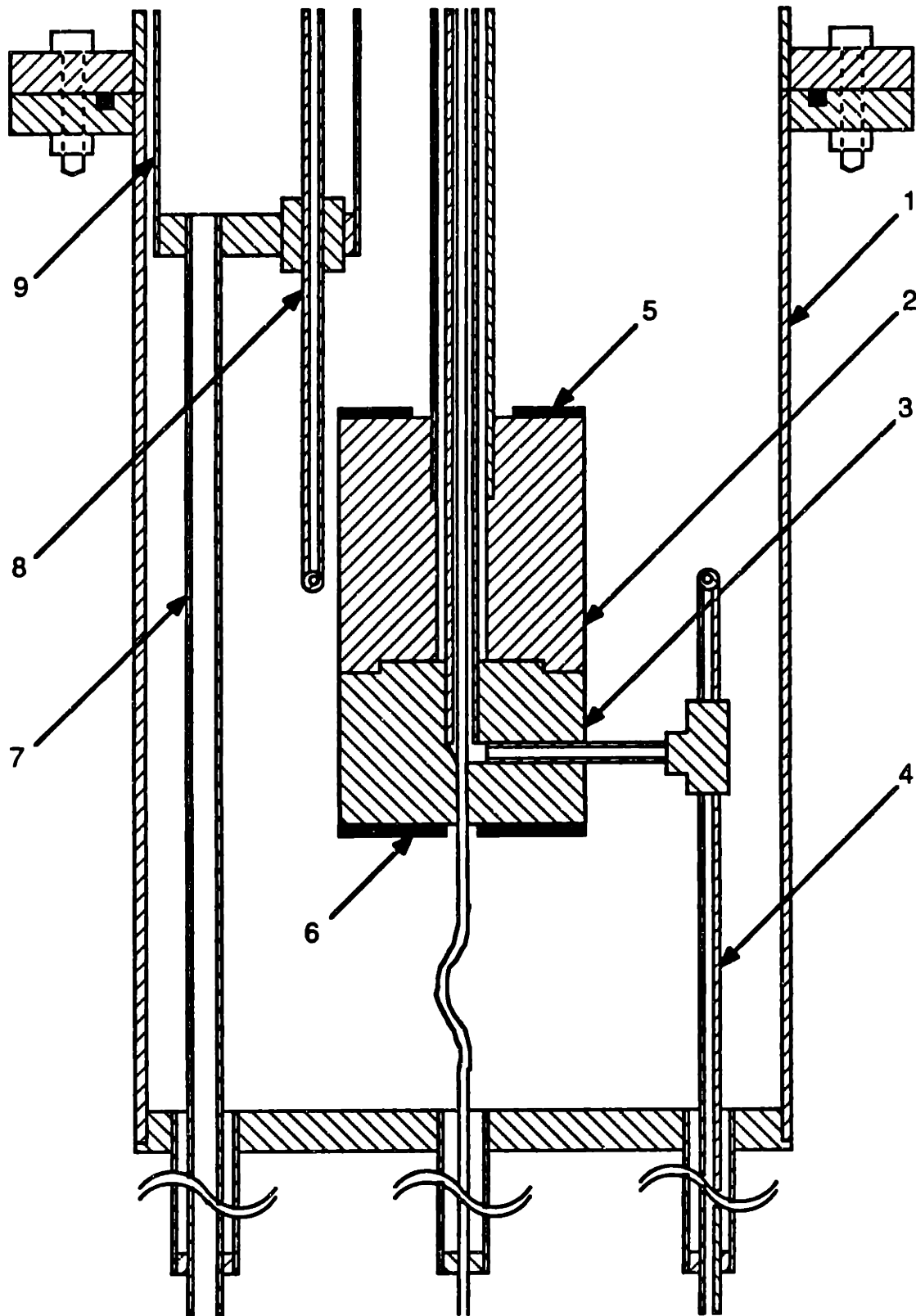


Figure 3.8 Cold End Assembly (SCALE 1:1)

### Legend for Figure 3.8

---

<b>1</b>	<b>Lower Vacuum Shell</b>
<b>2</b>	<b>Upper Piece of Cold Block</b>
<b>3</b>	<b>Lower Piece of Cold Block</b>
<b>4</b>	<b>Helium Tube for Counterflow</b>
<b>5</b>	<b>Thermofoil Heater 1</b>
<b>6</b>	<b>Thermofoil Heater 2</b>
<b>7</b>	<b>Liquid Nitrogen Supply Tube</b>
<b>8</b>	<b>Propane Cooling Tube</b>
<b>9</b>	<b>Nitrogen Bath</b>

---

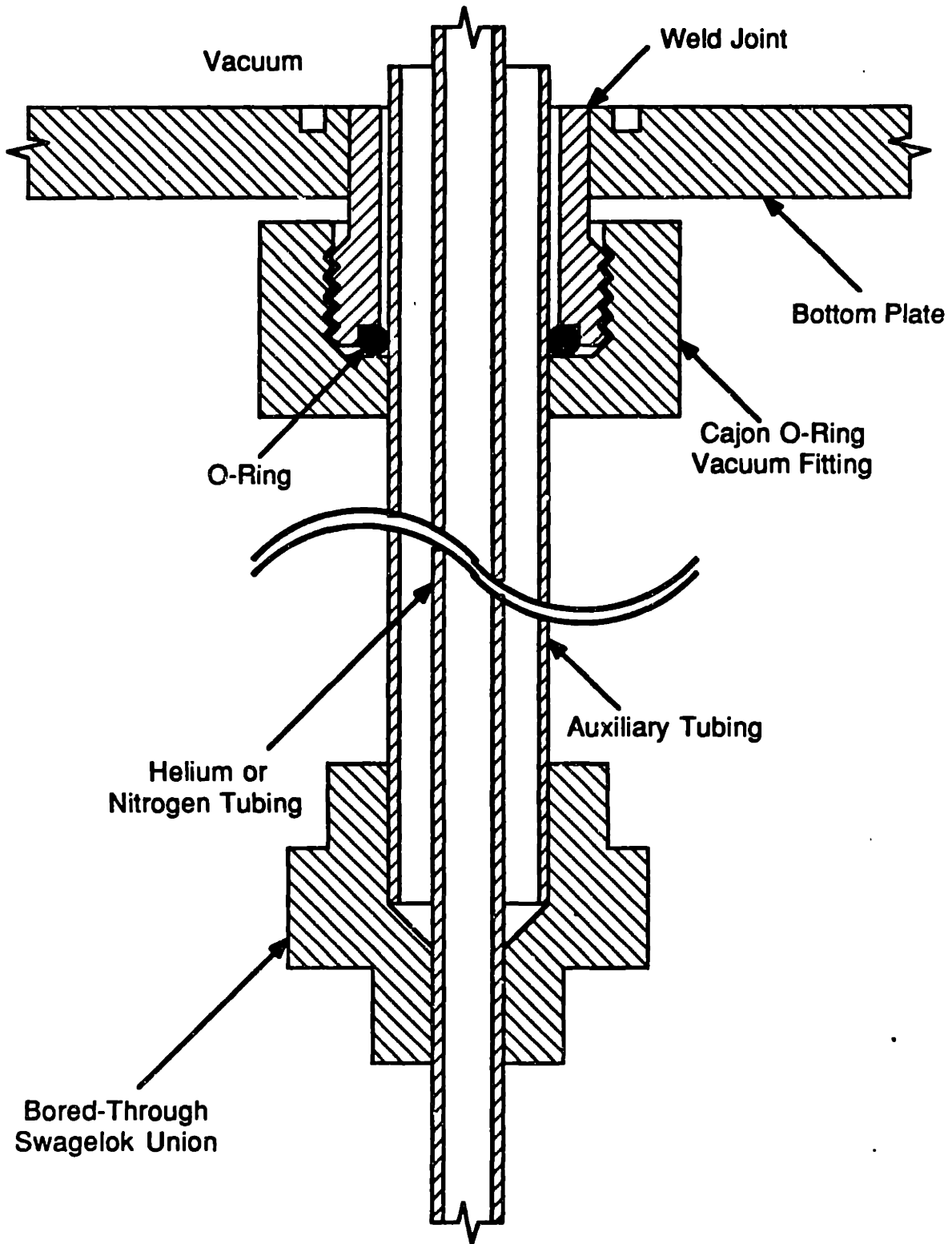
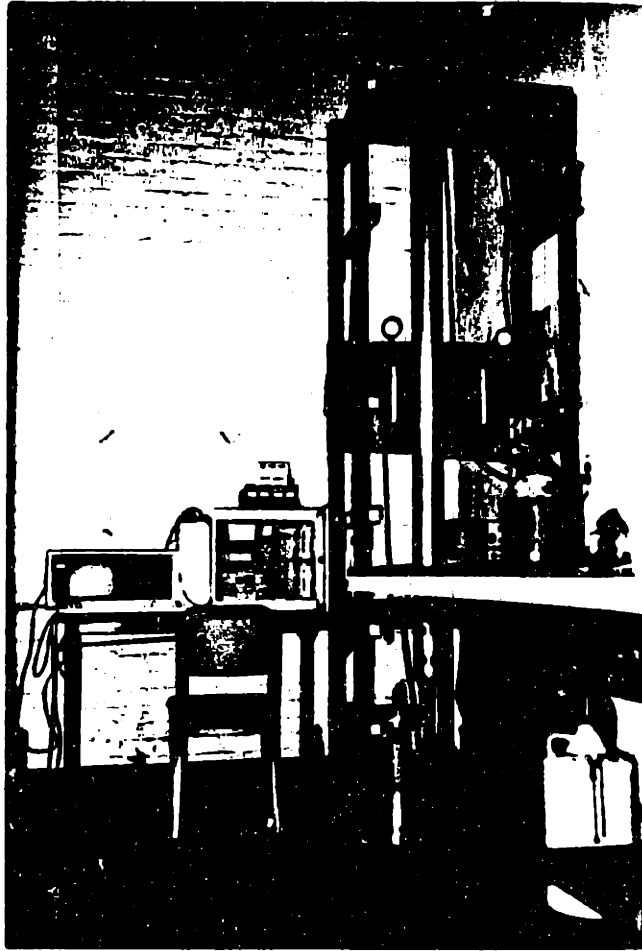


Figure 3.9 Schematic Diagram of a Tube Passing through the Bottom Plate



**Figure 3.10 Photograph of Complete Experiment**

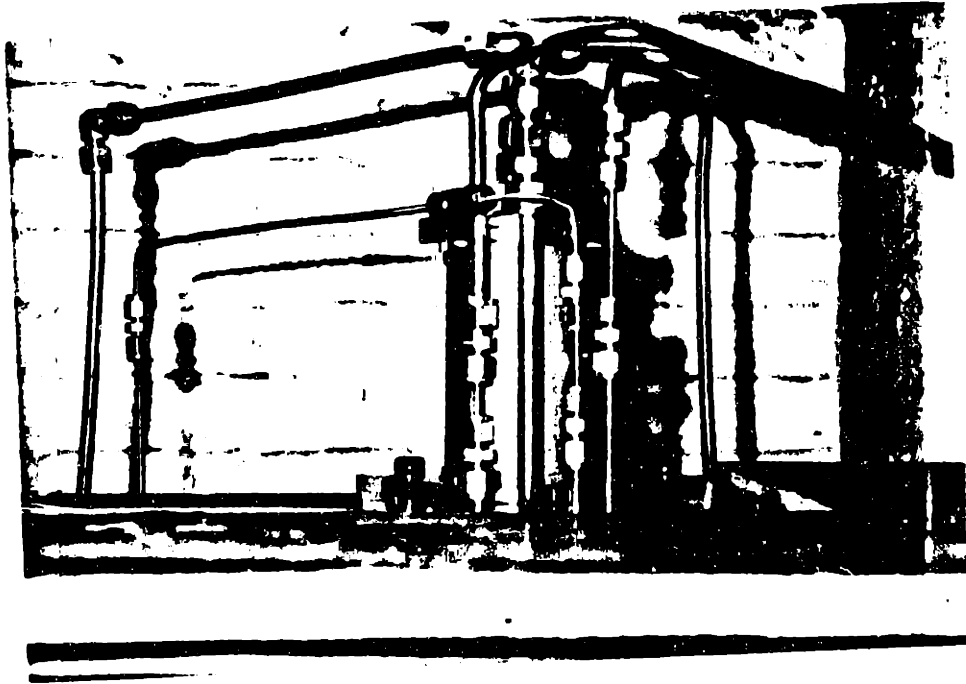
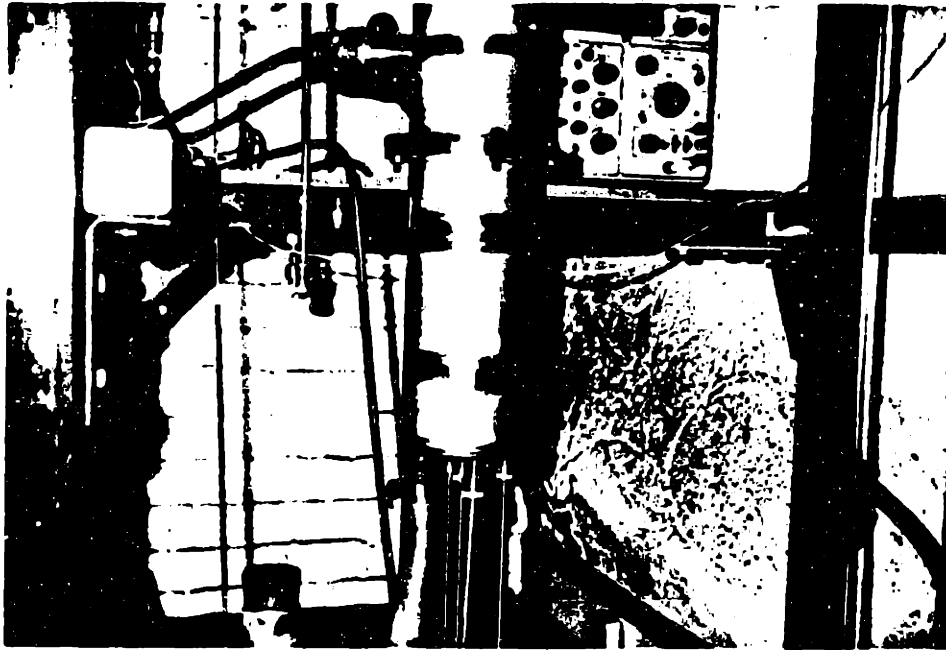
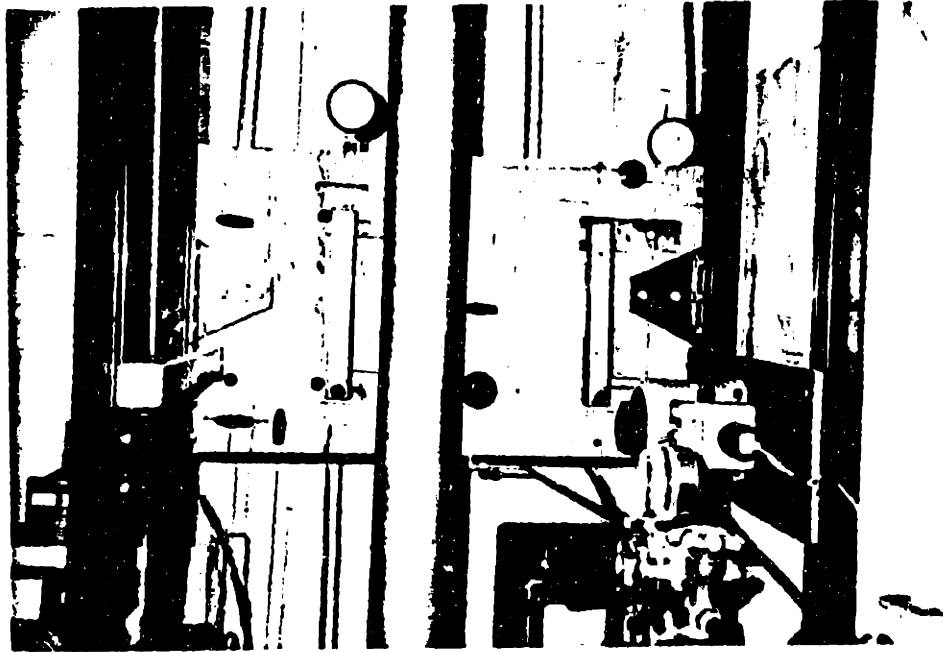


Figure 3.11 Photograph of Top Assembly



**Figure 3.12 Photograph of Bottom Assembly**





**Figure 3.13 Photograph of Fluid Control Panel**

## **3.4 Procedure**

**This experiment consists principally of three phases - the temperature set-up phase, the contamination phase, and the detection phase. The detailed procedures and some of the obtained test conditions are discussed in this section.**

### **3.4.1 Preparation of Experiment**

**Before starting the first phase of the experiment, the vacuum chamber, test column and the gas analyzer should be ready. Vacuum is pulled down to 5 microns with a mechanical pump and a diffusion pump. The reason why this good vacuum is necessary in spite of relatively high temperature of cryogenic experiment is because the cold block and the test column is cooled by the liquid propane whose cooling capacity is not so big. What really matters in preparing vacuum as a thermal insulation is not only the temperature of cold parts but the ratio of heat leak to the cooling capacity.**

**Purging air from the TCD cells in gas analyzer, the test column and other connected tubes is essential to prepare the experiment, as mentioned earlier. This preparation is concerned with two purposes: to eliminate any pre-contamination and to obtain a stable base line of the detector output. The 3-way valve III (in Figure 3.1) is turned down and the shut-off valves 1 and 3 are opened with the valve 2 closed. A complete purge of air was observed in two days after it started.**

A minor calibration of the TCD is needed at every run of experiment. The TCD is very sensitive to the pressure and gas flow rate, which are different from run to run. This calibration is done, after turning the 3-way valve III to the right, with the shut-off valve 1 open and with valves 2 and 3 open and close in turns. When the calibration is completed, valve 2 is opened and valve 3 is closed for the temperature set-up.

### 3.4.2 The Temperature Set-Up Phase

In this phase, the temperature of the test column is linearly set up by a constant liquid propane flow through the outer tube and a uniform heat flux. First, liquid nitrogen is transported into the nitrogen bath as shown in Figure 3.1. The propane is fed into the nitrogen bath from the top, liquefied and cooled down to about 90 K. Since the freezing temperature of propane is 85.7 K and the liquid nitrogen temperature is 77.3 K at atmospheric pressure, the propane is cooled carefully to avoid freezing. One of the methods is to start to feed the propane before the nitrogen bath is full and returns to the atmospheric pressure. The pressure of nitrogen bath can be maintained at around 300 KPa (29 psig), which is high enough for the bath temperature to be above the freezing temperature.

The cold liquid propane fills the heat exchanger shown at the right-hand side of the test column in Figure 3.1, by turning the 3-way valve IV to the right. This heat exchanger is installed to cool the counterflow helium to the cold end temperature for the contamination phase. Once liquid propane shows up at the flowmeter at the top of the figure, the 3-way valve is turned to the left and the

wrapped heating coil (shown in Figure 3.4) is turned on so that the propane flows through the outer tube of the test column and the linear temperature is set up.

The pressure regulator of propane is set to 515 KPa (60 psig) and its flow rate is controlled with a metering valve and flowmeter to 0.614 kg/hr, which yields the mean velocity of about 0.7 cm/sec in the outer annular space. In these propane flow conditions, the heat flux per unit length of tube is 28.9 Watts/m to produce an 80 K/m of temperature gradient according to Eqn. (3.1). The back pressure regulator keeps the pressure around 460 KPa (52 psig) at the exit of the outer tube, where the boiling temperature of propane is about 273 K. It may be noticed that most of the propane is vaporized at the top of the tube and the stepper motor is operated in a vapor-filled enclosure.

A theoretical set-up time is the total length of column divided by the migration velocity of temperature wave given by Eqn. (3.2), which is about 19 minutes because the migration velocity is about a quarter of the fluid velocity. Because of cooling required for the cold block and heat leaks through vacuum, the actual set-up was obtained in 30 minutes.

The obtained temperature distribution for the lower half of the column is shown in Figure 3.14. Some non-linearity was due to the location of the thermocouples, some of which are slightly closer to the heating wire than others. The set-up was satisfactorily obtained as designed.

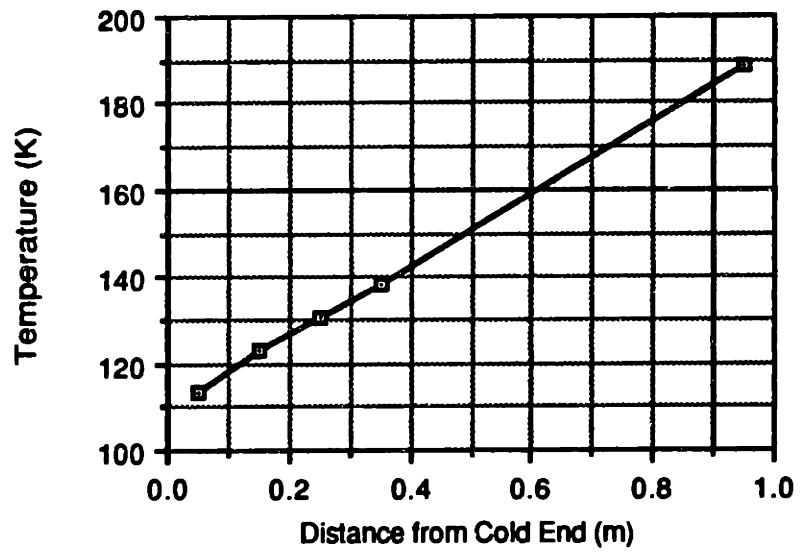


Figure 3.14 Obtained Linear Temperature of Test Column

### **3.4.3 The Contamination Phase**

**After the desired temperature distribution is completely set-up, the test gas is made to flow through the test column by opening the shut-off valve 3 and closing valve 2, while the set-up conditions in the previous phase remains same. For a balanced counterflow, both 3-way valves I and II are turned up.**

**The contamination time does not have to be very long, because the contamination behavior is basically not time-dependent. It should be, however, much bigger than the detection time, during which the contaminant is accumulated in a complicated way. Since the detection time is about 20 seconds, the contamination time is selected as 4 or 5 minutes.**

### **3.4.4 The Detection Phase**

**The first step to detect the spatial distribution of wall accumulation of the test column is to stop the propane flow and to turn off the uniform heat flux at the same time. Immediately after that, the two thermofoil heaters (5 and 6 in Figure 3.8) are turned on to heat the cold block for 30 seconds. When the cold block is warmed, the 3-way valve II (in Figure 3.1) is turned to the left to switch counterflow to the warm direction, and the moving heater and the stepper motor are turned on simultaneously to provide the intensive local heating over the test column from the cold end. During this period, the TCD detects the concentration of migrating contaminant.**

The time history of temperature at point 3 (in Figure 3.6) is shown in Figure 3.15. In this graph, the time was chosen as zero when the moving heater started to move. The top of heater reached at  $t=18$  sec and the bottom passed at  $t=25$  sec. During the period, a very fast temperature increase was obtained. Since the sublimation temperature corresponding contaminant concentration of a few thousand ppm is in between 140 to 150 K, most of the contaminant accumulated at the location migrated within 2 seconds. Therefore, this heating could be considered as satisfactorily rapid.

The small amount of preheating between 10 to 18 sec was due to the natural convection of liquid propane. Temporarily, the column was thermally unstable because the temperature at higher location was lower before the moving heater passed. But the heater velocity was comparatively fast and, as a result, the preheating due to natural convection was very small.

The overshoot at the end of heating was due to the condensation of tailing bubbles and the radial temperature difference. The bubbles generated on the sides of the heater were expected to be condensed immediately because of the close cold wall, but the bubbles at the tail were expected to condense gradually. The temperature was measured on the outer surface of outer tube, and the inner tubes would have some amount of time lag in heating because of a slower heat transfer. In other words, the temperature of inner tubes would be lower than that of outer tube at the same height. The later thermal equilibrium between these tubes was the other reason for the overshoot.

The obtained time history of temperature was good enough to provide the condition for producing the spatial distribution of wall accumulation from the detector output. Critical results obtained in this phase will be presented and discussed in next chapter.



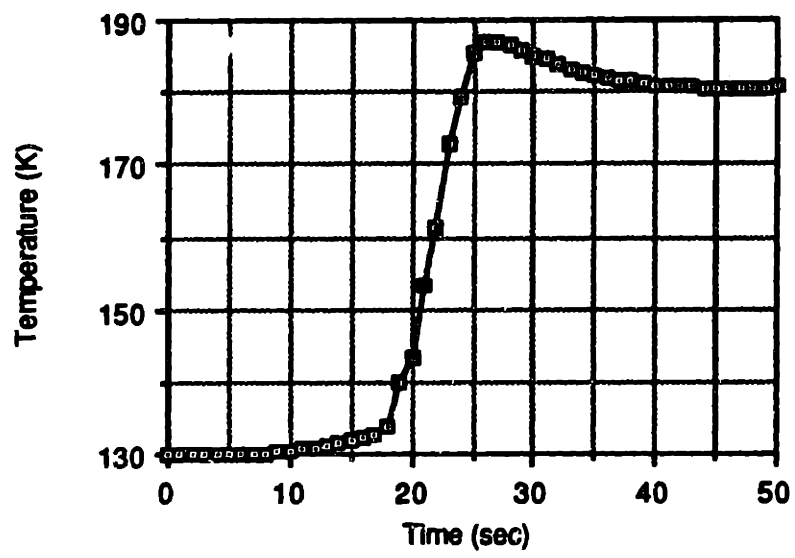


Figure 3.15 Time History of Temperature at Point 3

## Chapter 4

### Results and Discussion

This chapter presents the critical results of the experiment and discusses them with the analytical results of Chapter 2. The time history of the detector output successfully reflected the spatial distribution of wall accumulation in the test column. The same experiment was run for various input parameters, which determined the degree of super-saturation of contaminant. For a small degree of super-saturation, the spatial distribution reasonably coincided with that of the analytical results with no snow-formation assumption (Section 2.3.3). For a large degree, snow formation and its accumulation on the wall were clearly observed. A qualitative description for the behavior of snow was made from the analytical model, which was in good agreement with the experimental results. The observed transition from the no-snow to the snow condition was used to determine the onset condition of snow formation in terms of the degree of super-saturation.

#### 4.1 Test Conditions and Experimental Results

Out of four input parameters (temperature gradient, flow rate, total pressure, and dimensions of tube), gas flow rate and total pressure were easily varied in the experiment. The variation was, however, limited to a certain range because of the operation of the gas analyzer. Too little flow rate caused short life of the filaments in the TCD cells and resulted in much dispersion of the concentration wave. Too much flow rate also resulted in much dispersion, in

accordance with large convection augmented diffusion, as discussed earlier. The TCD cells were designed for a limited working pressure.

The selected test conditions are listed in Table 4.1. The RUN numbers are given only for convenience. The results of RUNs 3 to 6 (shown with bold characters in Table 4.1) are focused on in the present chapter, because variation of the degree of super-saturation by changing the fluid velocity yielded different characteristics for the formation and migration of snow. Details of the remaining results are shown in Appendix F.

Figures 4.1 through 4.4 show the TCD outputs of RUNs 3 through 6, respectively. The time is zero at the start of heater movement and the TCD output is in the units of ppmCO<sub>2</sub>. Five important observations should be made for these results.

First, the contaminant concentrations at the start and at the end were about zero and 100 ppm, respectively. Since the cold block temperature was about 100 K, the test gas became almost carbon dioxide free. After heating of the column was completed, the test gas retained the inlet concentration, 100 ppm, because every location of the column was at higher than the sublimation temperature corresponding to the inlet partial pressure of contaminant.

The second observation is the peak location in the time axis. The location was determined by the test gas velocity and the distance to the accumulation peak from the cold end in the test column. As the velocity increased from RUN 3

to 6, the peak appeared earlier because the temperature gradients differed little from run to run.

The third observation is the magnitude of TCD output. The magnitude was determined by accumulation time, which was about 4 to 5 minutes as listed in Table 4.1. The magnitude at the peak was also related with the amount of dispersion, as discussed below.

The fourth observation is about the dispersion of the concentration wave. One may observe that the biggest dispersion was in RUN 3 and the smallest was in RUN 5, because there existed an optimum velocity for the minimum dispersion. The sources of dispersion and their details will be discussed in the next section.

The final and the most important observation is the shape of the peak. In RUN 3, the concentration wave was too dispersed (because of slow gas velocity) to obtain the spatial distribution of wall accumulation. In RUN 4, the dispersion was much less and the shape of the peak was similar to the shape of wall accumulation without snow formation. In RUN 5, a small secondary peak was obtained in addition to the expected shape and in RUN 6, it became bigger. The secondary peaks were asserted to be from the snow which formed in the middle of tube due to a large super-saturation and, subsequently, accumulated on the wall. Note that the degree of super-saturation got larger from RUN 3 to 6 according to Eqn. (2.87). The snow formation and accumulation will be treated in detail in the next section.

**Table 4.1 List of Test Conditions**

<b>RUN</b>	<b>P<sub>t</sub> Total Press. (KPa)</b>	<b>u<sub>m</sub> * Mean Velocity (m/sec)</b>	<b>- (dT/dx) Temp. Grad. (K/m)</b>	<b>Re * Reynolds No.</b>	<b>T<sub>0</sub> Sublim. Start. Temp. (K)</b>	<b>t<sub>acc</sub> Acc. Time (sec)</b>
1	163	0.242	75.0	13.6	126.5	275
2	163	0.421	72.6	23.7	126.5	265
3	191	0.057	82.2	3.8	127.2	270
4	191	0.172	70.2	11.5	127.2	240
5	191	0.286	74.3	19.1	127.2	250
6	191	0.400	66.5	26.7	127.2	270
7	287	0.049	75.5	4.6	129.4	250
8	287	0.146	75.4	13.6	129.4	260
9	287	0.244	72.1	22.8	129.4	225
10	398	0.106	75.2	14.8	131.1	255
11	398	0.191	74.1	26.7	131.1	275

\* Evaluated at the sublimation starting point

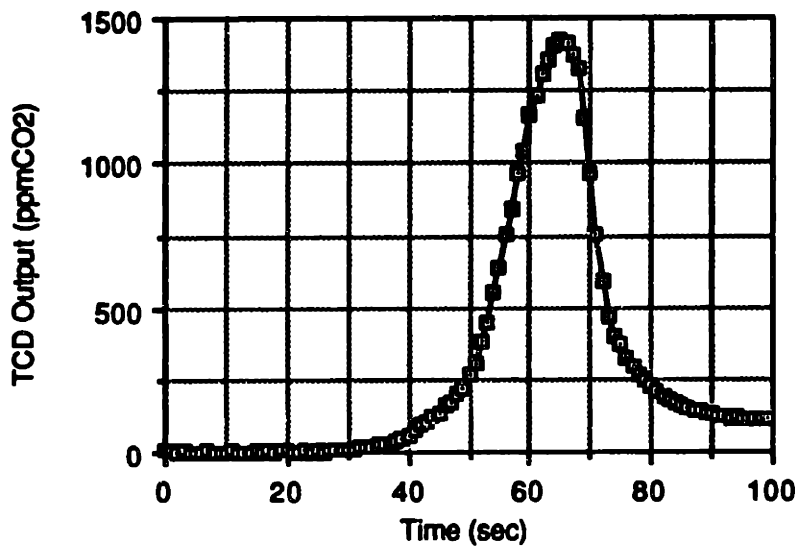


Figure 4.1 TCD Output of RUN 3

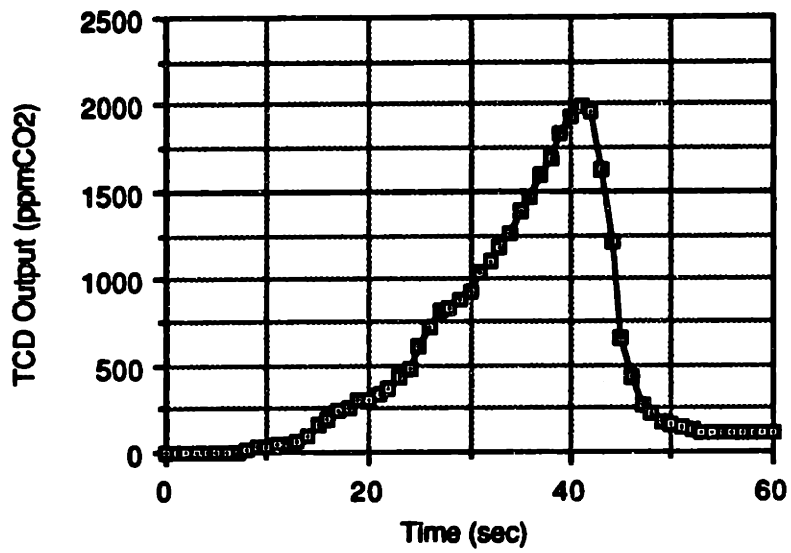


Figure 4.2 TCD Output of RUN 4

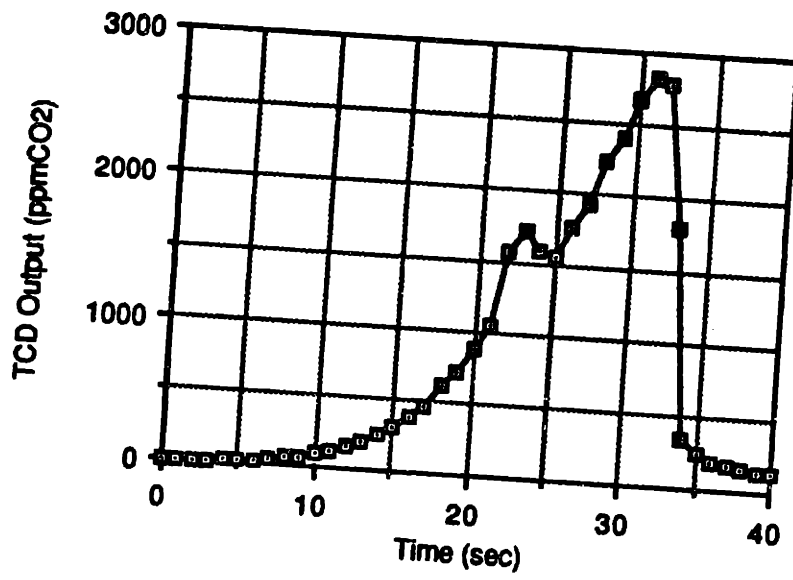


Figure 4.3 TCD Output of RUN 5



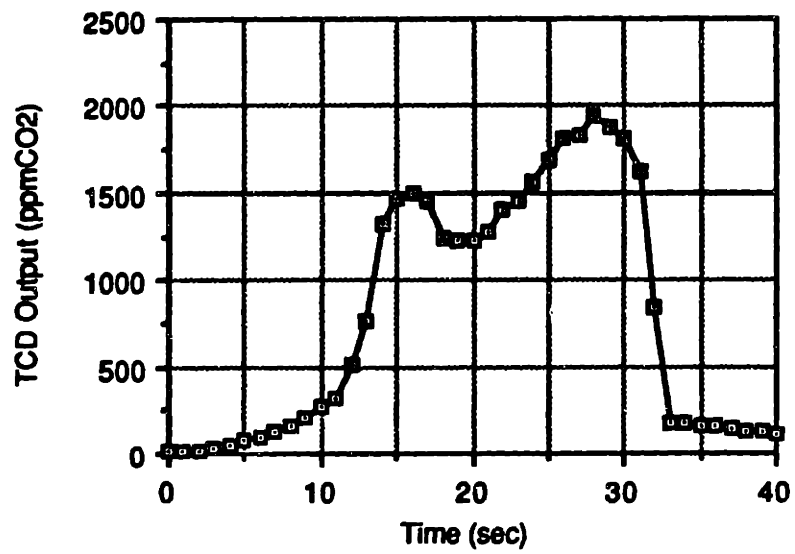


Figure 4.4 TCD Output of RUN 6

## 4.2 Interpretation of Results

To interpret the experimental results with the analytical description, the time history of TCD outputs should be converted into a spatial distribution of wall accumulation. A complete procedure includes solving an integral equation for the dispersion mechanisms. In addition to the mathematical complicity, the major dispersion mechanism can hardly be modelled to analytical form, as described below. In other words, the loss of information in the experiment cannot be recovered in an analytical way.

In this section, instead of the complete recovery, a simple coordinate transformation, from concentration vs. time to corresponding accumulated mass vs. axial distance, is performed. The transformed spatial distribution is used to compare the experimental results with the analytical results. Before this step, the dispersion mechanisms and their estimated amounts are discussed because they are related with part of discrepancy between the analytical and experimental results.

### 4.2.1 Dispersion Mechanisms

The time history of TCD output is dispersed from the spatial distribution of wall accumulation by four different mechanisms. First, the finite heating length allows some amount of mixing of contaminant from different locations of accumulation, which results in a dispersed concentration wave. If the mass accumulated on the wall denotes  $M_{acc}(x)$ , then the mass accumulation with a

finite heating length may be considered as a seemingly effective mass accumulation with a point heater such that

$$\{ M_{\text{acc}}(x) \}_{\text{eff}} = \frac{1}{L_h} \int_{x-L_h/2}^{x+L_h/2} M_{\text{acc}}(\xi) d\xi \quad (4.1)$$

where  $L_h$  is the effective heating length and is approximately 2 cm as discussed in the previous chapter. To be exact, the integration in Eqn. (4.1) should be weighted by proper sublimation data for the contaminant, because the contaminant does not migrate uniformly while the temperature increases. But, to an estimation order, Eqn. (4.1) is acceptable.

The second dispersion occurs in a round tube between the test column and the detector by the convection augmented diffusion as introduced in Appendix D. The amount of dispersion can be estimated from solving the 1-D convection-diffusion equation with an effective mass diffusivity, which is obtained also in Appendix D.

$$\frac{\partial c}{\partial t} + u_m \frac{\partial c}{\partial x} = D_{\text{eff}} \frac{\partial^2 c}{\partial x^2} \quad (4.2)$$

A method to solve Eqn. (4.2) is to use the Green's function, derived in Appendix E. If the initial concentration is  $c(x,t=0)$ , then

$$c(x,t) = \int_{x'=-\infty}^{\infty} G(x,t; x',0) c(x',0) dx' \quad (4.3)$$

Since the effective diffusivity,

$$D_{\text{eff}} = D + \frac{u_m^2 d^2}{192 D}, \quad (4.4)$$

should be included in the Green's function in Eqn. (4.3), the amount of dispersion depends on the mean velocity,  $u_m$ , and the time,  $t$ , allowed for the dispersion. As shown in Section D.3, there exists an optimum velocity to produce minimum dispersion for the given length of tube, which is

$$(u_m)_{\text{opt}} = \sqrt{192} \frac{D}{d}. \quad (4.5)$$

The optimum mean velocity of carbon dioxide in a 1 mm ID tube is 0.45 m/sec at pressure of 191 KPa (pressures of RUNs 3 to 6) and room temperature.

The third dispersion is caused through tube fittings, the control valves and other non-uniform cross-sectional elements. The dispersion through such complex geometries may not be easily estimated, because the flow pattern includes separation, reattachment, eddy, and so on. But the mechanism is essentially a diffusion augmented by convection. The amount of dispersion is expected to be much more than dispersion in a round tube and to depend on the gas flow rate.

The fourth dispersion occurs in the detector cells. Because of the response time, the detected concentration is more dispersed than the concentration of the migrating wave, which is estimated by a first-order model,

$$\tau \frac{dc_{\text{det}}}{dt} + c_{\text{det}} = c_{\text{in}}, \quad (4.6)$$

where  $\tau$  is the response time of the detector, which is equal to about 1 sec, and  $c_{\text{det}}$  and  $c_{\text{in}}$  are the detected and incoming concentrations, respectively.

#### 4.2.2 Experimental and Analytical Distributions of Wall Accumulation

To compare the experimental results with the analytically obtained distribution of wall accumulation without snow formation, the time history of TCD output is converted to the wall accumulation by simple coordinate transformation. As mentioned at the beginning of this section, the transformation does not include any dispersion mechanisms.

The concentration of contaminant at the ideal point heater,  $c_h(t)$ , is determined by the amount of mass accumulation per unit length,  $M_{acc}(x)$  such that

$$c_h(t) = \frac{M_{acc}(L_{test} - v_h t)}{A \left(1 + \frac{u_m}{v_h}\right)}, \quad (4.7)$$

where  $A$  is the cross-sectional area of tube,  $L_{test}$  is the test length or the distance from the sublimation starting point to the cold end, and  $v_h$  is the speed of the heater, moving from the cold end. As before, the axial coordinate,  $x$ , is selected to be positive in the gas flow direction from the sublimation starting point, and the time,  $t$ , is zero when the moving heater starts. Eqn. (4.7) is obtained by letting the location of the heater be expressed by  $(L_{test} - v_h t)$ . The term,  $(1 + u_m/v_h)$ , in the denominator comes from the spreading effect due to the gas and heater velocities in the reverse direction. These relations are schematically shown in Figure 4.5.

Since the contaminant migrates with the mean flow velocity to the detector, the concentration at the detector,  $c_{det}(t)$ , is obtained as

$$c_{det}(t) = c_h \left( t - \frac{L_{det}}{u_m} \right) \quad (4.8)$$

where  $L_{det}$  is the distance from the test column to the TCD cell, which should include every dead volume in its equivalent length of the tube cross-sectional area and was determined by a simple experiment to measure the time for a concentration wave to migrate from the test column to the detector. In Eqn. (4.8),  $L_{det}$  is assumed constant because the heater's moving distance is much smaller than  $L_{det}$ .

From Eqns. (4.7) and (4.8), the mass accumulation per unit length is obtained for a given time history of TCD output,  $c_{det}(t)$ .

$$M_{acc}(x) = A \left( 1 + \frac{u_m}{v_h} \right) c_{det} \left( \frac{L_{test} - x}{v_h} + \frac{L_{det}}{u_m} \right) \quad (4.9)$$

In other words, the desired coordinate transformation can be performed by letting

$$M_{acc} = \frac{A P_{tot}}{RT} \left( 1 + \frac{u_m}{v_h} \right) (\text{ppmCO}_2 \times 10^{-6}) \quad (4.10)$$

and

$$x = L_{test} - \left( t - \frac{L_{det}}{u_m} \right) v_h \quad (4.11)$$

In Eqn. (4.10), the total pressure,  $P_{tot}$ , and the temperature,  $T$ , are the values at the detector.

The transformed mass accumulations for RUNs 4 through 6 are shown in Figure 4.6 through 4.8, respectively, along with the corresponding analytical result, which is the mass accumulation rate from Eqn. (2.36) multiplied by the accumulation time shown in Table 4.1.

For RUN 4, the discrepancy is mostly due to the dispersion in the experiment, because the analytical distribution yields a similar shape to the experimental distribution after some amount of dispersion. The spatial distribution of wall accumulation in this run is estimated to coincide with the analytical prediction without snow formation, which means that the degree of super-saturation was not big enough to produce a noticeable amount of snow.

The dispersion due to the first and second mechanisms of the previous sub-section results in almost non-distinguishable amount if Eqns. (4.1) and (4.3) are numerically calculated from the analytical distribution. The dispersion due to the fourth mechanism, estimated by Eqn. (4.6), is also very small except the tailing part which corresponds to the fast change near  $x=0$ . Most of the dispersion results from the third mechanism; through the tube fittings and valves. As mentioned earlier, the mechanism is essentially due to diffusion augmented by fluid convection. Therefore, there exists an optimum velocity for the minimum "overall" dispersion, even if it is not exactly given by Eqn. (4.5). The order of the optimum velocity is slightly bigger than 0.45 m/sec, the optimum velocity for the round tube, because the cross-sectional areas of the tube fittings and valves are smaller than the tube so an equivalent diameter in Eqn. (4.5) should be smaller. The flow velocity of RUN 4 is 0.41 m/sec at room



temperature, which is certainly below the optimum velocity, and, as a result, the dispersion was more than the minimum.

RUN 5 has almost the same condition as RUN 4, except a larger flow rate. The flow velocity is 0.69 m/sec at room temperature, which is estimated about the optimum for minimum dispersion. The experimental distribution matches the analytical distribution very closely except a small secondary peak. As mentioned earlier, this secondary peak is due to the accumulation of formed snow on the wall, from the following qualitative description.

As shown in Figure 4.9 (a), the super-saturated contaminant starts to nucleate at the location of maximum degree of super-saturation (point 1) where  $x=L_e$  or mass transfer entry length. As the nuclei grow to snow, the concentration of gaseous contaminant decreases locally as shown at point 2. The sudden decline of concentration is flattened by a fast mass transfer, which results in a smaller super-saturation or even an under-saturation of contaminant (point 3 to 4). The concentration profile followed by the formation of snow affects the distribution of wall accumulation by mass transfer such that the  $M_{acc}(x)$  decays faster than that without snow formation (dotted curve) as shown at the top of Figure 4.9 (b). The formed snow migrates by the gas to a certain location and is deposited on the wall as shown by the second figure. Its migration length,  $L$ , and the deposition width,  $\sigma$ , are expected to be determined by the relation of the size and shape of snow crystals, exact location of snow formation, flow velocity, surface condition of wall, and so on. A short qualitative discussion concerning this behavior will be presented in the next section. The total mass accumulated on the wall has the shape as shown at the bottom of Figure 4.9 (b).

With this reasoning in RUN 5 the formed snow is interpreted to have migrated to about 100 times the tube diameter (10 cm) before its deposition to the wall within a length of 40 times the diameter (4 cm). At least, 2% of the total contaminant has been formed into snow.

In RUN 6, the dispersion is bigger again because the flow velocity exceeds the optimum. The amount of formed and migrated snow is about 11% of the total mass, which is greater than that of RUN 5 because of the greater degree of super-saturation. The snow migration length and the deposition width are about 150 times (15 cm) and 60 times (6 cm) the tube diameter, respectively. One of the reasons for these bigger values is the faster gas velocity.

There seems to exist simple relations between the amount of snow formed and the degree of super-saturation or between the migration length and the gas velocity. But the experimental results are not accurate at higher flow velocities because of too much dispersion. In addition, the flow rate of RUN 6 is almost the maximum that the gas analyzer unit allows. While those relations can be found, valid in a short range, the information obtained from them may not be very important. Therefore, instead of the specific relations, a dimensional consideration for the obtained analytical and experimental results is presented to draw significant conclusions for practical helium systems, in the remaining sections of this chapter.

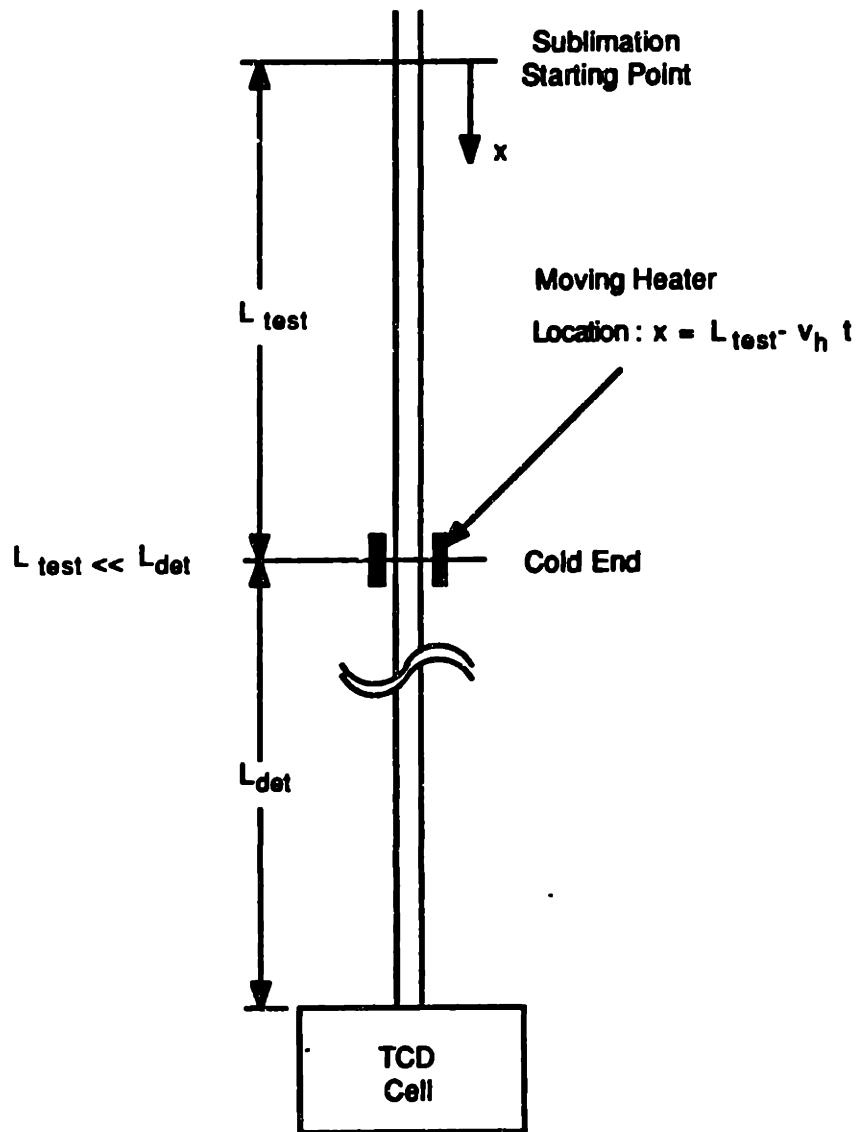
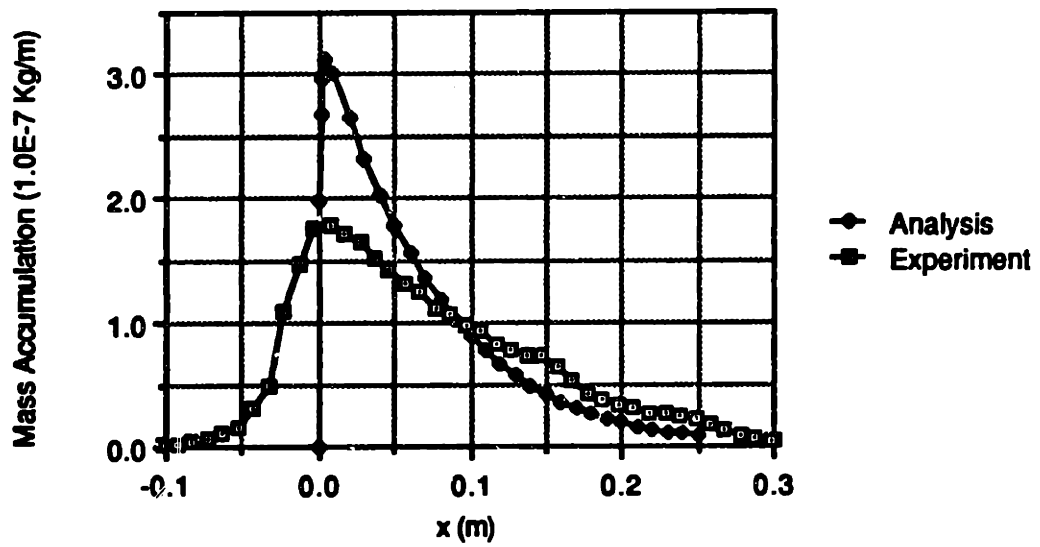
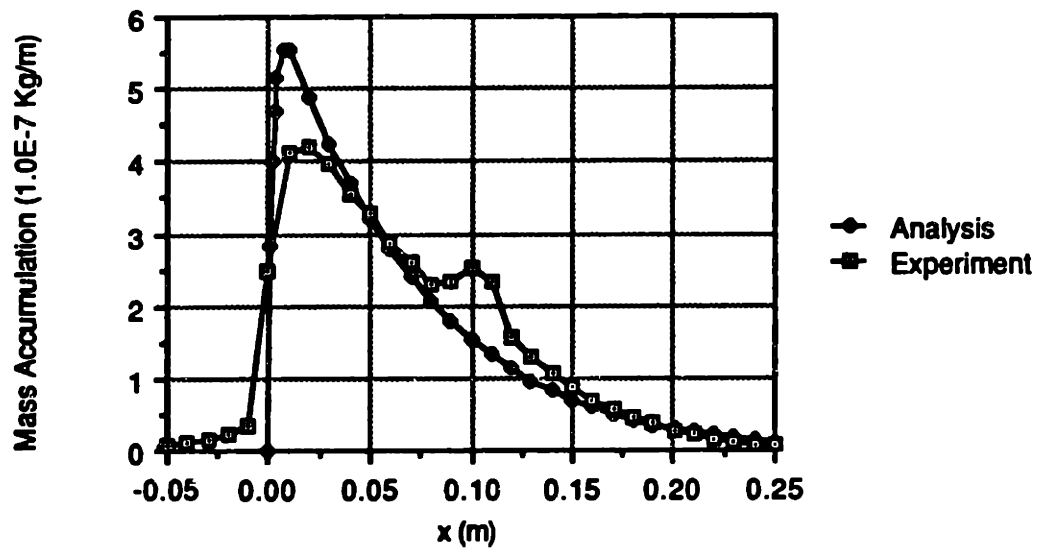


Figure 4.5 Explanation for the Test and Detection Length



**Figure 4.6 Experimental and Analytical Distribution of the Mass Accumulation for the RUN 4**



**Figure 4.7 Experimental and Analytical Distribution of the Mass Accumulation for the RUN 5**

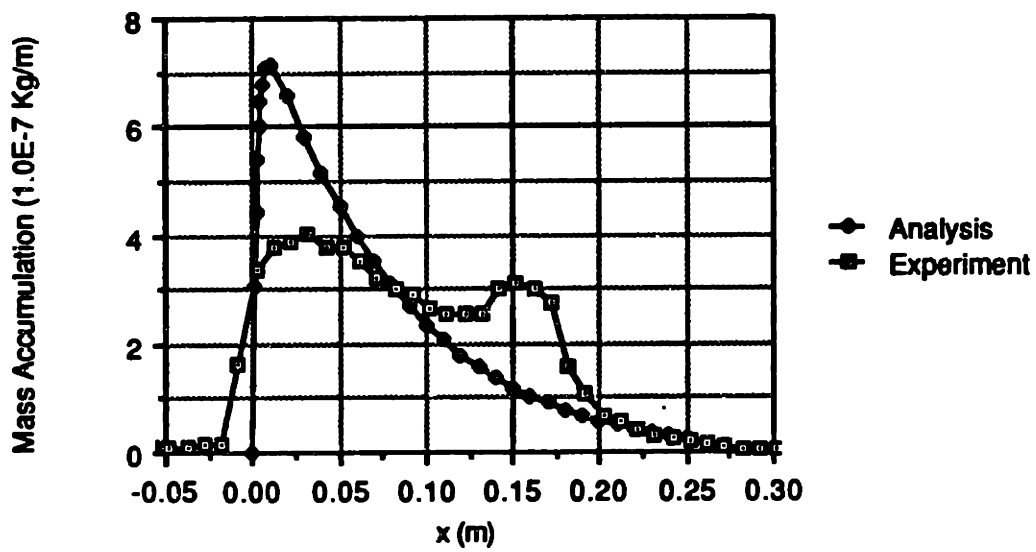


**Figure 4.8 Experimental and Analytical Distribution of the Mass Accumulation for the RUN 6**

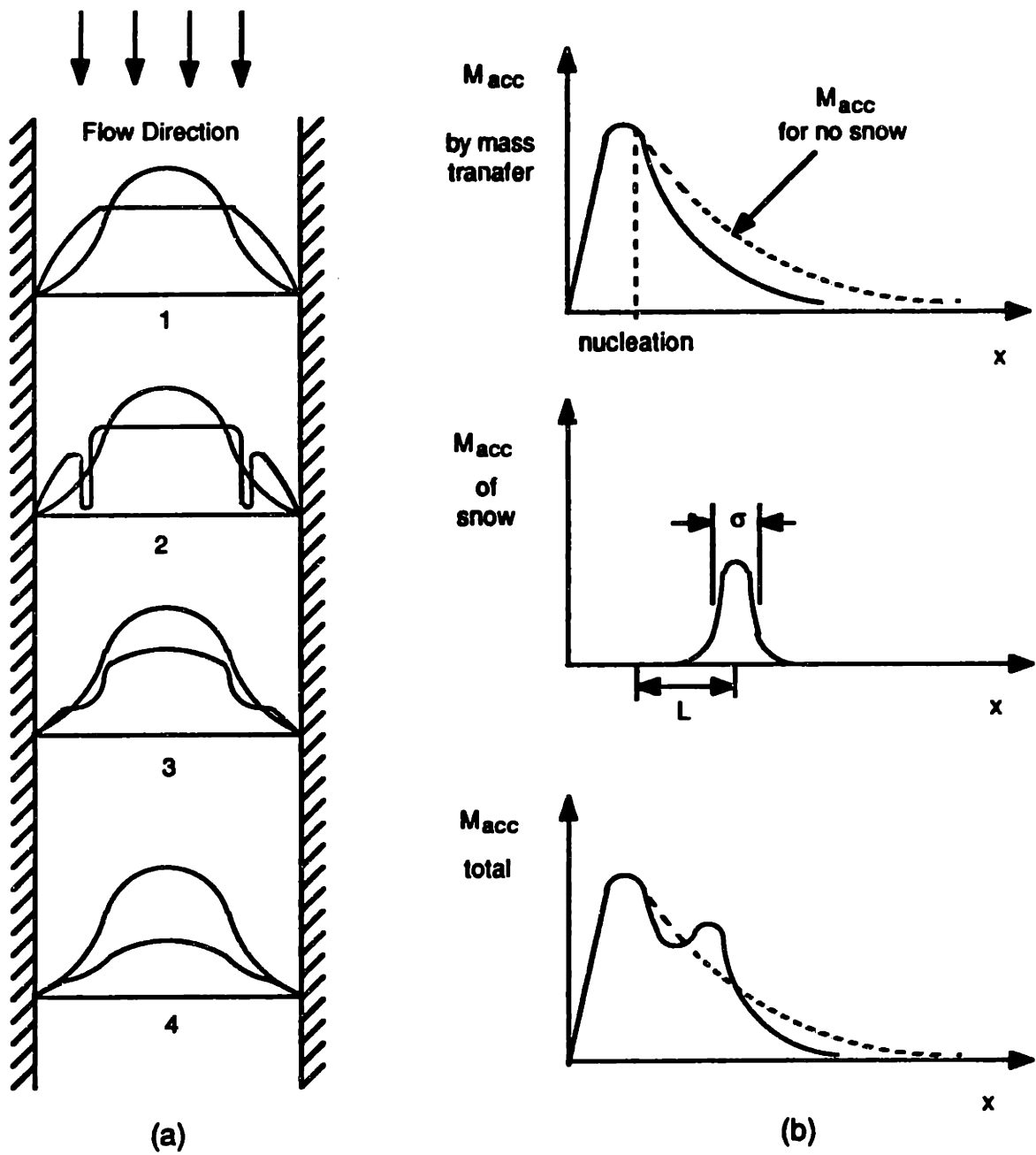


Figure 4.9 Effect of Snow Formation on the Concentration Profile and the Distribution of Wall Accumulation

## 4.3 Discussions

### 4.3.1 Onset of Snow formation

As presented in the previous section, a clear transition from the no-snow to snow formation was observed when the gas flow velocity was increased for a given total pressure and almost same temperature gradient. The similar transition was obtained for other runs as shown in Appendix F. Based on these results and a dimensionless degree of super-saturation, defined at the end of Chapter 2, a prediction for the onset of snow can be made.

For the test conditions listed in Table 4.1, the DSS (degree of super-saturation) given by Eqn. (2.87) is calculated and summarized in Table 4.2. Out of the various test conditions, the obvious peaks due to snow formation and its deposition on the wall are observed for RUNs 2, 5, 6, 9, and 11, as shown in Appendix F. The values of DSS, defined by

$$DSS = 0.0332 \left( \frac{C_p d}{H_{ig}} \right)_0 \left( -\frac{dT_w}{dx} \right)_0 (Re Sc) \quad (4.12)$$

for those runs are greater than  $(8 \times 10^{-5})$  and the values for the other runs are less than  $(8 \times 10^{-5})$ . Figure 4.10 displays the test points in dimensionless temperature gradient,  $(Rd)(-dT/dx)/H_{ig}$ , vs.  $(Re Sc)$  diagram. A clear separation by a constant DSS curve is observed between the snow and no-snow conditions.



As discussed in Section 2.4.2, even if the DSS may not be the only factor affecting the onset of nucleation for the snow, it is an important property determining the environment for the onset. Therefore, the onset of snow formation can be generally predicted when the value of DSS is greater than ( $8 \times 10^{-5}$ ).

In order to avoid the snow formation, either the dimensionless temperature gradient or the Reynolds times Schmidt number should be reduced. The former can be achieved by a smaller temperature gradient or by smaller  $(C_p d / H_{ig})_0$  and the latter by smaller Reynolds number. In other words, small flow rate and large heat exchanger length with small flow passage would reduce the degree of super-saturation and the probability of snow formation.

The latent heat of sublimation,  $H_{ig}$ , involves the effect of inlet partial pressure, which is the total pressure times the mole fraction of contaminant, because the partial pressure determines the sublimation starting temperature. For carbon dioxide,  $H_{ig}$  was nearly independent on the inlet pressures of the experiment and as a result, the onset was not dependent on the total pressure. But this may not be true for other contaminants. Therefore, the temperature dependence of the heat of sublimation should be examined carefully if the onset of snow formation for a contaminant is to be predicted.

**Table 4.2 The Degree of Super-Saturation and Snow Formation  
for the Test Conditions**

<b>RUN</b>	<b>(Rd)(-dT/dx)/H<sub>ig</sub> *</b> <b>(10<sup>-5</sup>)</b>	<b>Re Sc *</b>	<b>DSS</b> <b>(10<sup>-5</sup>)</b>	<b>Snow Formation</b>
<b>1</b>	<b>2.35</b>	<b>23.5</b>	<b>6.41</b>	<b>No</b>
<b>2</b>	<b>2.28</b>	<b>41.0</b>	<b>10.8</b>	<b>Yes</b>
<b>3</b>	<b>2.58</b>	<b>6.59</b>	<b>1.97</b>	<b>No</b>
<b>4</b>	<b>2.20</b>	<b>19.9</b>	<b>5.08</b>	<b>No</b>
<b>5</b>	<b>2.33</b>	<b>33.0</b>	<b>8.92</b>	<b>Yes</b>
<b>6</b>	<b>2.09</b>	<b>46.2</b>	<b>11.2</b>	<b>Yes</b>
<b>7</b>	<b>2.37</b>	<b>7.89</b>	<b>2.17</b>	<b>No</b>
<b>8</b>	<b>2.37</b>	<b>23.5</b>	<b>6.46</b>	<b>No</b>
<b>9</b>	<b>2.26</b>	<b>39.4</b>	<b>10.3</b>	<b>Yes</b>
<b>10</b>	<b>2.36</b>	<b>25.6</b>	<b>7.01</b>	<b>No</b>
<b>11</b>	<b>2.32</b>	<b>46.2</b>	<b>12.4</b>	<b>Yes</b>

\* Evaluated at the Sublimation Starting Point

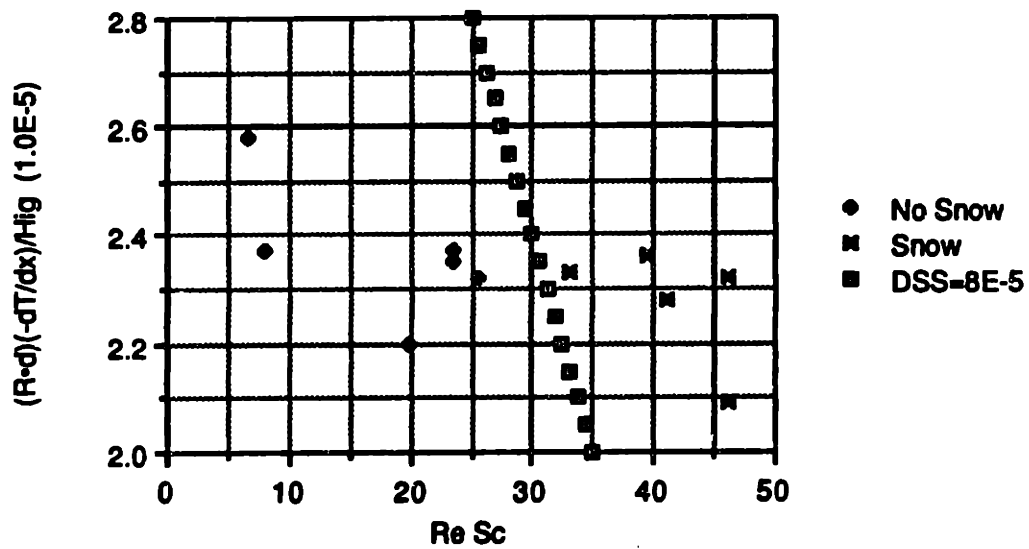


Figure 4.10 Experimental Conditions on a Dimensionless Temperature Gradient vs. Re Sc Diagram

### **4.3.2 Contamination in Practical Helium Systems**

**One of the objectives in this study is to understand the contamination behavior in practical helium systems. Even if an experimental verification of the behavior in the systems may be extremely difficult, a general description is possible based on the obtained results and a dimensional consideration.**

**The most obvious observation is that a vigorous snow formation of every contaminant should occur in practical helium systems. a typical Reynolds number in those systems is well in the order of  $10^3$  or even bigger, and the tube diameter or comparable dimension in Eqn. (4.12) is much bigger than 1 mm. Therefore, the DSS is at least on the order of  $10^{-3}$ , which is well above the DSS for the onset of snow formation, ( $8 \times 10^{-5}$ ).**

**For this large DSS condition, the amount of formed snow out of the total mass of contaminant is expected to be very much. In the experiment, 2 % and 11 % of the total mass of contaminant were formed into snow and migrated by the distance equivalent to the length of 100 and 150 times the tube diameter for DSS values of ( $8.92 \times 10^{-5}$ ) and ( $1.12 \times 10^{-4}$ ), respectively. When DSS is greater than  $10^{-3}$ , only a small amount of contaminant is continuously transported to the wall by mass transfer, being sublimated and accumulated on the wall, and most of it is formed into snow.**

**The large amount of snow formation occurs because the nucleation of contaminant starts much earlier than the end of the mass transfer entry length, where the super-saturation would reach the maximum if no snow formed. The**

early nucleation, in the contaminant with its super-saturation still increasing, is definitely a good environmental condition for the nuclei to grow and form snow. As explained with Figure 4.9, the more snow forms, the smaller the slope of the concentration profile is at the wall and the less the contaminant is accumulated by mass transfer.

The migration of the snow is expected to be characterized by two compensating effects. The first yields more chance to migrate to downstream because of the faster velocity. As observed in the experiment, the snow was deposited further downstream when the velocity was increased. The second effect yields less chance because the location of nucleation is closer to the tube wall. For a very large-DSS flow, nucleation starts long before the mass transfer boundary layer is (semi) fully developed, as mentioned above. In other words, the nuclei start to grow when the boundary layer is still thin, and the chance to be deposited on the wall is increased. As a result, the migration length of snow might not be increased.

In the experimental conditions, the first effect was dominant over the second, so more migration was observed for a larger flow rate with a larger DSS. Extrapolation of these results to the practical helium systems cannot be easily made without any verification, because the behavior of interest has too much order of difference from the verified results. However, it is not an unreasonable prediction that at least some of the formed snow would migrate to its downstream by the length of a few hundred times the tube diameter.

**An important explanation for the contamination of the Collins cycle shown in Figure 1.1 is possible even with the very conservative prediction. Carbon dioxide starts to sublime at above 120 K, and the sublimation of other common contaminants (argon, nitrogen, and oxygen) starts in temperature ranges roughly between 50 and 20 K, and finally neon sublimates below 20 K. Even if most of the contaminants start to sublime at much above the J-T valve temperature, the formed snow due to a large degree of super-saturation may well migrate to the J-T valve, which has the smallest cross-sectional area of passage, and may be deposited around the valve, because the migration length necessary to reach the J-T valve is typically less than a few hundred times the passage diameter. Therefore, the clog-up of the J-T valve is a quite reasonable conjecture for the stoppage of the Collins helium refrigeration cycle.**

**As a summary for the behavior of contaminants in the practical helium systems, it is mentioned again that DSS is much bigger than the verified value for the onset of snow formation and therefore, most of the contaminant would be formed into snow rather than being continuously transported to the wall by mass diffusion.**

# Chapter 5

## Conclusion

### 5.1 Summary of the Study

This study was intended to understand the physics of contamination in cryogenic helium systems. First, the analytical study described the behavior of a contaminant by means of mass transfer theory, which enabled the prediction for the spatial distribution of mass accumulation rate including the probable snow formation.

The system to which the mass transfer theory could be applied was a simple and most significant case: fully-developed laminar flow in a round tube. Several justified assumptions simplified the problem such that the mass transfer of contaminant was a secondary transport phenomenon, subject to the momentum and heat transfer of the main fluid, helium. Based upon those assumptions, the behavior of the contaminant was formulated into a mass convection-diffusion equation and solved analytically, yielding the concentration distribution of contaminant for the given velocity and temperature distributions. In the solution process, a few methods of applied mathematics and analytical heat transfer were involved. From the concentration distribution, the mass accumulation rate on the wall was obtained with no snow-formation assumption. On the other hand, the concentration and temperature distributions provided the degree of super-saturation, which was always positive because the mass transfer was slower than the heat transfer or the Lewis number for the

common contaminants in helium was greater than unity. A linearized and non-dimensionalized expression for the degree of super-saturation (DSS) was defined for the prediction of snow formation and for a dimensional consideration of contamination in practical helium systems.

An experiment was designed and completed to detect the spatial distribution of contaminant accumulation in a test column. After the column was contaminated with 100 ppm carbon dioxide in a well-posed condition, a sharp temperature wave generated by a continuously moving heat source was propagated from the cold to the warm end (opposite to the flow direction), flushing the accumulated CO<sub>2</sub> through the column. A detector measured the concentration of the migrating CO<sub>2</sub> at the exit of the column. Time history of the detector output successfully reflected the spatial distribution, because the continuous heating was locally very intensive and the dispersion of the concentration was minimized.

The test column was selected as a capillary stainless-steel tube with 1.0 mm ID and 2 m long and was placed vertically in a vacuum space. The temperature of the test column was precisely controlled by an auxiliary outer tube filled with liquid propane, which was cooled by liquid nitrogen. For the temperature to be set linear before the contamination, the cold propane flowed through the outer tube at constant rate with a uniform heat flux by spirally wrapped heating wire. A typical temperature distribution was 110 K (cold/bottom end) to 270 K (warm/top end). After several minutes of contamination, a small thermfoil heater in the propane-filled space was pulled up from the cold end at the speed of 1 cm/sec, by a stepper motor located at the top plate. The heat flux



generated by the heater was as high as  $(1.0 \times 10^5)$  Watts/m<sup>2</sup>. Burn-out of the heater was avoided by a fast heat transfer accompanying boiling and immediate condensation of the liquid propane. As a result, the temperature at one location of the column was increased by 50 K within 7 seconds.

The detector was a fast response Thermal Conductivity Detector, supplied for typical Gas Chromatography applications. The test conditions were in the ranges of 3 to 30 Reynolds number flow, 160 to 400 KPa total pressure, 65 to 85 K/m temperature gradient, and 4 to 6 minute contamination time.

When the super-saturation of contaminant was small, the contaminant was continuously diffused to the tube wall and sublimated without any noticeable snow formation, as the analysis described. When the super-saturation increased, a formation of snow and its deposition on the wall at a distance (about 100 times of diameter) from the formed location were clearly observed. This transition was separated with a single parameter, a constant DSS ( $DSS = 8 \times 10^{-5}$ ), for the various runs of experiment. The amount and the migration length of the formed snow increased with DSS. However, the experiment did not allow a wide variation of the test conditions to generalize the characteristics of this behavior.

## 5.2 Conclusions

Two different categories of conclusions can be made in this study. The first involves the behavior of carbon dioxide for small Reynolds number flows in a round tube as verified in the experiment. The second is associated with the general behavior of common contaminants in helium systems, predicted by the analytical description and the conclusions of the first category.

For a condition with DSS less than  $(8 \times 10^{-5})$ , carbon dioxide as a contaminant in helium is continuously transported to the tube wall by molecular diffusion and sublimated to the wall in spite of its super-saturation. For DSS greater than  $(8 \times 10^{-5})$  and less than  $(1.5 \times 10^{-4})$ , some of the carbon dioxide forms snow at around the end of mass transfer entry region and is accumulated on the tube wall at a distance from the formed location. The amount of formed snow is less than 30 % of total contaminant and the migration length is about 100 to 200 times of diameter.

In practical helium systems, since an equivalent DSS is estimated typically to the order of  $10^{-3}$  to  $10^{-2}$  for every common contaminant, the snow formation is predicted to be very active, and at least some of the formed snow is expected to migrate further downstream.

An effective control of the snow formation and migration is suggested as a critical way to reduce the detrimental effects of contamination. To reduce the amount of snow formation, the systems should be designed to have small DSS by reducing the temperature gradient, the effective flow passage, and the flow

rate. The effect of the contamination level and the total pressure on the amount of snow formation should be examined with the sublimation data for the contaminants. To reduce the migration of snow to the J-T valve or to other smaller cross-sectional passage, the best geometry or flow conditions are not clear from this study. A few proper snow traps in between the contaminant sublimation location and the J-T valve might be effective to reduce the migration.

### **5.3 Recommendations for Further Study**

**Three important recommendations are made for the better understanding of the contamination behavior and for the improvement of the contamination problem in practical systems.**

**First, an extended experiment for the various flow conditions and geometries is recommended. The experiment may include higher Reynolds number covering the turbulent flow region, other common contaminants of helium, various shapes of heat exchanger, and J-T valve.**

**Second, as an intensive local heating method in the experiment, a "laser beam" is strongly recommended. A laser with tens of Watts power may fit the heating requirements of the experiment involving the lower temperature contamination, which cannot be obtained by a sub-cooled boiling heat transfer. Another significant advantage of the laser heating is that the power source and traversing system can be placed outside the vacuum chamber.**

**Finally, an analytical study for the detailed behavior of snow formation and migration is recommended. Especially, the snow formation when more than one contaminant are nucleated and grow in close temperature ranges (for example, oxygen and nitrogen) may be an interesting topic. Relations of the snow growth and the concentration distribution of contaminant may be important in migration characteristics.**

# Appendix A

## Sublimation Data of Carbon Dioxide

One of the nice fitting expressions for the pressure-temperature relation of sublimation curve <sup>27</sup> is given by

$$\ln \left( \frac{P}{P_t} \right) = a \left( 1 - \frac{T_t}{T} \right) + b \ln \left( \frac{T}{T_t} \right) + c \left( \frac{T}{T_t} - 1 \right) + d \left\{ \left( \frac{T}{T_t} \right)^2 - 1 \right\} + e \left\{ \left( \frac{T}{T_t} \right)^3 - 1 \right\} \quad , (A.1)$$

where

$$a = 14.57893$$

$$b = -14.48067$$

$$c = 63.35685$$

$$d = -47.14593$$

$$e = 14.53922$$

and

$$T_t = \text{Triple Point Temperature}$$

$$= 216.58 \text{ K}$$

$$P_t = \text{Triple Point Pressure}$$

$$= 518.5 \text{ KPa}$$

for carbon dioxide. Eqn. (A.1) is good for the temperature range from the triple point down to 90 K. The temperature derivative of the sublimation pressure is of special interest, and is expressed as

$$\frac{dP}{dT} = \frac{P}{T_t} \left\{ a \left( \frac{T_t}{T} \right)^2 + b \left( \frac{T_t}{T} \right) + c + 2d \left( \frac{T}{T_t} \right) + 3e \left( \frac{T}{T_t} \right)^2 \right\} \quad . \quad (A.2)$$

The latent heat of sublimation,  $H_{ig}$ , can be obtained from the Clausius-Clapeyron Equation, which is

$$\frac{dP}{dT} = \frac{H_{ig}}{T v_{ig}}, \quad (\text{A.3})$$

where  $v_{ig}$  is the difference of specific volumes for the gaseous and solid phase. Since gaseous specific volume is much greater,

$$H_{ig} = \frac{RT^2}{P} \frac{dP}{dT} \quad (\text{A.4})$$

or from Eqn. (A.2)

$$H_{ig} = RT \left\{ a \left( \frac{T}{T_t} \right) + b + c \left( \frac{T}{T_t} \right) + 2d \left( \frac{T}{T_t} \right)^2 + 3e \left( \frac{T}{T_t} \right)^3 \right\}, \quad (\text{A.5})$$

which is a third order polynomial plus a hyperbola.

Table A.1 and Figures A.1 to A.3 show the numerical values of sublimation pressure, its temperature derivative, and latent heat of sublimation, for the temperature range, 110 to 150 K.

**Table A.1 Sublimation Data of Carbon Dioxide**

<b>Temperature (K)</b>	<b>Sublimation Pressure (Pa)</b>	<b>Derivative of Pressure (Pa/K)</b>	<b>Heat of Sublimation (KJ/Kg)</b>
110	0.379	0.099	598.699
111	0.491	0.126	599.029
112	0.634	0.160	599.340
113	0.815	0.203	599.632
114	1.043	0.255	599.905
115	1.329	0.319	600.158
116	1.686	0.398	600.392
117	2.131	0.495	600.607
118	2.683	0.613	600.803
119	3.365	0.756	600.979
120	4.204	0.929	601.136
121	5.235	1.138	601.247
122	6.494	1.389	601.392
123	8.029	1.690	691.491
124	9.893	2.049	601.572
125	12.150	2.476	601.633
126	14.872	2.983	601.676
127	18.147	3.584	601.700
128	22.075	4.291	601.706
129	26.772	5.124	601.694
130	32.371	6.100	601.664
131	39.027	7.242	601.606
132	46.928	8.574	605.551
133	56.248	10.124	601.468
134	67.248	11.912	601.369
135	80.185	14.002	601.253

**Table A.1 Sublimation Data of Carbon Dioxide (Continued)**

<b>Temperature (K)</b>	<b>Sublimation Pressure (Pa)</b>	<b>Derivative of Pressure (Pa/K)</b>	<b>Heat of Sublimation (KJ/Kg)</b>
136	95.360	16.404	601.121
137	113.116	19.171	600.973
138	133.841	22.351	600.810
139	159.972	25.995	600.631
140	186.004	30.162	600.438
141	218.491	34.917	600.231
142	256.058	40.331	600.010
143	299.400	46.463	599.776
144	349.297	53.457	599.528
145	406.620	61.347	599.269
146	473.331	70.257	598.998
147	547.510	80.297	598.716
148	633.344	91.590	598.423
149	731.149	104.266	598.120
150	842.384	118.471	597.808



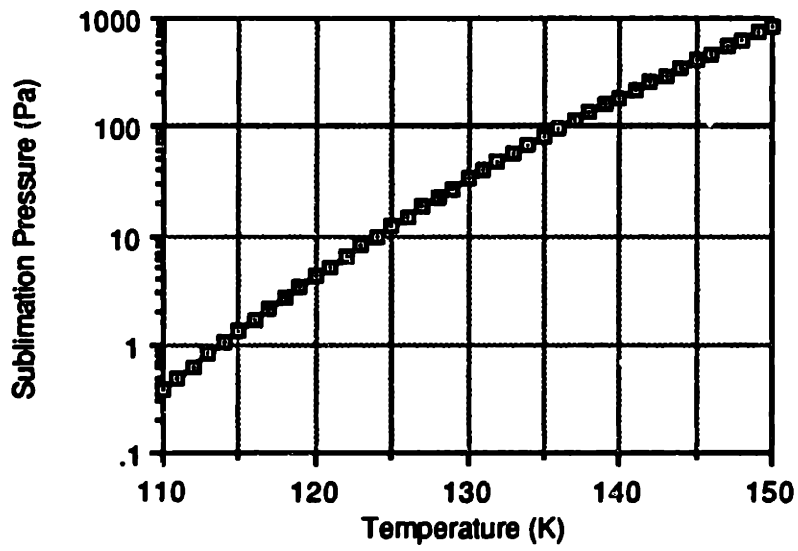
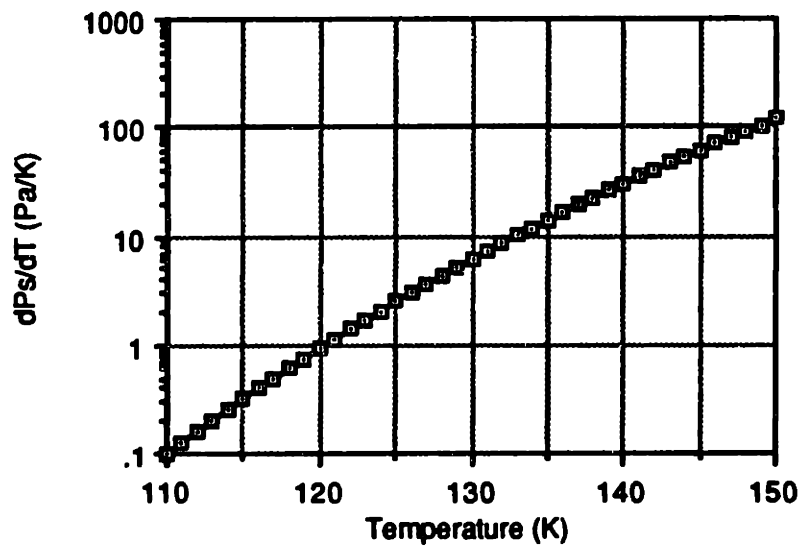


Figure A.1 Sublimation Pressure of Carbon Dioxide



**Figure A.2 Temperature Derivative of Sublimation Pressure  
of Carbon Dioxide**

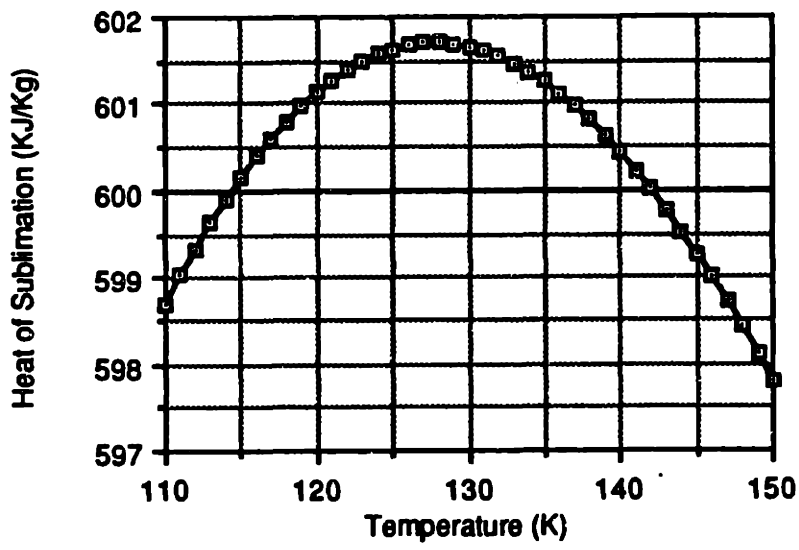


Figure A.3 Latent Heat of Sublimation of Carbon Dioxide

## Appendix B

### Graetz Functions

This appendix presents the properties of the solutions of a specific Sturm-Liouville problem, so called Graetz equation,

$$r R_n'' + R_n' + \lambda_n^2 r (1 - r^2) R_n = 0 \quad (\text{B.1})$$

with boundary conditions,  $R_n(1)=0$  and  $R_n(0)=1$ , where  $R_n$  and  $\lambda_n$  are the  $n$ -th eigen-function and eigen-value, respectively. Instead of deriving a series form of exact solution, asymptotic behaviors<sup>8</sup> in two limiting cases ( $r \approx 0$  and  $r \approx 1$ ) and in the medium range between them are sought, because many useful results are obtained from them.

For small  $r$ , or near the center of tube, Eqn. (B.1) becomes the Bessel equation of order zero since  $\lambda_n^2 r (1-r^2)$  becomes  $\lambda_n^2 r$ . So the asymptotic behavior is simply expressed as

$$R_n(r) \approx J_0(\lambda_n r), \quad (\text{B.2})$$

where the second solution of the Bessel equation,  $Y_0$ , did not appear because of the boundary condition at  $r=0$ .

For medium  $r$  between 0 and 1, its asymptotic behavior is found with so-called WKB theory<sup>30</sup>, which is a typical method to get the eigen-functions of Sturm-Liouville problems for large  $n$ 's or large eigen-values. It is known,

however, that only the leading order of approximation is sufficiently accurate even for small  $n$ 's or small eigen-values. According to the WKB theory, its asymptotic behavior is assumed as

$$R_n(r) = \exp \left\{ S_0(r) \lambda_n + S_1(r) + \text{order of } \left( \frac{1}{\lambda_n} \right) \right\}, \quad (\text{B.3})$$

where  $S_0$  and  $S_1$  are the leading order of functions to find by comparing the powers of  $\lambda_n$  just like the perturbation methods. From the zeroth order, the derivative of  $S_0$  is obtained as

$$S_0'(r) = \pm i \sqrt{1-r^2}, \quad (\text{B.4})$$

which is sometimes called as a solution of eiconal equation. Similarly from the first order,

$$S_1(r) = -\ln \sqrt{r S_0'(r)}, \quad (\text{B.5})$$

which is sometimes called as a solution of transport equation. In Eqn. (B.5) a constant was not included. Substituting Eqns. (B.4) and (B.5) into Eqn. (B.3) and neglecting the higher order terms yield

$$R_n(r) \approx \frac{A \cos \left( \lambda_n \int_0^r \sqrt{1-\xi^2} d\xi \right) + B \sin \left( \lambda_n \int_0^r \sqrt{1-\xi^2} d\xi \right)}{\sqrt{r} (1-r^2)^{1/4}}, \quad (\text{B.6})$$

where A and B are the constants to be determined to match its behavior near  $r=0$ . It may be noticed that  $S_0$  is the leading order of oscillating behavior and  $S_1$

is that of decaying behavior. Since the asymptotic behavior of zeroth order Bessel function in Eqn. (B.2) is given by

$$J_0(\lambda_n r) \approx \sqrt{\frac{2}{\pi \lambda_n r}} \cos\left(\lambda_n r - \frac{\pi}{4}\right) \quad (\text{B.7})$$

for large  $\lambda_n r$  even if  $r$  is small, and the integration can be performed as

$$\int_0^r \sqrt{1 - \xi^2} d\xi = \frac{1}{2} \left( \sin^{-1} r + r \sqrt{1 - r^2} \right) \quad (\text{B.8})$$

the final expression of the  $n$ -th eigen-function for the medium range of  $r$  is obtained as

$$R_n(r) \approx \sqrt{\frac{2}{\pi \lambda_n r}} \frac{\cos\left\{\frac{\lambda_n}{2} r \sqrt{1 - r^2} + \frac{\lambda_n}{2} \sin^{-1} r - \frac{\pi}{4}\right\}}{(1 - r^2)^{1/4}} \quad (\text{B.9})$$

The asymptotic behavior for  $r \approx 1$  or near the wall of tube is the most useful, because the asymptotic eigen-values for large  $n$  can be found. The independent variable  $r$  is changed to  $z$  such that

$$z = 1 - r \quad (\text{B.10})$$

and the Graetz equation becomes

$$\frac{d^2 R_n}{dz^2} - \frac{1}{1-z} \frac{dR_n}{dz} + \lambda_n^2 z(2-z) R_n = 0 \quad (B.11)$$

For small  $z$  and large  $\lambda_n$ , the dominant balance of Eqn. (B.11) can be written as

$$\frac{d^2 R_n}{dz^2} - 2\lambda_n^2 z R_n = 0 \quad (B.12)$$

which has the solution

$$R_n(z) = C\sqrt{z} J_{1/3}\left(\frac{\sqrt{8}\lambda_n}{3} z^{3/2}\right) + D\sqrt{z} J_{-1/3}\left(\frac{\sqrt{8}\lambda_n}{3} z^{3/2}\right) \quad (B.13)$$

where  $C$  and  $D$  are the constants to be determined to match Eqn. (B.13) with Eqn. (B.9) for small  $z$  or  $r=1$ , again. Using variable  $z$ , Eqn (B.9) becomes

$$R_n(z) = \sqrt{\frac{2}{\pi\lambda_n}} \frac{\cos\left\{\sqrt{\frac{8}{3}}\lambda_n z^{3/2} - (\lambda_n - 1)\frac{\pi}{4}\right\}}{2^{1/4} z^{1/4}} \quad (B.14)$$

for small  $z$ , and the asymptotic behavior of Eqn. (B.13) becomes

$$R_n(z) = \sqrt{\frac{3}{\pi\lambda_n}} \frac{C \cos\left(\frac{\sqrt{8}}{3}\lambda_n z^{3/2} - \frac{5\pi}{12}\right) + D \cos\left(\frac{\sqrt{8}}{3}\lambda_n z^{3/2} - \frac{\pi}{12}\right)}{2^{1/4} z^{1/4}} \quad (B.15)$$

for large  $\lambda_n z$ , even if  $z$  is small. Comparing Eqns. (B.14) and (B.15), the constants  $C$  and  $D$  are determined and finally the asymptotic behavior of complete solution for the Graetz equation near the wall is found as

$$R_n(z) = \frac{\sqrt{8z}}{3} \left\{ \sin\left(\frac{\pi\lambda_n}{4} - \frac{\pi}{3}\right) J_{1/3}\left(\frac{\sqrt{8}\lambda_n z^{3/2}}{3}\right) - \sin\left(\frac{\pi\lambda_n}{4} - \frac{2\pi}{3}\right) J_{-1/3}\left(\frac{\sqrt{8}\lambda_n z^{3/2}}{3}\right) \right\} \quad (\text{B.16})$$

As  $z$  goes to zero, the first term having  $J_{1/3}$  go to zero but the second term having  $J_{-1/3}$  does not. Therefore, to satisfy the boundary condition,  $R_n(r=1) = 0$ , the coefficient of  $J_{-1/3}$  should be zero or

$$\sin\left(\frac{\pi\lambda_n}{4} - \frac{2\pi}{3}\right) = 0 \quad (\text{B.17})$$

which is the equation determining the eigen-values,  $\lambda_n$ .

$$\lambda_n = 4n + \frac{8}{3} \quad \text{for } n = 0, 1, 2, \dots \quad (\text{B.18})$$

And the asymptotic behavior of the eigen-functions near the wall becomes

$$R_n(z) = (-1)^n \sqrt{\frac{2z}{3}} J_{1/3}\left(\frac{\sqrt{8}}{3} \lambda_n z^{3/2}\right) \quad (\text{B.19})$$

Another important property of the Graetz function is its derivative at  $r=1$  or  $z=0$ , because it is used to calculate the mass flux at the wall. It can be found directly by taking derivative Eqn. (B.19) to give

$$\begin{aligned} R_n'(1) &= -\left(\frac{dR_n}{dz}\right)_{z=0} \\ &= \frac{(-1)^{n+1} 2^{2/3}}{\Gamma(4/3) 3^{5/6}} \lambda_n^{-1/3} = (-1)^{n+1} 0.715094 \lambda_n^{-1/3} \end{aligned} \quad (\text{B.20})$$



Finally, the coefficients of series expansion for the function,  $f(r) = 1$  for  $0 \leq r < 1$ , in terms of the eigen-functions are obtained. From the orthogonality of the eigen-functions, the n-th coefficient is given as

$$a_n = \frac{\int_0^1 r(1-r^2) R_n dr}{\int_0^1 r(1-r^2) R_n^2 dr} \quad (\text{B.21})$$

Integrating the Graetz equation, Eqn. (B.1), from 0 to 1, the numerator of Eqn. (B.21) is shortly evaluated to

$$\int_0^1 r(1-r^2) R_n dr = -\frac{R_n'(1)}{\lambda_n^2} \quad (\text{B.22})$$

The denominator of Eqn. (B.21) is, however, obtained by a few complicated steps, including the introduction of the partial derivative with respect to  $\lambda_n$ , being

denoted by  $\frac{\partial R_n(r)}{\partial \lambda_n}$ . The first step is to multiply Eqn. (B.1) by  $\frac{\partial R_n(r)}{\partial \lambda_n}$  and integrate over the interval (0,1). The second step is to multiply Eqn. (B.1) by  $R_n(r)$ , integrate over the same interval, and differentiate with respect to  $\lambda_n$ . These two separately obtained equations are combined to yield

$$\int_0^1 r(1-r^2) R_n^2 dr = \frac{R_n'(1)}{2\lambda_n} \left\{ \frac{\partial R_n(r)}{\partial \lambda_n} \right\}_{r=1} \quad (\text{B.23})$$

Substituting Eqns. (B.22) and (B.23) into Eqn. (B.21) results in

$$a_n = \frac{-2}{\lambda_n \left\{ \frac{\partial R_n(r)}{\partial \lambda_n} \right\}_{r=1}} \quad (\text{B.24})$$

The derivative in the denominator can be evaluated from Eqn. (B.19), so that the final expression is

$$a_n = (-1)^n \frac{2 \Gamma(2/3) 6^{2/3}}{\pi} \lambda_n^{-2/3} = (-1)^n 2.84606 \lambda_n^{-2/3} \quad (\text{B.25})$$

Every expression derived above is based on the asymptotic behavior of the eigen-functions, which is true only for large eigen-values or large n's. Some of the useful numbers obtained from the above equations are shown in Table B.1. They are extremely accurate for greater than n=3, and sufficiently accurate for the even smaller n's.

**Table B.1 First Ten Eigen-Values and Important Constants**

<b>n</b>	<b><math>\lambda_n</math></b>	<b><math>a_n</math></b>	<b><math>R'_n(1)</math></b>
0	2.666667	1.480010	-0.515672
1	6.666667	-0.803274	0.379950
2	10.666667	0.587343	-0.324853
3	14.666667	-0.474996	0.292137
4	18.666667	0.404451	-0.269572
5	22.666667	-0.355347	0.252678
6	26.666667	0.318859	-0.239354
7	30.666667	-0.290491	0.228459
8	34.666667	0.267692	-0.219310
9	38.666667	-0.248897	0.211471

## Appendix C

### Computation of Wall Accumulation and Sherwood Number without Snow Formation

This appendix illustrates how the wall accumulation rate and local Sherwood number, given by Eqns. (2.36) and (2.42) respectively, are computed on the assumption that there is no snow formation. The purpose of this illustration is to present the general computational method, available for any given conditions of flow rate or total pressure, any tube diameter, any contamination level of any species of contaminants. Again this computation is limited only to the laminar flow in a round tube.

The first information needed in this calculation is the sublimation pressure-temperature data in the form of either functional relation or numerical values. Presently, carbon dioxide is the test contaminant so the data in Appendix A is used for the illustration.

Secondly, the temperature and pressure dependence of mass diffusivity is required. There are many theoretical and/or empirical relations <sup>28</sup>, most of which show the dependence like

$$\frac{D(T, P)}{D(T_0, P_0)} = \left(\frac{T}{T_0}\right)^n \left(\frac{P_0}{P}\right), \quad (\text{C.1})$$

where  $P$  is the total pressure, and  $T_0$  and  $P_0$  are any reference temperature and pressure, respectively. The power  $n$  of the temperature ratio has typically the

value of 1.5 to 1.75 or sometimes even to 2.0. In this calculation,  $n$  was selected as 1.5 which was from the empirical Wilke-Lee relation and statistical mechanics, and was in a good agreement with the known values for carbon dioxide in helium.

At the end of this appendix, the computer program written in FORTRAN 77 is attached. In the program, the inner integrals in Eqns. (2.36) and (2.42) are analytically performed, because the velocity and the mass diffusivity are known for the given location whose temperature is known already. The outer integrals are performed numerically. The numerical technique is a five point Gaussian integration <sup>32</sup>, which is extremely accurate when the analytical expression to be integrated is available. Gaussian integral of a function,  $f(x)$ , from  $x_1$  to  $x_2$  is expressed as

$$\int_{x_1}^{x_2} f(x) dx = \sum_{i=1}^5 w(i) f(x_i) \frac{x_2 - x_1}{2}, \quad (B.2)$$

where  $w(i)$ 's are weight constants, given by

$$w(1) = w(5) = 0.2369268851$$

$$w(2) = w(4) = 0.4786286705$$

$$w(3) = 0.5688888889$$

and the  $x_i$ 's are selected as

$$x_1 = (x_1+x_2)/2 - 0.9061789459 (x_2-x_1) / 2$$

$$x_2 = (x_1+x_2)/2 - 0.5384693101 (x_2-x_1) / 2$$

$$x_3 = (x_1+x_2)/2$$

$$x_4 = (x_1+x_2)/2 + 0.5384693101 (x_2-x_1) /2$$

$$x_5 = (x_1+x_2)/2 + 0.9061789459 (x_2-x_1) /2$$

There is no summation accelerating technique involved, because the summations converges fast. The summation stops when the error is less than  $10^{-4}$ .

Input parameters in the program are the number of nodes (to discretize the interesting length of tube from the sublimation starting length), length for the Gaussian integration, the axial temperature gradient, the total inlet pressure, the contamination level, and the mean axial velocity. Output of calculation includes the wall accumulation rate of contaminant, zeroth-order accumulation rate, and the local Sherwood number.

The external function, XFCT, is the function to be integrated by the Gaussian method, and includes the variation of sublimation concentration and the temperature dependences of axial mean velocity and mass diffusivity. For the input temperature, the subroutine, SUBLIM, calculates the sublimation pressure and its derivative for carbon dioxide. And the subroutine, GAUSS, performs the gaussian integration for the given function, its integration limits, and the integration length.



```

C
C
C-----SOME CONSTANTS-----
C
C
C      PI=4.0*ATAN(1.0)
C
C      PRINT *, ' TYPE NUMBER OF NODES ( 250 TO 2500 ) '
      READ *,N
      N1=N+1
      PRINT *, ' TYPE DELTA X OF GAUSSIAN INTEGRATION IN M ( 0.001 TO
* 0.0001) '
      READ *,DELTA X
C
C      LENGTH AND DIAMETER IN METER
C
C      LENGTH=0.25
      DX=LENGTH/N
      DIAMETER=0.001
      RADIUS=DIAMETER/2.0
C
C      TEMPERATURE GRADIENT IN K/M
C
C      PRINT *, ' TYPE DTDX
* (TEMPERATURE GRADIENT IN K/M) (-80) '
      READ *, DTDX
C
C      GAS CONSTANT OF CARBON DIOXIDE IN BAR*(M**3)/(KG*K)
C
C      GASCONST=0.0018892
C
C
C      PRINT *, 'TYPE P IN PSIG ( 15 )
      READ *, P0
      P0=(P0+14.7)/14.7
      PPM=100
      PRINT *, 'TYPE FLUID VELOCITY AT 300 K AND P, IN M/SEC ( 0.5 ) '
      READ *,U
C
C-----FIND THE STARTING POINT OF SUBLIMATION-----
C
C      *0 DENOTES QUANTITY AT THE STARTING POINT
C
C      PCO2=(P0*1.01325)*PPM*1.0E-6
      TEMPO=140.0
      DO 10 I=1,N1
          TEMPO=TEMPO+DX*DTD X

```



```

        CALL SUBLIM(TEMPO,P,DPDT)
        IF(PCO2.GE.P) THEN
            ISTART=I
            GO TO 5
        END IF
10    CONTINUE
    PRINT *,SUBLIMATION STARTS AT BELOW 110 K '
    GO TO 25
5    CONTINUE
    IF(ISTARTEQ.1) THEN
        PRINT *, SUBLIMATION STARTS AT ABOVE 140 K '
        GO TO 25
    END IF

C
C
C
C
        VALUES OF X(I) AND TEMP(I)
        FROM SUBLIMATION STARTING POINT

    DO 20 I=1,N1
        X(I)=DX*(I-1)
        TEMP(I)=TEMPO+DTDIX*X(I)
20    CONTINUE
    DIFFUSE0=-6.12E-5*(TEMPO/298.0)**1.5*(1.0/P0)
    U0=U*(TEMPO/300.0)

C
C
C-----SUMMATION OF SERIES SOLUTION OF MACC(I) FOR X(I)-----
C
C
    DO 30 J=1,5000
        LAMBDA(J)=4.0*(J-1)+8.0/3.0
        TERM(J)= -(LAMBDA(J)**2*DIFFUSE0*TEMPO)
        * / (3.0*RADIUS**2*U0*DTDIX)
30    CONTINUE

C
C
C
    MACC(1)=0.0

C
C
    DO 40 I=2,N1
        DIFFUSIVITY
        DIFFUSE=DIFFUSE0 * (TEMP(I)/TEMPO)**1.5

C
C
        SUM=0.0
        SUMDEN=0.0
        X0=0.0

```



C  
C  
C  
C  
C  
C  
C  
C  
C  
C

FUNCTION XFCT(PSI)

FUNCTION OF PSI TO BE INTEGRATED FROM PSI=0 TO X

COMMON XI,TERMJ,TEMPO,DTDX,GASCONST

TEMP=TEMPO+PSI\*DTDX

CALL SUBLIM(TEMP,P,DPDT)

DCDPSI= (DPDT-P/TEMP) / (GASCONST\*TEMP) \*DTDX

XFCT= (1.0+PSI\*DTDX/TEMPO)/(1.0+XI\*DTDX/TEMPO)

\* \* EXP(TERMJ\* ( (1.0+XI \*DTDX/TEMPO)\*\*1.5

\* \* (1.0+PSI\*DTDX/TEMPO)\*\*1.5 ) ) \* (-DCDPSI)

END

SUBROUTINE SUBLIM(T,P,DPDT)

C  
C  
C  
C  
C  
C  
C  
C  
C

SUBLIMATION PRESSURE OF CARBON DIOXIDE  
AS A FUNCTION OF TEMPERATURE  
AND ITS DERIVATIVE

A=14.57893  
B=14.48067  
C=65.35685  
D=47.14593  
E=14.53922

C  
C  
C  
C  
C

TRIPLE POINT TEMP( K ) AND PRESS( BAR = 1.0E5 PA )

TT= 216.58  
PT= 5.180

C  
C  
C

T0=T/TT  
P1=A\*(1.0-1.0/T0)  
P2=B\*ALOG(T0)  
P3=C\*(T0-1.0)  
P4=D\*(T0\*\*2-1.0)  
P5=E\*(T0\*\*3-1.0)

C  
C

P= PT \* EXP( P1-P2+P3-P4+P5 )  
DPDT=P/TT\*(A/T0\*\*2-B/T0+C-2.0\*D\*T0+3.0\*E\*T0\*\*2)

C  
C

RETURN  
END

SUBROUTINE GAUSS(G,A,B,DX,GINTEG)

INTEGRAL OF G(X) FROM A TO B

WITH INTERVAL DX

BY 5 POINT GAUSSIAN INTEGRATION

REAL POINT(5),WEIGHT(5)

N=(B-A)/DX

WEIGHTS

WEIGHT(1)=0.2369268851

WEIGHT(2)=0.4786286705

WEIGHT(3)=0.5688888889

WEIGHT(4)=WEIGHT(2)

WEIGHT(5)=WEIGHT(1)

GINTEG=0.0

DO 20 I=1,N+1

X1=A+(I-1)\*DX

IF(LLT.N+1) THEN

X2=X1+DX

ELSE

X2=B

END IF

ALPHA=(X1+X2)/2.0

BETA=(X2-X1)/2.0

POINTS

POINT(1)=ALPHA - 0.9061789459\*BETA

POINT(2)=ALPHA - 0.5384693101\*BETA

POINT(3)=ALPHA + 0.0 \*BETA

POINT(4)=ALPHA + 0.5384693101\*BETA

POINT(5)=ALPHA + 0.9061789459\*BETA

SUM

DO 10 J=1,5

P=POINT(J)

10  
20

~~GINTEG~~-GINTEG+WEIGHT(J)\*G(P)\*BETA  
CONTINUE

CONTINUE  
RETURN  
END

# Appendix D

## Convection Augmented Diffusion

### D.1 Introduction

This appendix presents the convection augmented diffusion of a concentration wave in fully developed laminar flow through a round tube, which is mostly contributed by G. I. Taylor<sup>33</sup>. This analytical work intends to reduce 2-D convection-diffusion equation

$$\frac{\partial c}{\partial t} + 2u_m \left\{ 1 - \left( \frac{r}{r_0} \right)^2 \right\} \frac{\partial c}{\partial x} = D \left\{ \frac{1}{r} \frac{\partial}{\partial r} \left( r \frac{\partial c}{\partial r} \right) + \frac{\partial^2 c}{\partial x^2} \right\} \quad (D.1)$$

to a 1-D equation

$$\frac{\partial c}{\partial t} + u_m \frac{\partial c}{\partial x} = D_{\text{eff}} \frac{\partial^2 c}{\partial x^2}, \quad (D.2)$$

where  $c$  is the mean concentration over the cross-section of the tube, and  $D_{\text{eff}}$  is the effective mass diffusivity to be found. Therefore, it specifically aims at a simple relation of  $D_{\text{eff}}$  and other coefficient in Eqn. (B.1) such as  $D$ ,  $u_m$ , and  $r_0$ , or

$$D_{\text{eff}} = D + \text{fct of } ( D, u_m, r_0 ) \quad (D.3)$$

where the second term is the diffusion effect augmented by the convection of the mass.

This simplification is possible in the limiting case of "fast radial diffusion" compared with the convective transport. Figure D.1 shows schematically two limiting cases, slow and fast radial diffusion. If the initial concentration (at  $t_0$ ) is uniform in radial direction and has a step change in axial direction, a "tongue" is formed as time goes in the case of dominant convection or slow radial diffusion. But in the case of fast radial diffusion, an axial dispersion of concentration occurs by the amount of the length of the tongue, even if no axial diffusion is assumed. Taylor describes this limiting case of slow diffusion as

*" The time necessary for appreciable effects to appear, owing to convective transport, is long compared with the 'time of decay' during which radial variations of concentration are reduced to a fraction of their initial value through the action of molecular diffusion."*

Quantitatively, the radial diffusion time can be characterized by

$$t_{\text{diff}} = \frac{r_0^2}{(3.83)^2 D} \quad (\text{D.4})$$

because the solution of the radial diffusion equation,

$$\frac{\partial c}{\partial t} = \frac{D}{r} \frac{\partial}{\partial r} \left( r \frac{\partial c}{\partial r} \right) \quad (\text{D.5})$$

is

$$c = \sum_{n=0}^{\infty} a_n \exp(-\lambda_n^2 t) J_0 \left( \frac{\lambda_n r}{\sqrt{D}} \right) \quad (\text{D.6})$$

and the leading behavior of the Bessel function is determined by



$$\frac{\lambda_n r_0}{\sqrt{D}} = 3.83 \quad (D.7)$$

and the characteristic time for the diffusion is  $(1/\lambda_n^2)$ .

Convection characteristic time is simply taken as

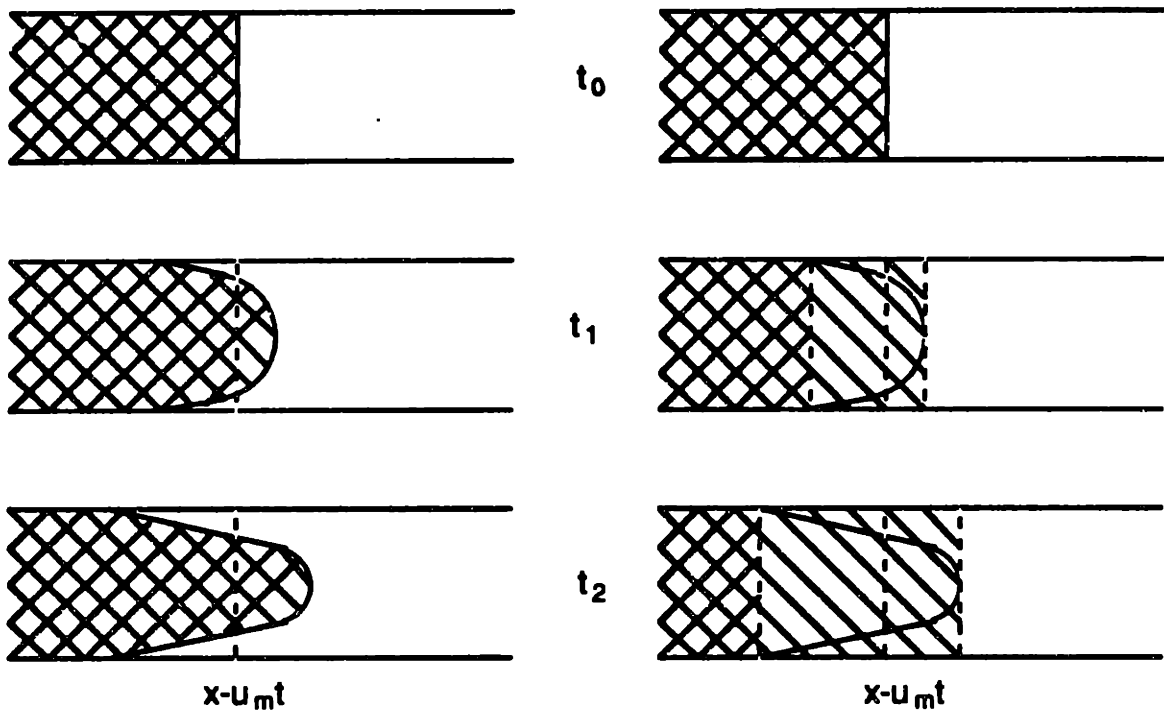
$$t_{\text{conv}} = \frac{L}{u_m}, \quad (D.8)$$

where L is the length of tube that the concentration wave travels.

The fast radial diffusion case is true if  $t_{\text{conv}} \gg t_{\text{diff}}$ , or from Eqns. (D.3) and (D.8)

$$\text{Re Sc} \ll 59 \left( \frac{L}{d} \right), \quad (D.9)$$

where Re and Sc are the Reynolds and Schmidt numbers, respectively. Eqn. (D.9) is the condition for which the following analysis is valid.



(a) Slow Radial Diffusion

(b) Fast Radial Diffusion

Figure D.1 Dispersion of a Step Concentration

## D.2 Effective Mass Diffusivity

To consider only the radial diffusion effect to the axial dispersion, the axial diffusion term in Eqn. (D.1) is neglected for the time being.

$$\frac{\partial c}{\partial t} + 2u_m \left\{ 1 - \left(\frac{r}{r_0}\right)^2 \right\} \frac{\partial c}{\partial x} = \frac{D}{r} \frac{\partial}{\partial r} \left( r \frac{\partial c}{\partial r} \right) \quad (\text{D.10})$$

Taking a new axial coordinate,  $\xi$ , moving with the mean velocity,

$$\xi = x - u_m t, \quad (\text{D.11})$$

the coordinate transform is made for  $x, r$ , and  $t$  to  $\xi, r$ , and  $t$  such that

$$\begin{aligned} \left(\frac{\partial c}{\partial t}\right)_x &= \left(\frac{\partial c}{\partial \xi}\right)_t \left(\frac{\partial \xi}{\partial t}\right)_x + \left(\frac{\partial c}{\partial t}\right)_\xi \\ &= -u_m \frac{\partial c}{\partial \xi} + \frac{\partial c}{\partial t} \end{aligned} \quad (\text{D.12})$$

and

$$\begin{aligned} \left(\frac{\partial c}{\partial x}\right)_t &= \left(\frac{\partial c}{\partial \xi}\right)_t \left(\frac{\partial \xi}{\partial x}\right)_t \\ &= \frac{\partial c}{\partial \xi} \end{aligned} \quad (\text{D.13})$$

Eqn. (D.10) becomes

$$\frac{\partial c}{\partial t} + 2u_m \left\{ \frac{1}{2} - \left(\frac{r}{r_0}\right)^2 \right\} \frac{\partial c}{\partial \xi} = \frac{D}{r} \frac{\partial}{\partial r} \left( r \frac{\partial c}{\partial r} \right) \quad (\text{D.14})$$

Then, the mean velocity (not  $u_m$ ) in the  $\xi$ -coordinate is zero everywhere and any transfer of mass is due to radial diffusion, which is very fast from the above discussion. Therefore, any radial variation of  $c$  disappears rapidly. In other

words,  $c$  is near steady and axial variation of  $c$  is not a strong function of  $r$ . In Eqn. (D.14),

$$\frac{\partial c}{\partial t} \approx 0 \quad (D.15)$$

and

$$\frac{\partial c}{\partial \xi} \approx \frac{\partial c_m}{\partial \xi} = \text{independent of } r \quad (D.16)$$

where  $c_m$  is the mean concentration.

With Eqns. (D.15) and (D.16), Eqn. (D.14) is simplified to

$$2u_m \left\{ \frac{1}{2} - \left(\frac{r}{r_0}\right)^2 \right\} \frac{\partial c_m}{\partial \xi} = \frac{D}{r} \frac{\partial}{\partial r} \left( r \frac{\partial c}{\partial r} \right) \quad (D.17)$$

which is immediately solved by integrating twice with respect to  $r$ , to yield

$$c = c_{r=0} + \frac{u_m r_0}{4D} \frac{\partial c_m}{\partial \xi} \left\{ \left(\frac{r}{r_0}\right)^2 - \frac{1}{2} \left(\frac{r}{r_0}\right)^4 \right\} \quad (D.18)$$

The mass transfer rate across the cross-section at a given  $\xi$  is

$$\dot{m} = \int_0^{r_0} c u (2\pi r) dr \quad (D.19)$$

or

$$\dot{m} = -\frac{u_m^2 r_0^2}{48D} (\pi r_0^2) \frac{\partial c_m}{\partial \xi} \quad (D.20)$$

Therefore, the augmented diffusivity can be expressed as

$$D_{\text{aug}} = \frac{u_m^2 r_0^2}{48 D} = \frac{u_m^2 d^2}{192 D}, \quad (\text{D.21})$$

which is the desired second term of Eqn. (D.3). The final expression for the effective mass diffusivity including molecular axial diffusion and convection augmented diffusion is given by

$$D_{\text{eff}} = D + \frac{u_m^2 d^2}{192 D}. \quad (\text{D.22})$$

### D.3 Optimum Velocity for Minimum Dispersion

Inspecting Eqn. (D.22), it is noticed that there is an optimum flow velocity to cause the minimum dispersion of concentration wave. The amount of dispersion is typically mentioned in terms of the penetration length of a square wave, which is defined as

$$L_{\text{pene}} = \sqrt{12 D_{\text{eff}} t_d}, \quad (\text{D.23})$$

where  $t_d$  is the diffusion time for the concentration wave to disperse. Since the diffusion time is simply  $(L/u_m)$ , there is a minimum penetration length. The optimum velocity to give this minimum is found by differentiating Eqn. (D.23) with respect to the velocity.

$$(u_m)_{\text{opt}} = \sqrt{192} \frac{D}{d}. \quad (\text{D.24})$$

At a larger velocity than the optimum, the convection augmented diffusion is bigger and results in more dispersion than its minimum. At a smaller velocity, the concentration wave migrates so slow that the wave has more diffusion time to disperse for the given tube length. Finally, it should be mentioned again that the above description is true only when the condition, Eqn. (D.9), is satisfied.

## Appendix E

### Green's Function for Convection-Diffusion Equation

In this appendix, Green's function for one-dimensional convection-diffusion equation

$$\left( \frac{\partial}{\partial t} + u \frac{\partial}{\partial x} - D \frac{\partial^2}{\partial x^2} \right) f(x,t) = 0 \quad (\text{E.1})$$

is derived<sup>35, 36</sup>. From its definition, Green's function is the solution for a unit delta function heterogeneity,  $\delta(x-x') \delta(t-t')$ , where  $x'$  and  $t'$  are the source coordinates corresponding  $x$  and  $t$ , respectively. Now the problem is to solve the equation

$$\left( \frac{\partial}{\partial t} + u \frac{\partial}{\partial x} - D \frac{\partial^2}{\partial x^2} \right) G(x,t;x',t') = \delta(x-x') \delta(t-t') \quad (\text{E.2})$$

with homogeneous boundary conditions at  $x=\pm\infty$  and  $t=\pm\infty$ . First of all, it is clear that  $G(x,t;x',t')=0$  for  $t<t'$  from the causality. Physically, the delta function in equation (E.2) is an unit impulse input at the location of  $x=x'$  and at the time  $t=t'$ , and nothing happens before the input is applied. So the seeking solution is the case of  $t>t'$ .

To obtain a Fourier transform of the Green's function, Equation (E.2) is multiplied with  $\exp(ikx+i\omega t)$  and integrated for both of  $x$  and  $t$  from  $-\infty$  to  $+\infty$ . Then the left hand side of the equation can be integrated by part using homogeneous

boundary conditions to yield the Fourier transform of the Green's function, and the right hand side can be simply calculated. Transformed equation is,

$$(-i\omega - iku + k^2 D) \tilde{G}(k, \omega; x', t') = e^{ikx' + i\omega t'} \quad (E.3)$$

where

$$\tilde{G}(k, \omega; x', t') = \int_{-\infty}^{\infty} dx \int_{-\infty}^{\infty} dt G(x, t; x', t') e^{ikx + i\omega t} \quad (E.4)$$

Therefore, Fourier transform of Green's function is expressed as

$$\tilde{G}(k, \omega; x', t') = \frac{i e^{ikx' + i\omega t'}}{\omega + ku + ik^2 D} \quad (E.5)$$

In order to get the Green's function, equation (E.5) should be inversely transformed. According to equation (E.4), the inverse transform is given as

$$G(x, t; x', t') = \frac{1}{(2\pi)^2} \int_{-\infty}^{\infty} dk \int_{-\infty}^{\infty} d\omega \tilde{G}(k, \omega; x', t') e^{-ikx - i\omega t} \quad (E.6)$$

or

$$G(x, t; x', t') = \frac{1}{(2\pi)^2} \int_{-\infty}^{\infty} dk \int_{-\infty}^{\infty} d\omega \frac{i e^{-i\omega(t-t') - ik(x-x')}}{\omega + ku + ik^2 D} \quad (E.7)$$

In equation (E.7), there are two integrals to be performed. Out of them, integration along the  $\omega$  axis can be done through a contour integral in complex  $\omega$ -plane. (Fig. E.1) shows the selected contour. There is only one pole ( $\omega = -ku - ik^2 D$ ), which has a negative imaginary part, and so it is located in lower half



plane. Infinite radius half circle is in lower half plane because the coefficient of  $\omega$  at the exponent is  $-i(t-t')$ , whose imaginary part is always negative (from the causality discussion, above), and final real part of  $-i\omega(t-t')$  becomes negative through the lower half circle, so that its integral vanishes as radius of the circle goes to infinity.

From the Cauchy's residue theorem,

$$G(x,t;x',t') = \frac{1}{(2\pi)^2} \int_{-\infty}^{\infty} dk (-2\pi i) \text{Res}_{\omega = -ku - ik^2 D} \left( \frac{i e^{-i\omega(t-t') - ik(x-x')}}{\omega + ku + ik^2 D} \right), \quad (\text{E.8})$$

where  $(-2\pi i)$  is due to its clockwise contour direction. Calculation of the residue and simplification yields

$$G(x,t;x',t') = \frac{1}{2\pi} \int_{-\infty}^{\infty} dk e^{-D(t-t')k^2 - i[(x-x') - (t-t')u]k} \quad (\text{E.9})$$

This integration along  $k$  is a Gaussian integral. It can be easily shown that

$$\int_{-\infty}^{\infty} dk e^{-a^2 k^2 \pm bk} = \frac{\sqrt{\pi}}{a} e^{\frac{b^2}{4a^2}} \quad (\text{E.10})$$

Using equation (E.10), equation (E.9) is integrated and finally Green's function for  $t > t'$  is given by

$$G(x,t;x',t') = \frac{1}{\sqrt{4\pi D(t-t')}} \exp \left\{ -\frac{[(x-x') - (t-t')u]^2}{4D(t-t')} \right\} \quad (\text{E.11})$$

Again, for  $t < t'$ ,

$$G(x, t; x', t') = 0 \quad (E.12)$$

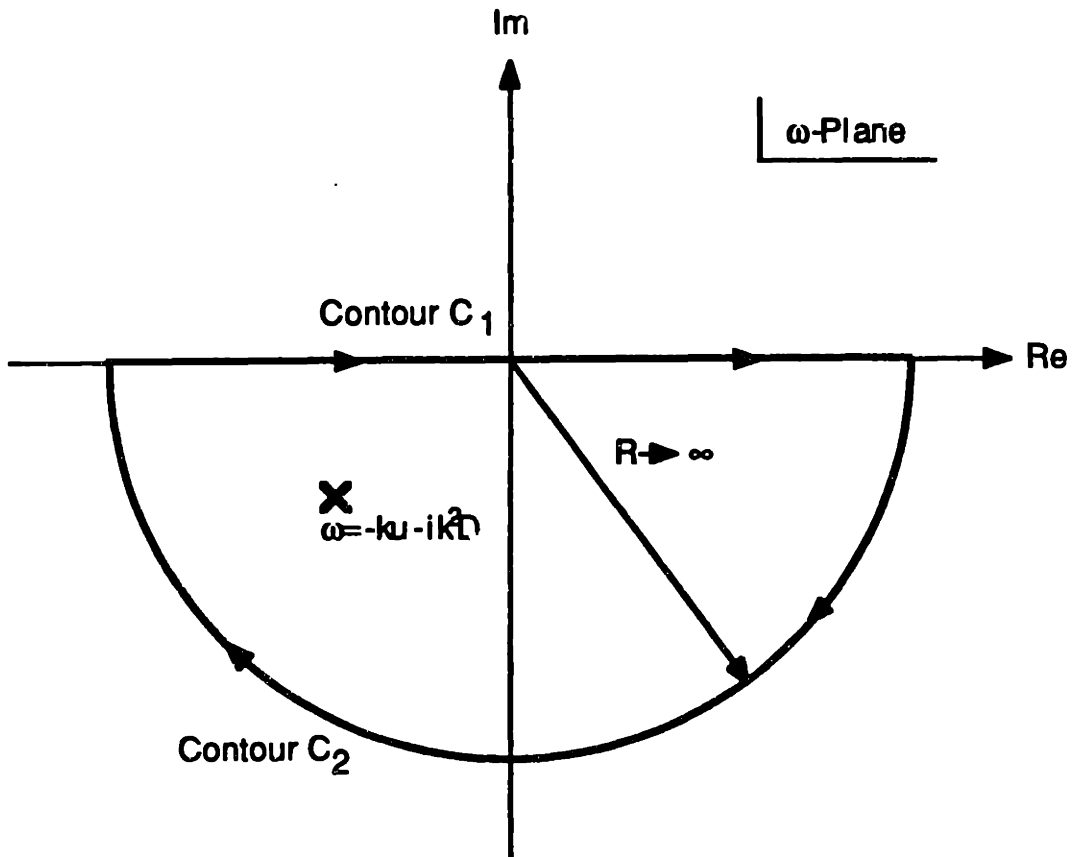


Figure E.1 Contour of Integration in Complex Plane

# Appendix F

## Details of Experimental Results

The experimental results, not shown in Chapter 4, are presented in this appendix. The TCD outputs of RUNs 1 and 2, and 7 through 11 are shown in Figures F.1 through F.7, respectively.

The runs at higher pressure (RUNs 10 and 11) yielded more dispersion than those at lower pressure (RUNs 1 and 2). An obvious snow formation was observed for the RUNs 2, 9, and 11, and seemingly no snow formation was observed for the other runs.

The accumulation shapes for the snow-formed runs are different each other: a concentrated accumulation for the RUN 9, a much dispersed accumulation for the RUN 11, and a medium accumulation for the RUN 2. About 14 %, 19 %, and 12 % of total contaminant formed and migrated downstream by 90 times, 80 times, and 130 times of diameter for the RUN 2, the RUN 9, and the RUN 11, respectively.

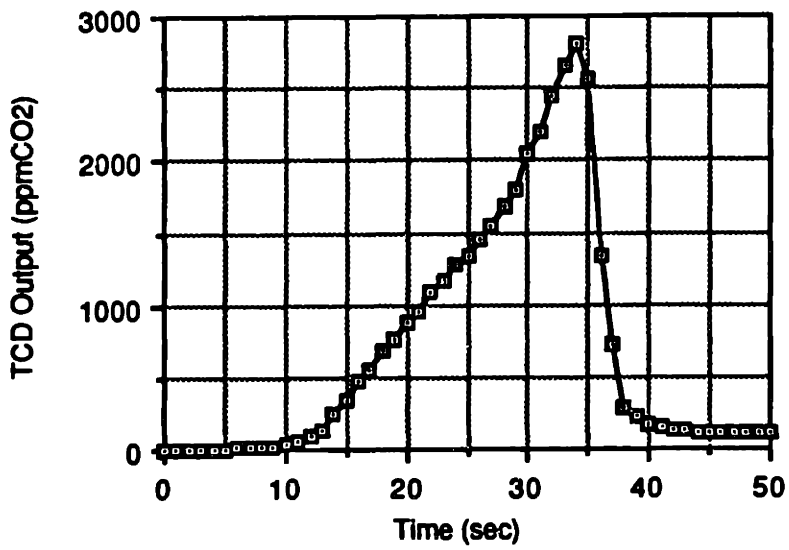


Figure F.1 TCD Output of RUN 1

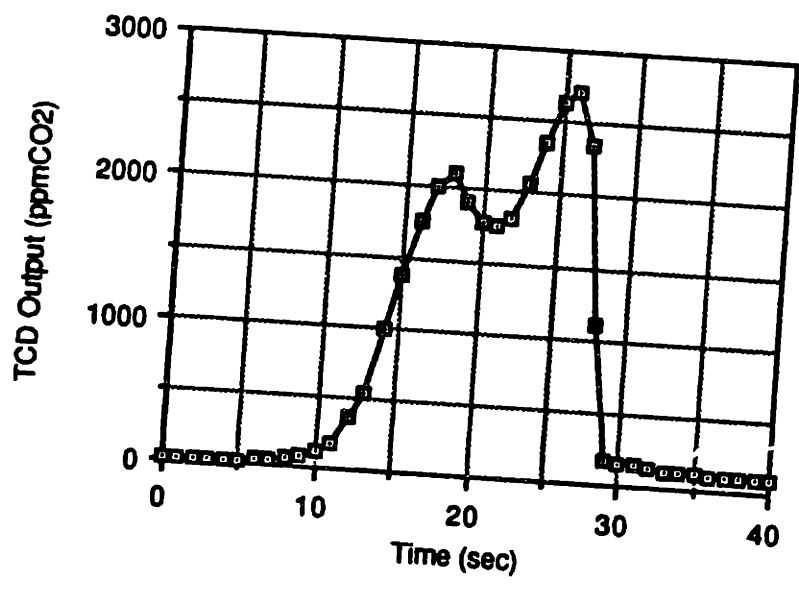


Figure F.2 TCD Output of RUN 2

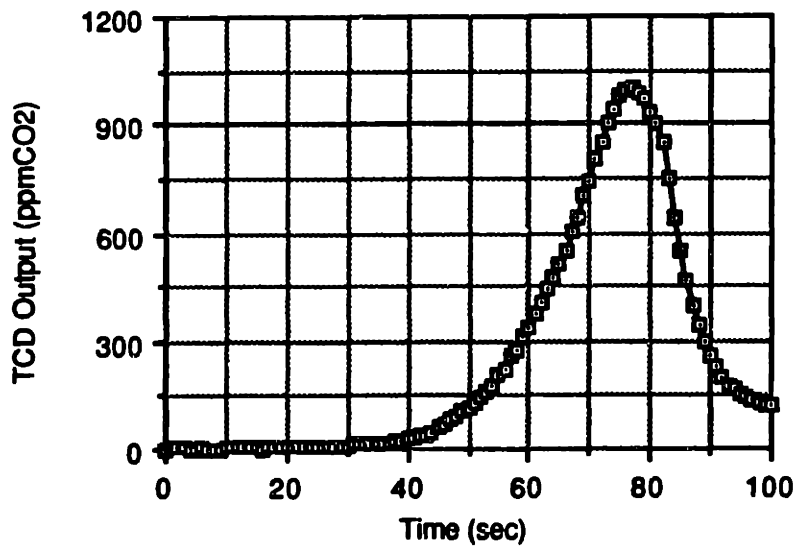


Figure F.3 TCD Output of RUN 7

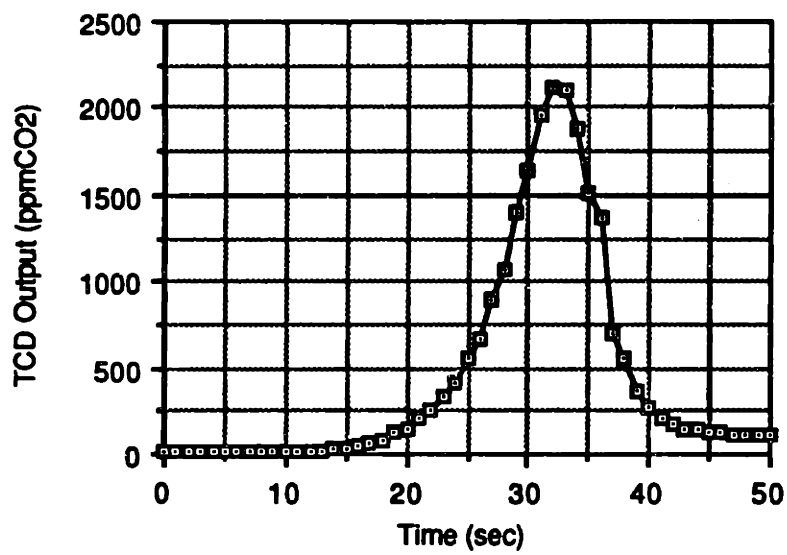


Figure F.4 TCD Output of RUN 8



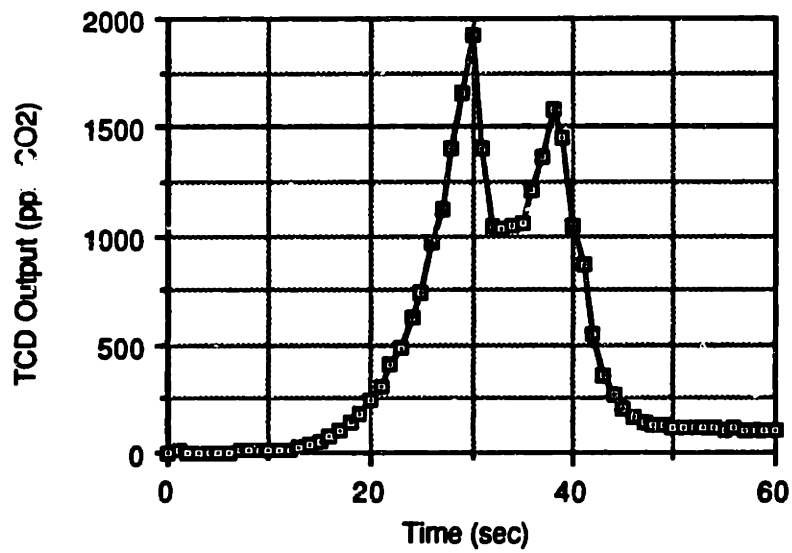


Figure F.5 TCD Output of RUN 9

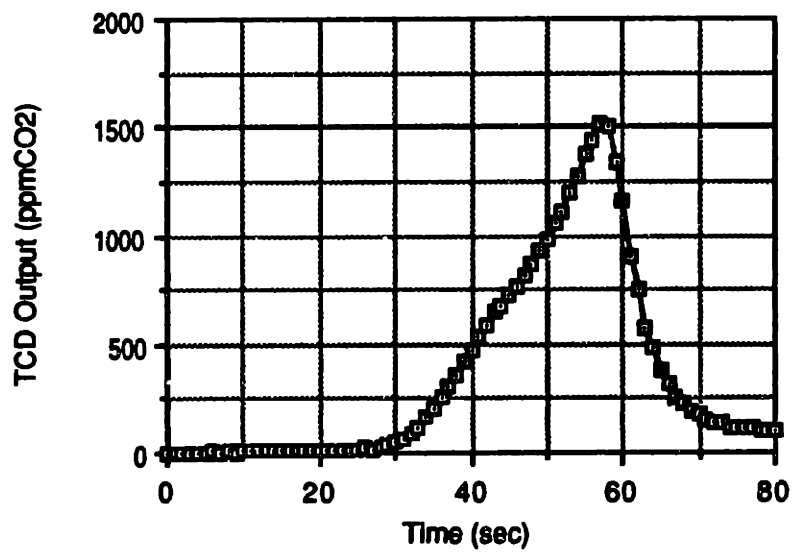


Figure F.6 TCD Output of RUN 10

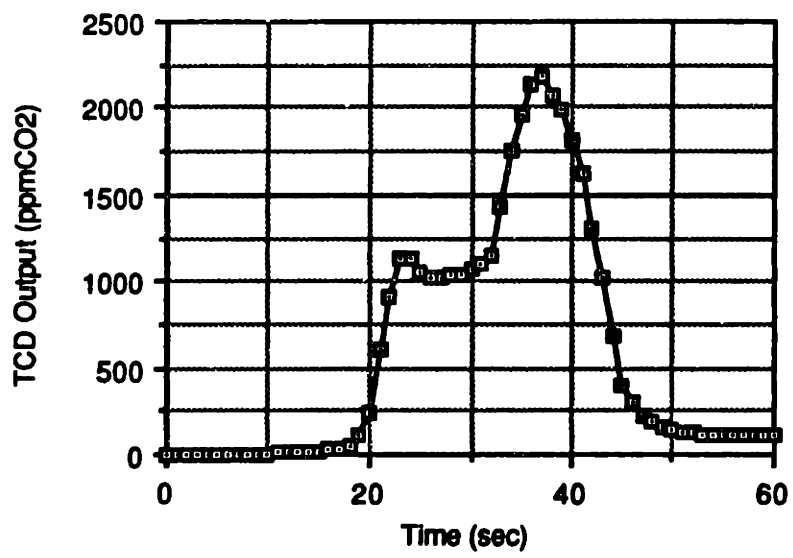


Figure F.7 TCD Output of RUN 11

## References

1. Barron, R., *Cryogenic Systems*, McGraw-Hill Book Co., New York, 1966
2. Scott, R., *Cryogenic Engineering*, D. Van Nostrand Co. Inc., Princeton, New Jersey, 1959
3. Bailey, B., "Freeze Out Purification of Gases in Heat Exchangers ", *Adv. in Cryogenic Eng.*, Vol. 2, pp 45-49, 1956
4. Kratz, W., "The Effect of Temperature of Impurity Adsorption from Hydrogen on Activated Carbon and Silica Gel ", *Adv. in Cryogenic Eng.*, Vol. 25, pp 597-608, 1980
5. Leyarovski, E., Georgiev, J. and Zahariev, A., "Application of Low Temperature Desorption in Systems for Adsorptive Purification of Cryogenic Gases ", *Cryogenics*, Vol. 26, pp 29-32, 1986
6. Koenig, K., *Performance of Thermal Regenerators on the Removal of Contaminants*, Sc.D. Thesis, MIT, 1970
7. Ashley, J., *Refrigeration Contaminants : The Feasibility of Using Light Scattering to Detect the Sublimation Point of a Carbon Dioxide Contaminant in Nitrogen*, B.S. Thesis, MIT, 1985
8. Sellars, J., Tribus, M. and Klein, J., "Heat Transfer to Laminar Flow in a Round Tube or Flat Conduit - The Graetz Extended ", *Trans. ASME*, Vol. 78, pp 441-448, 1956
9. Tribus, M. and Klein, J., "Forced Convection from Nonisothermal Surface ", *U. of Mich., Syup.* 1952, No. 8, pp 211-235, 1953
10. Singh, S., "Heat Transfer by Laminar Flow in a Cylindrical Tube ", *Appl. Sci. Res., Sec. A*, Vol. 7, pp 325-340, 1957

11. Singh, S., " The Determination of Eigen-Functions of a Certain Sturm-Liouville Equation and Its Application to Problems of Heat Transfer ", *Appl. Sci. Res., Sec. A.*, Vol. 7, pp 237-250, 1957
12. Rohsenow, W., Class Note on " Advanced Heat Transfer ", MIT, 1956
13. Siegal, R., Sparrow, E. and Hallman, T., " Steady Laminar Heat Transfer in a Circular Tube with Prescribed Wall Heat Flux ", *Appl. Sci. Res., Sec. A.*, Vol. 7, pp 386-392, 1957
14. Gray, D. and Male, D., *Handbook of Snow*, Pergamon Press, Inc., New York, 1981
15. Colbeck, S., *Dynamics of Snow and Ice Masses*, Academic Press, Inc., New York, 1980
16. Giddings, J., *Dynamics of Chromatography*, Marcel Decker, Inc., New York, 1965
17. Message, G., *Practical Aspects of Gas Chromatography/Mass Spectrometry*, John Wiley & Sons, Inc., New York, 1984
18. Lee, M., Yang, F. and Bartle, K., *Open Tubular Column Gas Chromatography*, John Wiley & Sons, Inc., New York, 1984
19. Schupp III, O., *Gas Chromatography*, John Wiley & Sons, Inc., New York, 1968
20. Grob, R., *Modern Practice of Gas Chromatography*, 2nd Ed., John Wiley & Sons, Inc., New York, 1985
21. Flood, E., *The Solid-Gas Interface*, Marcel Decker, Inc., New York, 1967
22. Bergles, A. and Rohsenow, W., " The Determination of Forced-Convection Surface-Boiling Heat Transfer ", *J. Heat Transfer, Trans. ASME, Series C.*, Vol. 85, pp 365-372, 1964
23. Frost, W., *Heat Transfer at Low Temperatures*, Plenum Press, New York, 1975

24. Hsu, Y. and Graham, R., *Transport Processes in Boiling and Two-Phase Systems*, McGraw-Hill Book Co., New York, 1976
25. McCarty, S., *Thermodynamic Properties of Helium 4 from 2K to 1500K with Pressures to 1000 Atmospheres*, National Bureau of Standards, Boulder, Colorado, 1972
26. ASHRAE *Thermodynamic Properties of Refrigerants*, ASHRAE, New York, 1974
27. Angus, S. et. al., *International Thermodynamic Tables of the Fluid State Carbon Dioxide*, Pergamon Press, Inc., New York, 1970
28. Reid, R., Prausnitz, J. and Sherwood, T., *The Properties of Gases and Liquids*, 3rd Ed., McGraw-Hill Book Co., New York, 1977
29. Maynard, v. and Grushka, E., " Measurement of Diffusion Coefficients by Gas Chromatography Broadening Techniques, A Review ", *Adv. Chromat.*, Vol. 12, pp 99-140, 1975
30. Bender, C. and Orszag, S., *Advanced Mathematical Methods for Scientists and Engineers*, McGraw-Hill Book Co., New York, 1978
31. Roache, P., *Computational Fluid Dynamics*, Hermosa Publishers, Albuquerque, New Mexico, 1972
32. Conte, S. and Boor, C., *Elementary Numerical Analysis*, 3rd Ed., McGraw-Hill Book Co., New York, 1980
33. Taylor, G., " Dispersion of Soluble Matter in Solvent Flowing Slowly through a Tube ", *Proc. Roy. Soc. London*, Vol. 219, pp 186-203, 1953
34. Turner, G., *Heat and Concentration Waves*, Academic Press, Inc., New York, 1972
35. Carrier, G. and Pearson, C., *Partial Differential Equations-Theory and Technique*, Academic Press, Inc., Orlando, Florida, 1976

36. Morse, P. and Feshbach, H., *Methods of Theoretical Physics*, Part I and II, McGraw-Hill Book Co., New York, 1953
37. Hatsopoulos, G. and Keenan, J., *Principles of General Thermodynamics*, John Wiley & Sons, Inc., New York, 1965
38. Van Wylen, G. and Sonntag, R., *Fundamentals of Classical Thermodynamics*, 2nd Ed., John Wiley & Sons, Inc., New York, 1976
39. Rohsenow, W. and Choi, H., *Heat, Mass, and Momentum Transfer*, Prentice-Hall, Inc., Eaglewood Cliffs, New Jersey, 1961
40. Eckert, E. and Drake, R., *Heat and Mass Transfer*, McGraw-Hill Book Co., New York, 1959
41. Carslaw, H. and Jaeger, J., *Conduction of Heat in Solids*, 2nd Ed., Oxford University Press, Oxford, 1959
42. Arpaci, V., *Conduction Heat Transfer*, Addison-Wesley Publishing Co., Palo Alto, California, 1966
43. Kays, W. and Crawford, M., *Convective Heat and Mass Transfer*, 2nd Ed., McGraw-Hill Book Co., New York, 1980

## Biographical Note

The author was born in Seoul, Korea on September 21, 1960. He was grown and educated in this big city until he graduated from Seoul National University with the degree of B.S.E. in February, 1983. It was in his sophomore year that he planned to continue his study to the Ph.D. degree in the area of mechanical engineering. At the same time of the graduation, he was selected as a Korean Government Scholarship student. The scholarship sponsors the selected students for the graduate studies in a foreign country.

He came to the U.S in June, 1983 to attend the University of Michigan in Ann Arbor, Michigan for the degree of M.S.E.. He completed the degree and was accepted to MIT for Ph.D. in September, 1984. After passing the doctoral qualifying examination, he joined the Cryogenic Engineering Laboratory in June, 1985. Since the fall term of the same year, he has worked on the problem of cryogenic contamination as a research assistant.

The author has been only in school, except a short term training at a small electrical machinery company in the summer of his senior year. One of the goals of his education in this foreign country was to contribute the economic development of his home country, Korea.